CHARGED JET PROPERTIES MEASURED WITH THE ALICE EXPERIMENT

MASTER THESIS

HENDRIK POPPENBORG

INSTITUT FÜR KERNPHYSIK
WESTFÄLISCHE WILHELMS-UNIVERSITÄT MÜNSTER

– April 2015 –

ERSTER GUTACHTER: PD Dr. Christian Klein-Bösing
ZWEITER GUTACHTER: Prof. Dr. Johannes P. Wessels

CONTENTS

INTRODUCTION

The collisions of highly accelerated lead ions can lead to the formation of a temporary state of matter that features an extreme density and temperature. Analogous to a classical plasma, where electrons and ions are no longer subject to the atomic bonding, this exotic type of strongly interacting matter is refered to as a *Quark-Gluon Plasma* (QGP). Here, the constituting quarks and gluons are no longer confined to the extent of a hadron.
The QGP in the experiment vanishes as violently as it has been created. After a short time the medium expands and cools down leading to the hadronization of thousands of particles. Observed by a suitable detector system, the properties of these remnants can then be linked to the properties of the QGP (fig. 1).
The research of the QGP has become famous for evoking the thunderous conditions that prevailed right after the big bang, but above all it provides a unique scenario to study the dynamics of the strong interaction and its challenging nature.

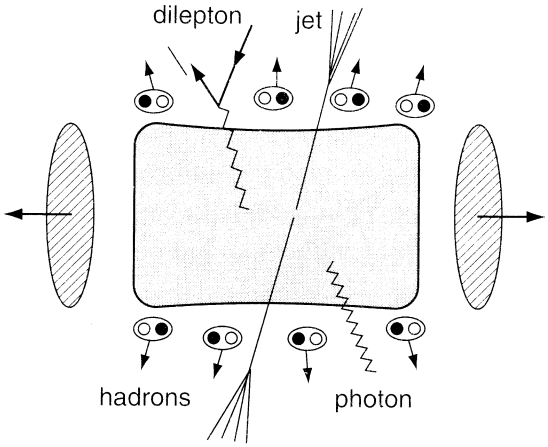

Figure 1: The collision of heavy ions leaves a hot and dense environment of deconfined quarks and gluons behind. Various probes allow insights into the involved processes. [1]

One specific issue is the medium-enhanced energy loss of partons (i.e. quarks and gluons) that originate from hard scatterings in the environment of the presumed QGP. Since an energetic parton fragments into a spray of hadrons – a *jet* of particles – the associated phenomenon is called *jet quenching*.
The work presented here consists of two separate studies. First, a correction of charged jet spectra for background fluctuations and detector effects has been performed (Chapter 4). In a second project (Chapter 5), elementary properties of *subjets* have been studied – a novel observable that is sensitive to the fragmentation pattern of the jet.
Introductory chapters provide an overview over the Strong Interaction and the quark-gluon plasma (Chapter 1), heavy-ion collisions and jets (Chapter 2), and the underlying experiment – the ALICE project at the Large Hadron Collider (LHC) at CERN (Chapter 3).

1

THE STRONG INTERACTION AND THE QUARK-GLUON PLASMA

The investigation of the quark-gluon plasma constitutes the current frontier in the research history of nuclear matter and the strong interaction. In that sense, the following sections shall provide an impression of the overall picture: episodes of history that led to our today's view of nuclear matter, the theory of quantum chromodynamics and finally the properties of the quark-gluon plasma.

1.1 RESEARCH OF THE STRONG INTERACTION

At the beginning of the 20th century, the attempt was to explain the structure of matter on the smallest scales in terms of electromagnetic interaction. With the evidence of the negatively charged electron being a constituting particle, its discoverer J.J. Thomson proposed the atom to be a *sphere of uniform positive electrification* in which the electrons are bound and their charges are balanced [2]. The image of a positive charge that is stretched over the extent of an atom was then to be revised by E. Rutherford. Scattering alpha particles against gold nuclei, he concluded that the space in an atom is devoid of any positive charges except a heavily charged center with a radius smaller than 10^{-14} m [3]. With the positive charges connected to the atomic numbers of the periodic table and the discovery of the neutron the picture of protons and neutrons constituting a nucleus became plausible.

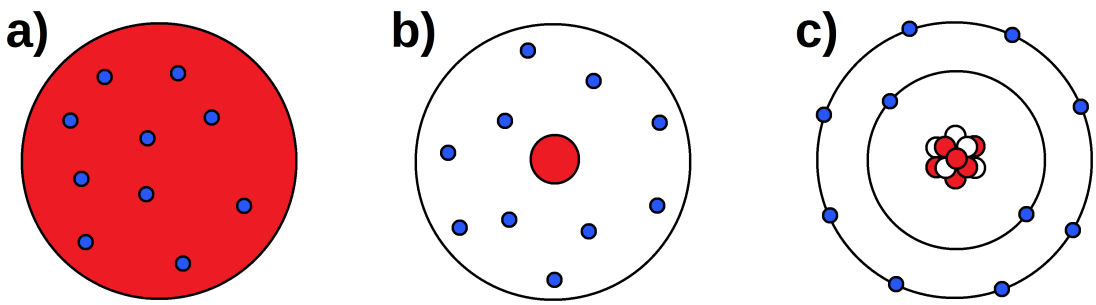

Figure 2: Evolution of atom models: a) Thomson model (1904): electrons embedded in a sea of positive electric charge; b) Rutherford model (1911): positive charge concentrated in a small center; c) (1932): protons and neutrons forming the nucleus, shells of electrons

Using from what had been learned from quantum mechanical principles, the nucleon picture spawned further insights like the semi-empirical mass formula [4] or the nuclear shell model [5]. However, it was not until about 1970 that the substructure of the nucleons could be revealed or the nature of the tying nuclear force that so easily overcomes electromagnetic repulsion and yet seemed so uninvolved in all previous physical phenomena.

Yukawa's Pion Exchange Model

An early concept for the mechanism behind the nuclear bonding was formulated by H. Yukawa in 1935. He imagined an exchange particle that carries the force between nucleons like a photon carries the electromagnetic force between electric charges. In order to account for the limited range of the nuclear force, he assumed this exchange particle to have a mass *200 times as large as the electron mass* ($\approx 100\,\mathrm{MeV}/c^2$) [6]. The model received approval when this particle – the pion – was found in atmospheric cosmic rays (fig. 3).

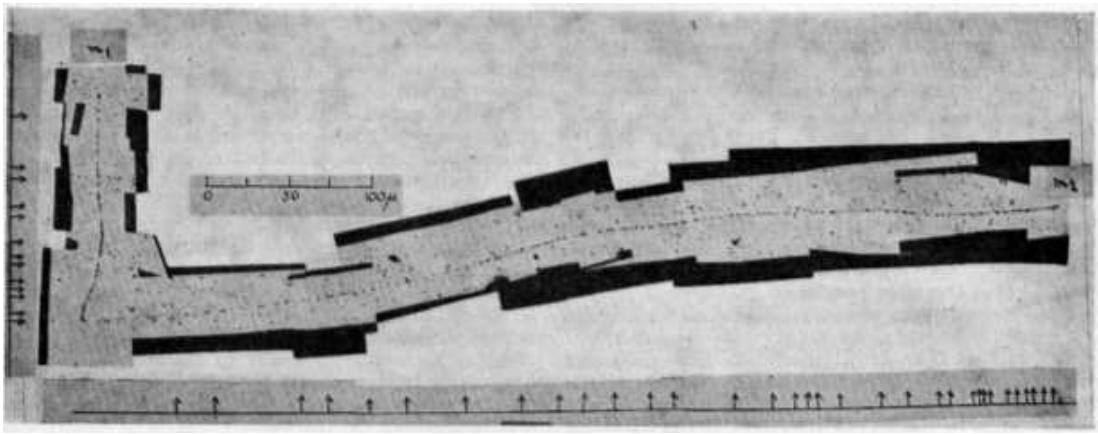

Figure 3: The pion in this picture of an emulsion enters from above and decays into a muon that goes right. The momentum of the muon is balanced by a neutrino that leaves no trace due to its vanishing interaction probability [7].

The Particle Zoo and the Quark Model

The pion has also been artificially produced in a cyclotron experiment in 1948, which launched the era of particle accelerators that, in addition to cosmic ray observations, would come up with a whole *zoo* of short lived strongly interacting particles. Their production and decay properties offered quantum numbers (e.g. isospin, strangeness) under which the particles could be arranged in patterns (multiplets) of group-theoretical origin (e.g. fig. 4) [8][9]. A major implication of the new classification scheme was the existence of *quarks* being the elementary building blocks of *hadrons* (i.e. strongly interacting matter). Assuming three types of quarks (*up*, *down*, *strange*) with electric charges (2/3, −1/3, −1/3) and spin 1/2, every known type of hadron could be constructed as a *baryon* (consisting of three quarks), *antibaryon* (three antiquarks) or *meson* (quark-antiquark). However appealing the idea, there were no free quarks to be seen in the experiments.

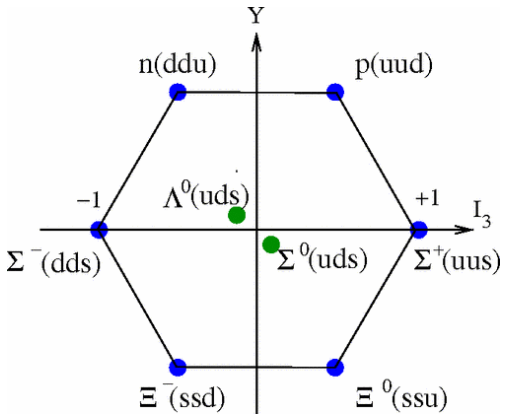

Figure 4: Spin-1/2 Baryons ordered by Strangeness and the third Isospin component [10]

Nucleon Substructure

Although quarks were not to be produced by means of brute force particle disintegration, evidence finally showed up around 1970 with the deep-inelastic scattering of electrons against nucleons [11]. With electron energies up to 25 GeV it was possible to probe the internal structure of nucleons and to make some decisive observations in favor of the quark hypothesis. The kinematic properties of the scattered electrons suggested that the nucleon contributed predominantly a certain fraction x of its four momentum to the scattering hinting at constituents that were scattered against elastically (fig. 5).

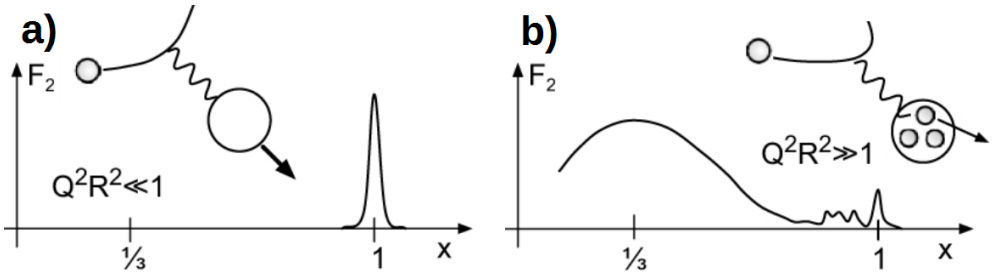

Figure 5: Comparison of elastic and deep-inelastic scattering: a) the momentum of the exchanged photon is low, respectively its wavelength is larger than the size of a nucleon and the electron scatters elastically against the whole nucleon; b) the momentum transfer is high enough and the photon's wavelength much smaller than the nucleon's radius; the elastic scattering against quarks is dominant, leading to a peak that is smeared due to the quarks's fermi motion [11].

Though the structure functions depended on this fraction of the nucleon's four momentum that is *seen* by the exchanged virtual photon, they did not depend on the four momentum transfer Q^2 implying that the constituents are pointlike (fig. 6 a)). Moreover, it was found that the constituents carry a spin 1/2 comparing the magnetic and the electric contributions of the interaction.

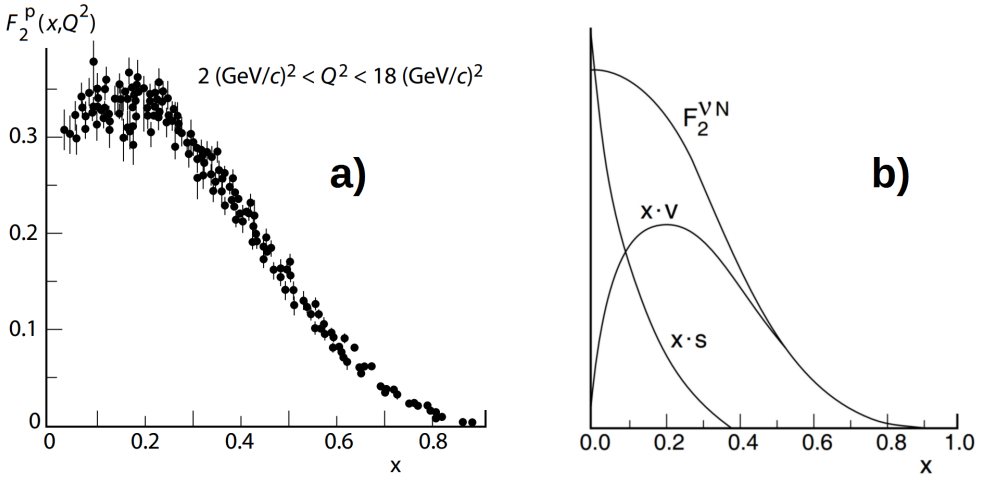

Figure 6: a) structure function F_2 of the proton for various momentum transfers Q^2 [12]; b) schematic illustration: structure function of the nucleus F_2 from deep-inelastic neutrino scattering; momentum distribution of valence (v) and sea (s) quarks, weighted with x [11].

Complementary measurements with deep-inelastic neutrino scattering seemed to give the final blessing to the quark model as they verified the fractional charges of the constituents. But in return they offered a glimpse into the dynamic processes within the nucleon, about which the static quark model does not say a word.
In contrast to electron scattering, the scattering of neutrinos against quarks can also break down the nucleon's share of quarks and antiquarks. This is due to the weak coupling involved that acts selectively on charge and helicity. Combining the results of electron and neutrino deep-inelastic scattering, one can distinguish two kind of quarks. There are three *valence quarks* that account for the quantum numbers of the nucleon and may in that sense be identified with the quarks that M. Gell-Mann and G. Zweig had in mind. Besides, there are quark-antiquark pairs called *sea quarks* that appear as short lived virtual particles. Their quantum numbers effectively cancel out, but as they contribute sources of charge, they do appear as impactor in the deep-inelastic scattering (fig. 6 b)).

Gluons

Momentum contributions of quarks and antiquarks raised an issue: As it turned out they only accounted merely for a half of the nucleon's momentum which led to the question what else there might be, insensible to the electromagnetic/weak coupling of electrons/neutrinos. The answer was included in the theory of quantum chromodynamics (QCD), the quantum field theory of the strong interaction, which proposed the *gluon* particle as the force carrier between quarks. Five years after its emergence, QCD received major approval when the discovery of the gluon was announced in 1979. It was found in lepton collisions producing quark-antiquark pairs with the occasional appearance of a gluon, analogous to the Bremsstrahlung known from the electromagnetic interaction (fig. 7).

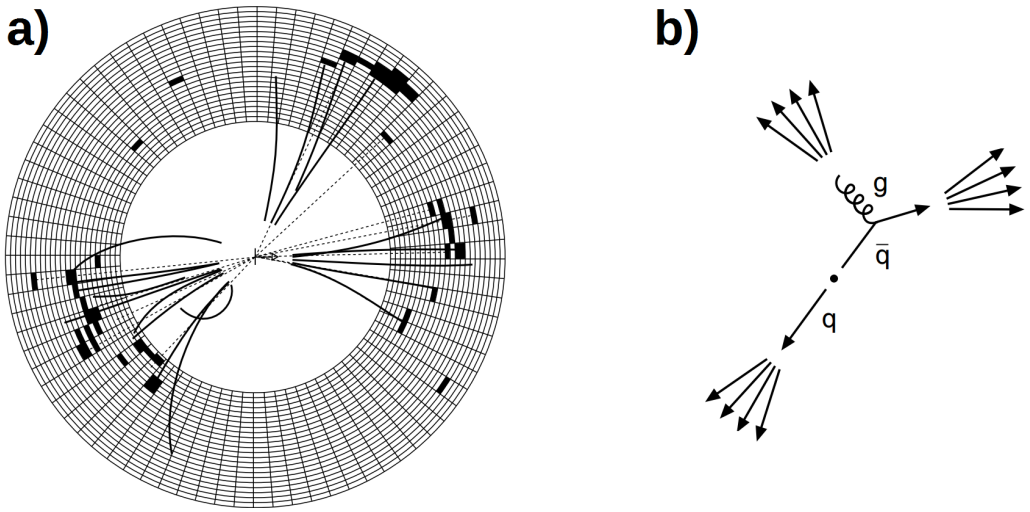

Figure 7: a) three-jet event measured with the JADE detector at the PETRA e^+e^- collider; b) three-jet event explained as gluon Bremsstrahlung; (anti-)quarks and the gluon eventually turn into a spray of hadrons measured in the detector [11].

1.2 QUANTUM CHROMODYNAMICS

The theory of quantum chromodynamics (QCD) is the field theory of the strong interaction. QCD follows physical principles that had already been introduced with quantum electrodynamics (QED) and introduced itself new features in order to match the somewhat strange nature of the strong force. In that sense, it is instructive to study the basic features of QED and to compare them to QCD.
By the end of the 1920s, quantum mechanics came to fruition. Classically measured quantities were replaced with quantum mechanical operators that had to be applied on the wave function of a particle. Following that way, quantum mechanics achieved to account for the wave-particle duality of particles and for the quantisation of energies. The subsequent approach was to quantize fields as well by employing field operators. The classical manifestation of fields – the forces – were now explained in terms of gauge bosons mediating the force between charges. The first theory of this kind was QED with the photon as the force carrier that couples to electric charges. In QED, contributions to any electromagnetic process can be illustrated with *Feynman diagrams*. The basic entities therein are the photon, the electric charge and their coupling, i.e. the electromagnetic vertex (fig. 8).

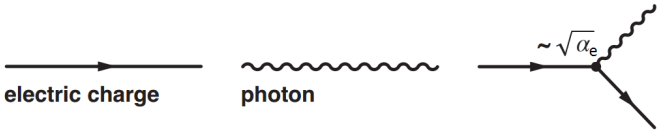

Figure 8: Elementary QED Feynman diagrams [13].

As an example, fig. 9 illustrates the QED interpretation of the Compton effect, the scattering of a photon against an electron (or any electric charge). One can also imagine a photon to be emitted and absorbed by the same electric charge or the case of vacuum polarisation, i.e. a photon breaking up into a positron-electron pair, which is allowed in the limits of the time-energy uncertainty. Obviously, one may equip a Feynman diagram with any (even) number of electromagnetic vertices and would still account for the same physical outcome (fig. 10). However, the electromagnetic coupling strength α_e involved in an electromagnetic interaction is way below unity ($\alpha_e \approx 1/137$) making successive electromagnetic vertices improbable. The contributions of higher order Feynman diagrams vanish accordingly. The series expansion of all contributions can be cancelled at some point, which makes perturbation theory possible.

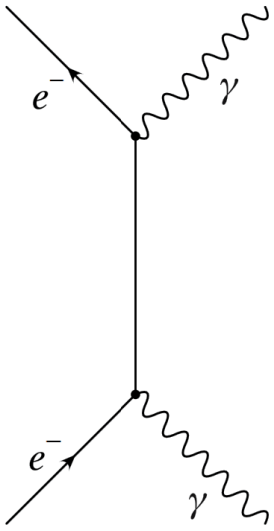

Figure 9: One QED contribution of the Compton effect [14].

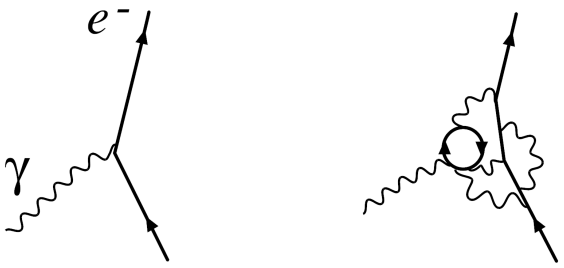

Figure 10: Two Feynman diagrams that depict the same process with different couplings involved, i.e. for different orders of α_e [14].

Similar to the electric charge and the photon of the QED, quantum chromodynamics assumes for the strong interaction a *color* charge and the *gluon* as the force carrying gauge boson. In contrast to the photon, the gluon itself carries a color charge which implies the possible coupling of the gluon to another gluon (fig. 11).

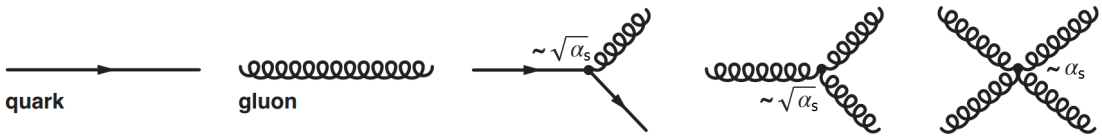

Figure 11: Elementary QCD Feynman diagrams [13].

As it was not curious enough, the strong interaction involves three types of color charges *red, green, blue* rather than the one type known from electromagnetism. A gluon carries a color and an anticolor giving an octet of possible gluons and a colorless singlet which is ignored as it is not found in nature. Neutralisation of color charges (i.e. a *white* color state) can be achieved by any combination of a color and its anticolor or the combination of (anti-)red, (anti-)green and (anti-)blue (there you get the analogy from additive color). With quarks (q) as fundamental particles carrying one color each, the *white* combinations of them are *mesons* ($q\bar{q}$), *baryons* (qqq) or *anti-baryons* ($\overline{qqq}$). One can imagine further colorless combinations like pentaquarks states ($qqqq\bar{q}$) whose existence is subject of an ongoing debate [15].

The fact that only a color singlet can exist as a free particle is refered to as *hadronic confinement*. It accounts for the observation that free quarks or gluons do not appear and has its cause in the QCD potential. In contrast to the electromagnetic potential or the gravitational potential which go with the inverse of the distance, the force between color charges rises with the distance. In that way, two quarks departing from each other will form a *gluonic flux tube*, similar to the string force of a spring, where the increasing potential energy will eventually give rise to quark and antiquarks so that colorless states are formed (fig. 12).

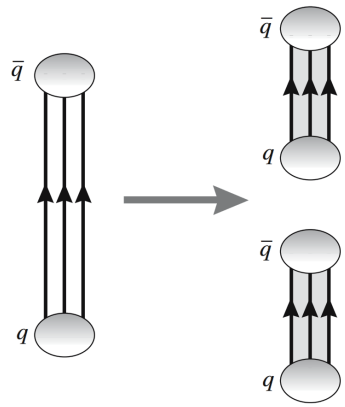

Figure 12: Hadronization in the chromoelectric field between two quarks [14].

With the nature of the strong interaction comes a major constraint on the usability of the theory. In contrast to the electromagnetic coupling strength $\alpha_e \approx 1/137$ the coupling strength α_s of the strong force is typically of the order of 1 preventing the appliance of perturbation theory. Luckily however, α_s depends on the momentum transfer involved and can indeed assume values ranging near zero for a high energy scale, which is called *asymptotic freedom* (fig. 13).

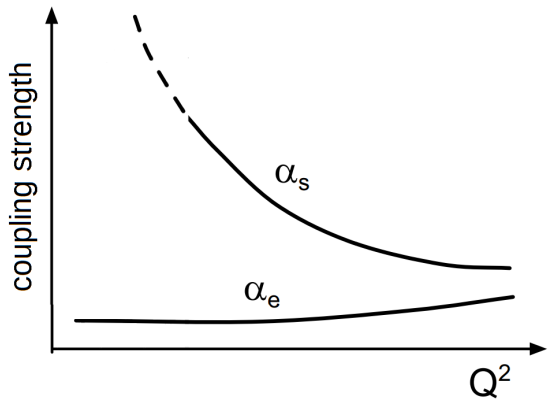

Figure 13: Schematic running of the coupling strengths α_s, α_e as a function of the momentum transfer [11].

The running of the coupling strength occurs due to a possible fluctuation of gluons that increases the effective charge seen at larger distance, respectively low momentum. To a lesser degree this also applies to the electromagnetic interaction, where vacuum polarisations screen a charge with increasing distance resulting in the inverse effect.
First order pertubation theory delivers the following dependence of the momentum transfer Q^2:

$$\alpha_s(Q^2) \quad = \quad \frac{12\pi}{(33 - 2n_f)\ln(Q^2/\Lambda^2)} \,, \tag{1}$$

where n_f is the number of involved quark species and Λ is the free scale parameter of the QCD. The shape of eq. 1 is confirmed by various observations (e.g. e^+e^- or Z^0 event shapes) with $\Lambda \approx 200\,\text{MeV}$ [16].
For a coupling strength $\alpha_s \ll 1$ the strong interaction in fact resembles the electromagnetic interaction in the sense that exchanges of a single boson prevail. The corresponding Coulomb-type potential can be found for instance in the model of heavy quarkonia, i.e. bound states of heavy quarks and antiquarks that involve small orbits. With the addition of the linear long range force the quark-antiquark potential is given by

$$V(R) = \frac{4\alpha_s(R)}{3R} + kR \,. \tag{2}$$

For scenarios where a large α_s does not allow pertubation theory, one can fall back on models that simplify the physical reality for the sake of manageability. An example would be the pion-exchange model of Yukawa mentioned earlier that accounts for the nuclear force as a residual interaction of the strong force. A prominent method however that can take into account the fundamental QCD processes is given by *Lattice*

Gauge Theory which uses finite-dimensional path integrals involving massive numerical calculations. This approach reproduced for instance the masses of mesons and baryons (fig. 14) and supplies the development of the flux-tube modeled QCD potential [17].

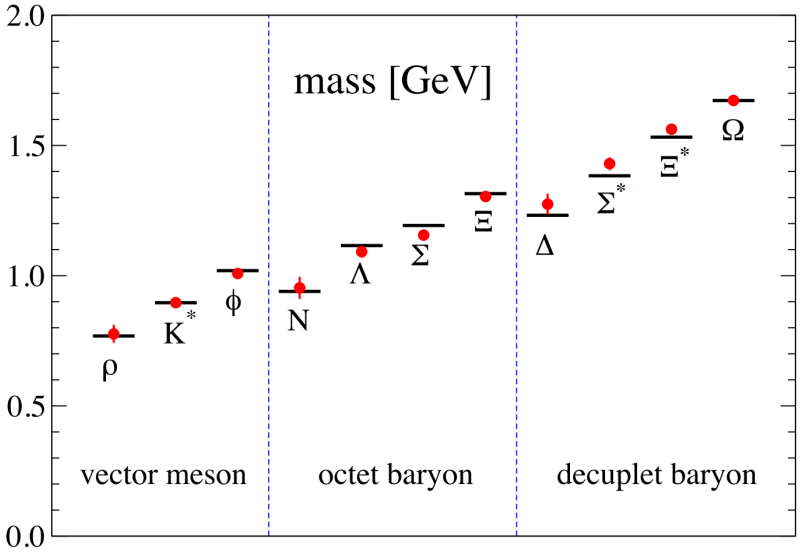

Figure 14: Masses of hadrons (dots) as calculated from Lattice Gauge Theory, lines depict experimental data [18].

1.3 QUARK-GLUON PLASMA

Heating up normal molecular matter will eventually lead to the formation of a plasma, where the atomic bonding between electrons and ions vanishes. As quarks and gluons are considered the building blocks of hadrons, one can readily anticipate a similar scenario in the regime of the strong force. It is considered that normal nuclear matter can be heated or compressed to a point, where the hadron wave functions overlap and the constituents are allowed to overcome their hadronic boundaries. With the temperature T as the scale parameter, the quarks and gluons tend to be asymptotically free with

$$\alpha_s(T) \propto \frac{1}{\ln(T/\Lambda)} \,. \tag{3}$$

Prior to the emergence of QCD, thermodynamic considerations already suggested an upper limit for the temperature of hadronic matter, the *Hagedorn temperature* $T_H \approx 150 - 200\,\mathrm{MeV}$. Lattice QCD calculations confirmed this temperature regime for the transition from hadronic matter to a QGP. It is however instructive to explore some properties of the QGP from a simplified picture, the *bag model*, which retains the two key features of asymptotic freedom and confinement [1].
The bag model assumes hadrons to be spherical bags with a volume V and radius R in a perturbative vacuum where the quarks are considered free particles. The kinetic pressure of the quarks is balanced by the *bag pressure* B accounting for their confinement. In that sense, B represents the difference between the true QCD vacuum pressure and the perturbative vacuum pressure. The energy E of the bag now

consists of the kinetic energy of the $N = 3$ quarks and the bag volume energy $B \cdot V$ needed to create the perturbative region:

$$E = \frac{2.04\,N}{R} + B\frac{4}{3}\pi R^3 \tag{4}$$

Identifying E with the proton mass, R with the proton radius and applying the stability criterion $dE/dR = 0$, this relation yields a value of $B^{1/4} \approx 220\,\text{MeV}$.
Assuming an ideal gas of massless quarks the pressure P of the QGP is linked to the temperature T via the Stefan-Boltzmann form

$$P_{QGP} = \left(2 \cdot 8 + \frac{7}{8}(3 \cdot 2 \cdot 2 \cdot 2)\right)\frac{\pi^2}{90}T^4 - B = 37\frac{\pi^2}{90}T^4 - B, \tag{5}$$

where the prefactors account for the degrees of freedom from spin $(2)^1$ and color $(8, 3)$ degeneracy of gluons and quarks. Further factors for the quarks consider the possibility of particles/antiparticles and the allowed quark flavors up/down as well as a factor $7/8$ for fermion statistics.
For the temperature regime of about 100 MeV, the hadron gas phase can be described as a pion gas with only three degrees of freedom for the three charge states of the pion:

$$P_\pi = 3\frac{\pi^2}{90}T^4 \tag{6}$$

At the point of phase transition, both P_π and P_{QGP} are the same (fig. 15 a)), delivering a critical temperature $T_C \approx 160\,\text{MeV}$. Due to the several degrees of freedom in a QGP the energy density ϵ rises accordingly (fig. 15 b)).

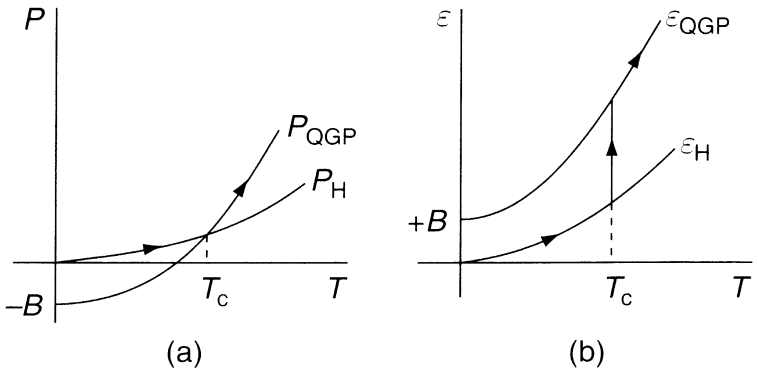

Figure 15: a) pressure P and b) energy density ϵ for a hadron gas and for the bag modelled QGP [1].

1 Massive spin-1 particles have three polarisation states, massless gauge bosons only have two (transversal) polarisation states.

Fig. 16 shows calculations from Lattice Gauge Theory. Besides the sudden rise in ϵ at critical temperature one notices that the energy density remains under the Stefan-Boltzmann prediction for an ideal gas of massless constituents. The difference gives a measure of the remaining interaction of the constituents.

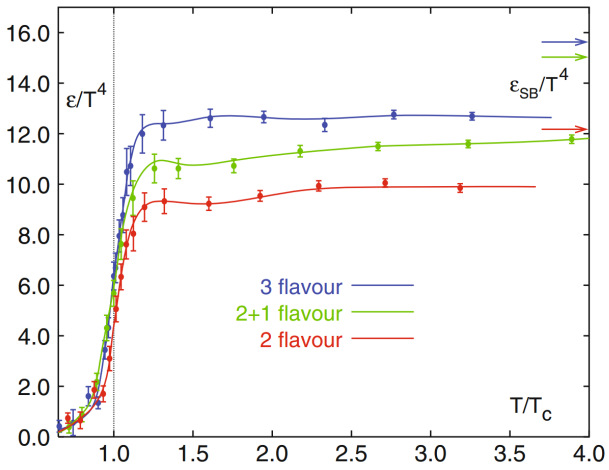

Figure 16: Energy density calculated for two light quark flavors, three light quark flavors and two light plus one heavy quark flavor [19].

While the bag model suggests a first-order phase transition, ongoing studies show that the nature of the transition is more complicated. Assuming quark masses $m_q \to 0$ or $m_q \to \infty$ a first order transition is in fact expected, but the point with the physical quark masses seems to fall in a region of a rapid *crossover* transition (fig. 17).

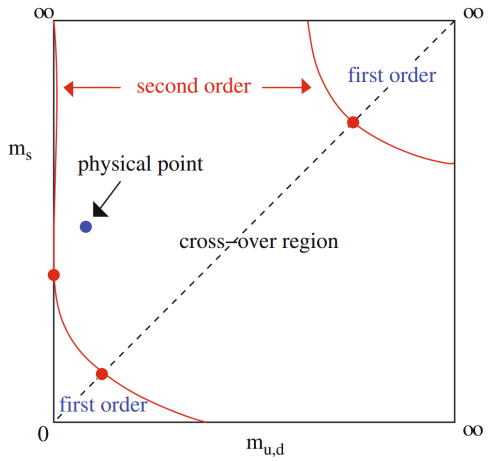

Figure 17: Nature of the QGP transition for varying quark masses [20].

The considerations above involve the simplification that the *baryochemical potential*[2] μ equals zero. Accounting for a non-vanishing μ, there may be a tricritical point μ_t (w. r. t. T, μ, m_q) and again a first-order transition for $\mu > \mu_t$.
While μ is about 940 MeV for ordinary nuclear matter, the baryochemical potential is significantly lower in ultrarelativistic heavy-ion collisions, where the nuclei typically

2 Besides the temperature T and the volume V the baryochemical potential μ is the third component of the grand potential $\Omega(T, V, \mu)$. μ is a measure of the net baryon density.

pass through each other leaving the produced matter with high energy density and low net baryon density behind.
To increase μ means to increase the baryon density which can also lead to the formation of a QGP, as nucleons will simply overlap by close packing. A manifestation of this scenario can presumably be found in neutron stars. Similar to an electric superconductor one also expects a color superconducting phase in this region, where quark pairs form cooper pairs. Unfortunately there is no possibility in sight to reproduce these conditions on earth.
Concluding, fig. 18 depicts a schematic of the QCD phase diagram.

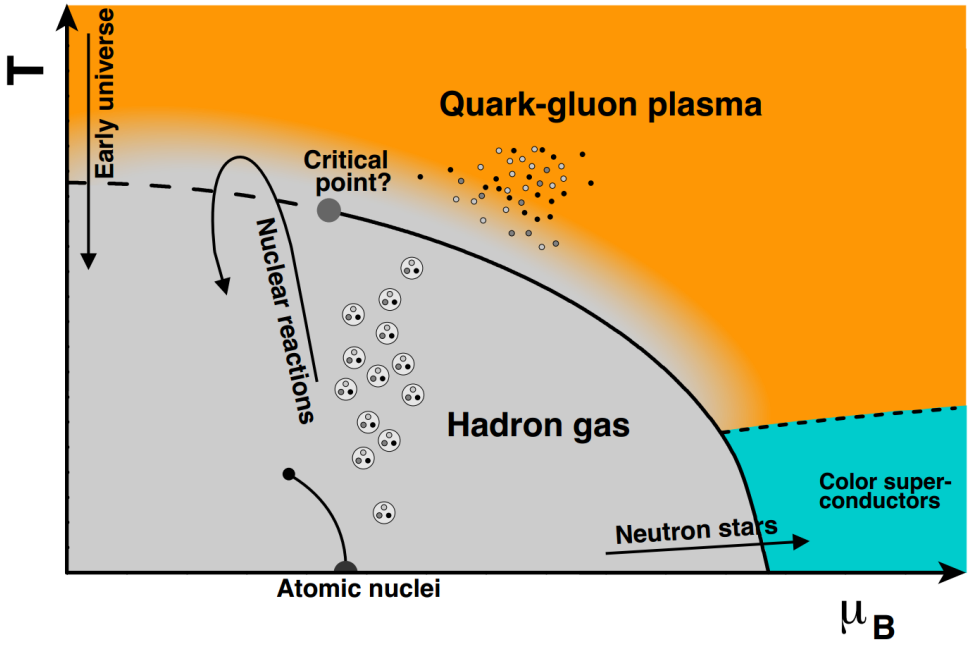

Figure 18: Schematic QCD phase diagram [13].

2

HEAVY-ION COLLISIONS

The following sections give an overview over ultrarelativistic heavy-ion collisions. Concluding, it is shown how jets are used to probe the QGP.

2.1 BASIC OBSERVABLES/PARTICLE SPECTRA

Momentum distributions of particles are treated separately for the longitudinal direction defined by the beam axis and the transverse direction. For the latter one simply employs the *transverse momentum* p_T, while it is convenient to use the *rapidity* y to express the longitudinal component p_Z:

$$y = \frac{1}{2} \ln \left(\frac{E + p_Z}{E - p_Z} \right) \tag{7}$$

Here, the energy of a particle is E. The rapidity y is an additive quantity considering longitudinal Lorentz boosts, i.e.

$$y' = y - y_{\text{Boost}} = y - \frac{1}{2} \ln \left(\frac{1 + v_Z/c}{1 - v_Z/c} \right) , \tag{8}$$

with y' the resulting rapidity, when the frame of y undergoes a Lorentz boost along the beam axis with a velocity v_Z. Under such a transformation a particle distribution dN/dy will likewise remain its shape.
The rapidity receives a somewhat tangible interpretation for the limit of large momenta or vanishing rest masses ($E \approx p$):

$$\lim_{p \to E} y = \frac{1}{2} \ln \left(\frac{p + p_Z}{p - p_Z} \right) = \frac{1}{2} \ln \left(\frac{1 + \cos\theta}{1 - \cos\theta} \right) = -\ln \tan \frac{\theta}{2} =: \eta \tag{9}$$

In this form, the rapidity is called *pseudorapidity* η and depends only on the angle θ between the particle and the beam axis. If the centre-of-mass frame coincides with the lab frame, the direction perpendicular to the beam line is called mid-rapidity with $\theta = 90°$ and $\eta = y = 0$. The value of η tends to infinity approaching the beam line ($\theta = 0°$). Considering the common outcome of hadron collisions with particle energies $\gtrsim 1\,\text{GeV}$ and the bulk of particles being pions ($m \approx 140\,\text{MeV}/c^2$), it is usually justified to employ the pseudorapidity η for its experimental accessibility; particle identification is not required.
With η accounting for the polar angle θ, the azimuthal angle φ completes the geometric description of particles originating from the point of collision, the *primary vertex*. One additional quantity is the radius R that is defined as a length on the φ-η-plane. Accordingly, the distance between two points i, j on the φ-η-plane is

$$\Delta R_{ij} = \sqrt{(\varphi_i - \varphi_j)^2 + (\eta_i - \eta_j)^2} \, . \tag{10}$$

As the distance between particles can account for their interrelation, the radius R is a relevant quantity for the analysis of particle jets.

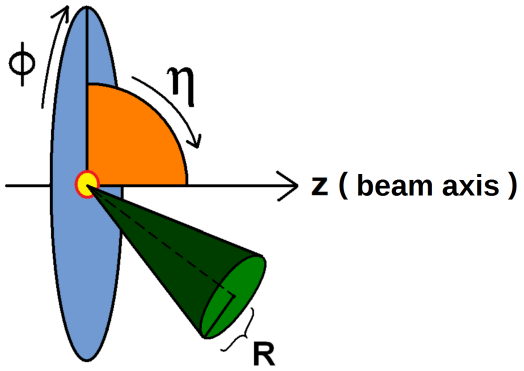

Figure 19: Geometric quantities describing outgoing particles [21].

With the kinematic and geometric terms at hand, one can now quantify the results of hadron collisions in the form of particle spectra. Besides the number of particles dN emitted in an interval of a certain quantity (e.g. dN/dy, $dN/d\eta$) a usual representation of a particle spectrum is the *invariant cross section*

$$E\frac{d^3\sigma}{dp^3} = \frac{d^3\sigma}{p_T d\varphi d\eta dp_T} . \tag{11}$$

Considering that only inelastic scatterings give rise to particles at sufficiently large angles covered by detectors, one measures the *inelastic cross section*. The cross section σ is related to the *reaction rate* r of a collider

$$r = \sigma L , \tag{12}$$

where L is the *luminosity* of the collider:

$$L = nf\frac{N_1 N_2}{A} \tag{13}$$

n is the number of bunches in one beam, f the revolution frequency, $N_{1(2)}$ the particle numbers in each bunch of beam 1(2) and A the intersecting area of the two beams. The luminosity L has the dimension of a flux $(1/(s \cdot cm^2))$ and represents a collider's ability to produce particle collisions. For instance, the affirmation of rarely produced particles like the Higgs boson depend on rich statistics and therefore on a large luminosity (fig. 20).

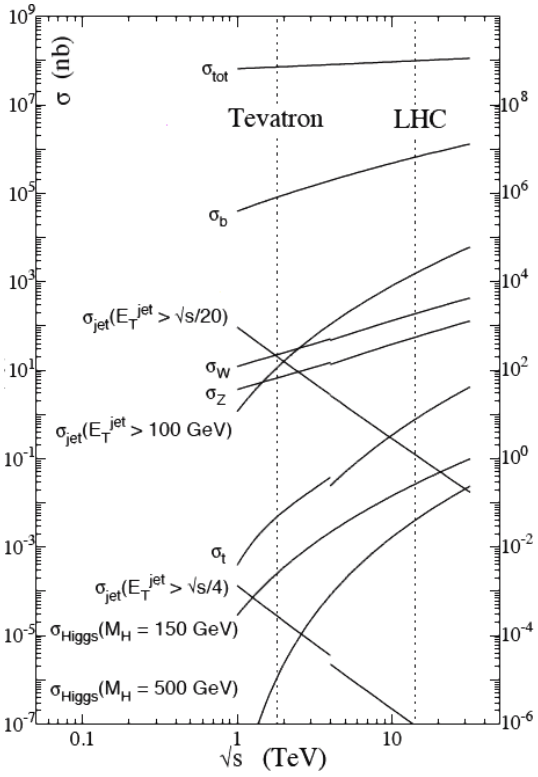

Figure 20: Events/s for $L = 10^{34}\,s^{-1}\,cm^{-2}$ (right axis); cross sections (left axis) [22].

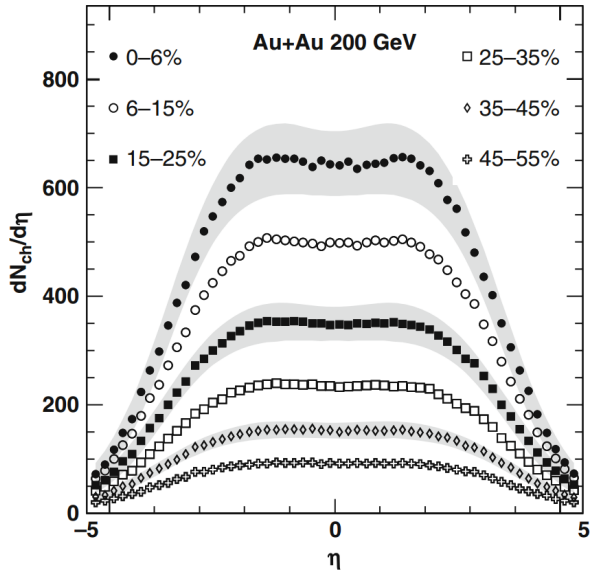

Figure 21: Pseudorapidity distribution $dN_{ch}/d\eta$ of charged particles for Au-Au collisions at $\sqrt{s_{NN}} = 200\,\text{GeV}$ [23].

To conclude this section, two typical distributions are exemplified in the following. Fig. 21 depicts the pseudorapidity distribution of charged particles measured in heavy-ion collisions at RHIC with $\sqrt{s_{NN}} = 200\,\text{GeV}$. The grey bands give the systematic uncertainty (90 % C.L.); statistical errors are smaller than the symbols. The distribution is shown for six classes of *collision centrality* (cf. section 2.3), from the most central (i.e. head-on) collisions (0-6%) to more peripheral collisions (45-55%). Naturally, a high collision centrality implies a high particle multiplicity.
A general feature of pseudorapidity distributions is the plateau around mid-rapidity – the *fragmentation region* – that declines for large $|\eta|$, where the lower energy transfer prevents the production of additional particles and elastic processes prevail. One typically finds a small depression of the yield around $\eta = 0$ that follows from the transformation $dN/dy \to dN/d\eta$. It is interesting to note that studies from RHIC [24] show a region of universal fragmentation: the curve up to approx. 90 % of the plateau height remains the same for various collision energies, when shifted by beam rapidity (fig. 22).

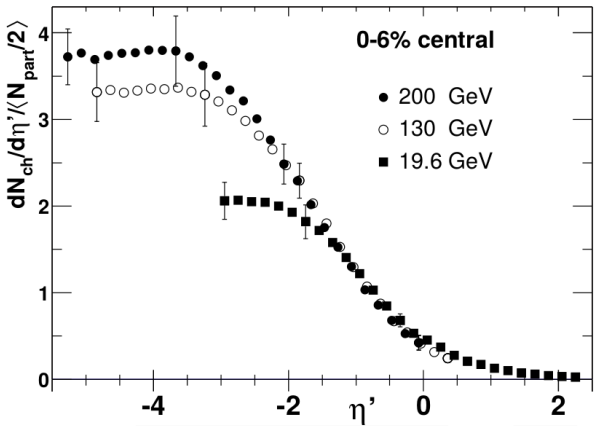

Figure 22: Charged particle multiplicity per participant pair in central Au-Au collisions for different collision energies with $\eta' = \eta - y_{beam}$ [24].

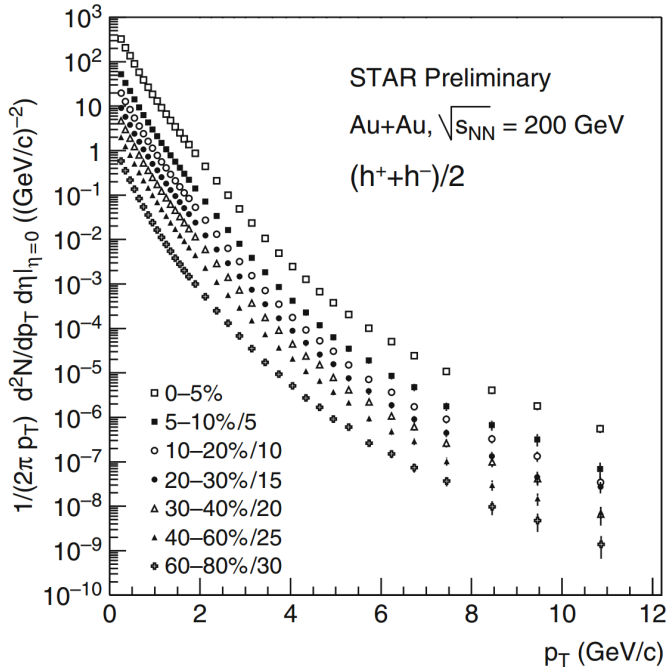

Figure 23: Transverse momentum spectra of charged hadrons in Au-Au collisions at $\sqrt{s_{NN}} = 200\,\text{GeV}$ for different collision centralities [25].

Fig. 23 shows a typical transverse momentum distribution of charged hadrons. The results are again depicted for various collision centralities and scaled for better visibility. A characteristic of such a hadron spectrum is the logarithmic scale and the steeply falling curve. It begins with a Boltzmann-like thermal spectrum of *soft* particle production for ($p_T < 2\,\text{GeV}/c$):

$$\frac{1}{p_T}\frac{dN}{dp_T} \propto e^{-\alpha p_T} \quad \text{with } \alpha \approx 1/(600\,\text{MeV}/c) \tag{14}$$

The curve descends into the high-p_T regime with a power law according to the Rutherford-like scattering of *hard* partons:

$$\frac{1}{p_T}\frac{dN}{dp_T} \propto (p_0 + p_T)^{-n} \tag{15}$$

The exponent n varies for different collision energies, e.g. $n \approx 9.8\ (6.0)$ at $\sqrt{s} = 62.4\,\text{GeV}$ (7000 GeV) for p-p collisions. p_T-spectra of heavy-ion collisions are additionally modified by collective flow which is covered e.g. by the phenomenological *Blast-wave model* [26].

2.2 A+A COLLISIONS AND THE QGP EVOLUTION

With the high energy scale of ultrarelativistic hadron collisions the nucleon in its entirety is no longer considered subject to the scattering, but the constituting partons, i.e. the quarks and gluons. The corresponding reaction model for nucleus-nucleus (A+A) collisions is called the *Bjorken picture* [1][27].

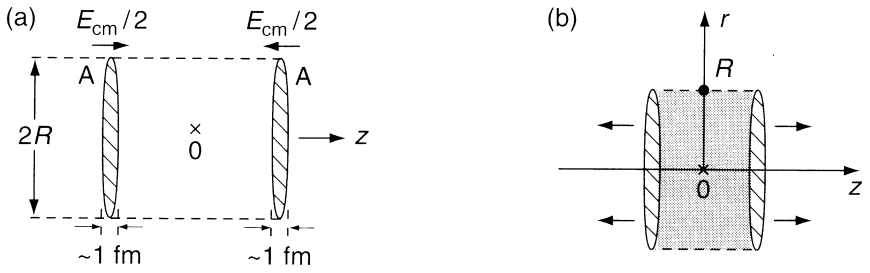

Figure 24: Bjorken picture of ultrarelativistic heavy-ion collisions: a) two nuclei approach each other; b) the nuclei pass through each other, leaving behind highly excited matter with a small net baryon density [1].

Assume a head-on collision of two nuclei of the same mass A as it is depicted in fig. 24 a). In the center-of-mass frame they appear as Lorentz-contracted pancakes with a thickness $2R/\gamma$, where γ is the Lorentz factor. Owing to this contraction, the nuclei would basically pass through each other were it not for the existence of sea quarks and soft gluons (wee partons), which carry a much smaller momentum fraction than the valence quarks. The wee partons can be seen as QCD vacuum fluctuations that couple to the fast moving valence quarks. Due to the uncertainty principle, the minimal longitudinal size of the wee partons is approximately $1/\Lambda_{QCD} \approx 1\,\text{fm}$, which exceeds the longitudinal size of the Lorentz-flattened valence quarks wave function in the case of $\gamma > 2R/(1\,\text{fm})$. As a result, the wee partons are responsible for the bulk energy deposition in ultrarelativistic heavy-ion collisions (fig. 24 b)).

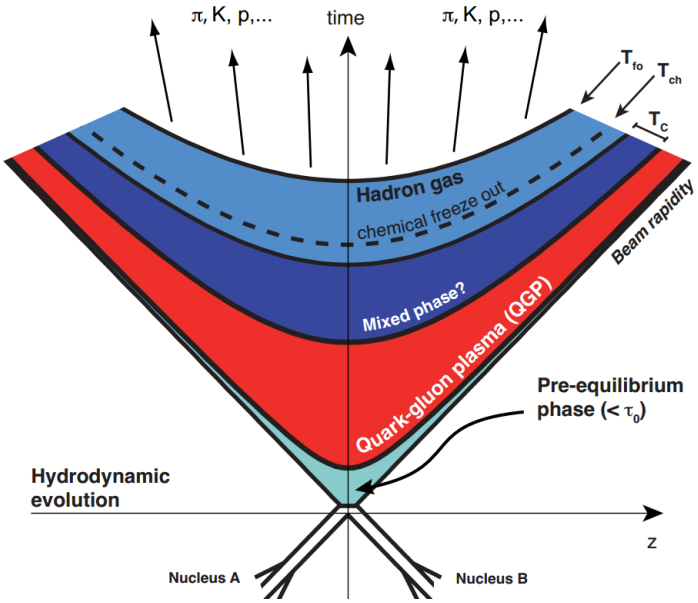

Figure 25: Space time evolution of a heavy-ion collision; the phase-boundaries are curves of constant proper time $\tau = \sqrt{t^2 - z^2}$ [13].

After a certain proper *decoherence time* τ_{de} the excited virtual quanta de-excite to real gluons and quarks. Following the Lorentz time dilation for each quantum as seen in the centre-of-mass frame, faster particles emerge later and farther away from the collision point (fig. 25). Within the *equilibration time* $\tau_0 > \tau_{de}$ quarks and gluons are expected to constitute an equilibrated QGP.
Due to the supposed crossover nature of the transition (see section 1.3) one expects a mixed phase before the decreasing temperature allows the formation of hadrons. With further cooling inelastic processes will cease and the particle species will be fixed (*chemical freeze out*). As soon as elastic interactions vanish, the kinematic properties become definite, too (*freeze out*), and so does the overall picture the detectors will take from the collision. The system reaches freeze-out after approx. 10 fm/c with a volume of about 5000 fm^3, estimated from *pion femtoscopy* for head-on heavy-ion collisions at the Large Hadron Collider (LHC) [28].
An important quantitative result of the Bjorken picture is the estimate of the initial energy density ϵ_0 from the particle multiplicity dN/dy at mid-rapidity [29]:

$$\epsilon_0 = \frac{m_T}{\tau_0 A}\frac{dN}{dy}\bigg|_{y=0} \quad \text{with} \tag{16}$$

$$m_T = m_0^2 + p_T^2 : \text{transverse mass (mostly pions)} \tag{17}$$

$$A : \text{overlapping area of the nuclei} \tag{18}$$

Accordingly, the energy density reached by Pb-Pb collisions at the LHC is presumably $\epsilon_{LHC} \gtrsim 15\,Gev/fm^3$ and therefore clearly above the critical energy density of the QGP transition $\epsilon_C \approx 0.5\,GeV/fm^3$ [30].

2.3 THE GLAUBER MODEL OF HEAVY-ION COLLISIONS

Colliding ions usually do not face each other head-on and one can readily anticipate different physics scenarios for different collision centralities. Despite the small length scale involved it is possible to have a measure for the collision centrality from experimental data and to extract the number of participating and colliding nucleons with the help of the *Glauber model* [31] [1].

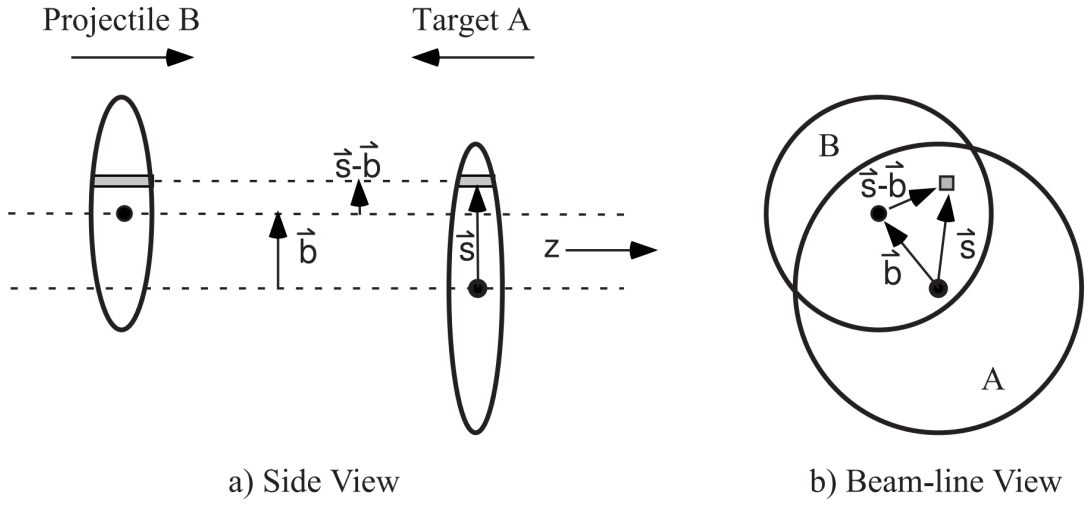

Figure 26: Glauber model geometry [31].

Imagine the encounter of two nuclei as it is depicted in fig. 26. Besides a possible electromagnetic interaction, that is only dominant for an *impact parameter* b much larger than the size of the nuclei, the nuclei interact mostly inelastically, when it comes to a geometrical overlap. The overlap is given by the *nuclear overlap function*

$$T_{AB}(\vec{b}) = \int d^2\vec{s}\; T_A(\vec{s})T_B(\vec{s}-\vec{b}) \tag{19}$$

with the *thickness function*

$$T_A(\vec{s}) = \int dz\; \rho_A(z,\vec{s})\,. \tag{20}$$

With an estimate of the nuclear mass number density ρ_A (commonly via Woods-Saxon parametrisation) and the inelastic nucleon-nucleon cross section σ_{NN} the Glauber model provides the number of participating nucleons N_{part} and the number of nucleon-nucleon collisions N_{coll}:

$$\begin{aligned} N_{part}(b) &= \int d^2\vec{s}\; T_A(\vec{s})\Big(1-\exp\left(1-\sigma_{NN}T_B(\vec{s})\right)\Big) \\ &\quad + \int d^2\vec{s}\; T_B(\vec{s}-\vec{b})\Big(1-\exp\left(-\sigma_{NN}T_A(\vec{s})\right)\Big) \end{aligned} \tag{21}$$

$$N_{coll}(b) = \int d^2\vec{s}\; \sigma_{NN}T_A(\vec{s})T_B(\vec{s}-\vec{b}) \tag{22}$$

Fig. 27 shows the curves of N_{part} and N_{coll} (here N_{binary}) depending on the impact parameter b in Au-Au collisions.

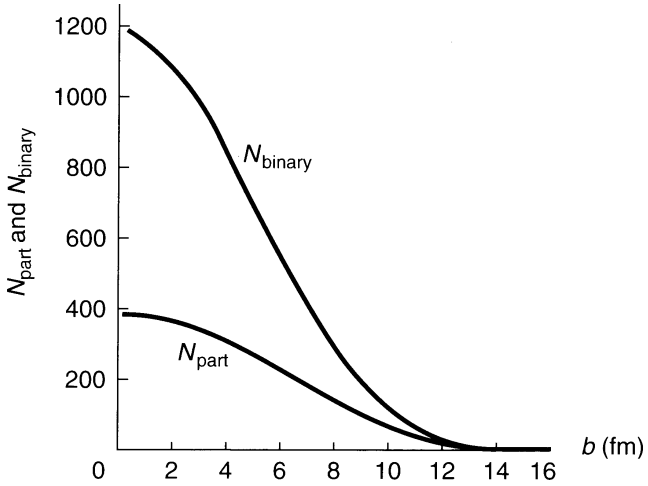

Figure 27: Number of binary collisions and participants as a function of the impact parameter in a Au-Au collision [1].

It is useful to keep in mind that soft processes (e.g. bulk particle production) scale roughly with N_{part} and hard processes (e.g. hard scattering of partons) scale with N_{coll}. One may therefore distinguish hard and soft contributions to the particle yield with

$$\text{yield} = f\cdot N_{coll} + (1-f)\cdot N_{part}\,, \tag{23}$$

where f gives the fraction of hard processes.

The usual approach to the Glauber Model are Monte Carlo (MC) calculations. The nucleons of the nucleus can be distributed according to a nuclear density function; the impact parameter b is randomly chosen from $d\sigma/db = 2\pi b$. Regardless of multiple scatterings the nucleons of the opposing nuclei encounter each other on straight lines and with a constant σ_{NN}. A hit between two nucleons can then occur, when a certain condition is met, e.g. the distance d between the centres of crossing nucleons lies within the radius of the cross section, $d \leqslant \sqrt{\sigma_{NN}/\pi}$.

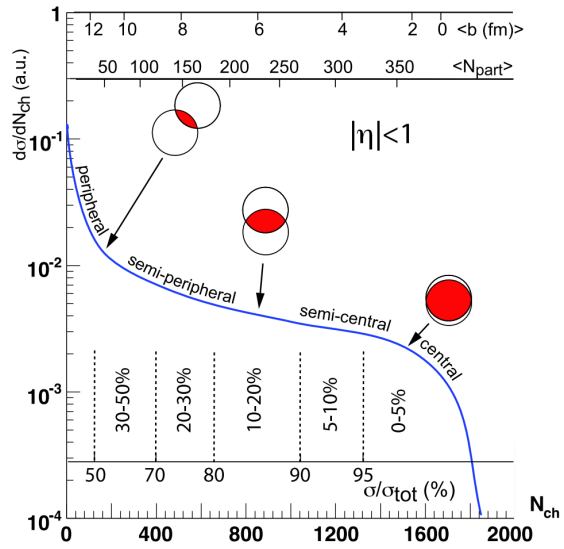

Figure 28: Particle multiplicity distribution plotted against Glauber MC quantities [31].

Assuming that the deposited energy increases with the centrality, one can accordingly assign a measure of centrality. Fig. 28 shows an ensemble of events that is simply mapped into centrality classes according to their share of the total yield.

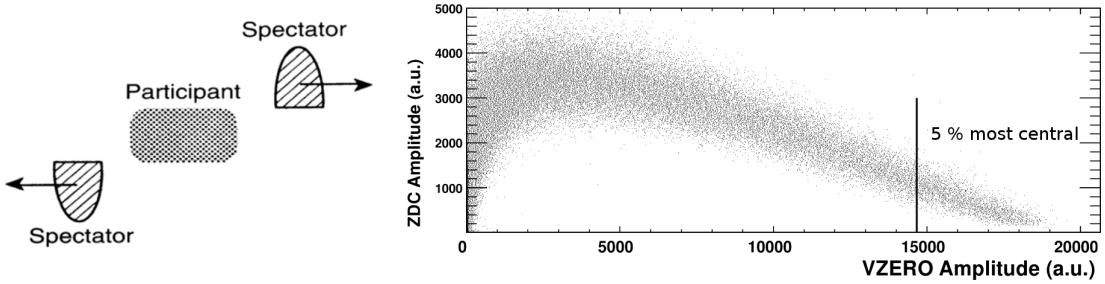

Figure 29: a) fragments uninvolved in the inelastic collision are called *spectators*, they keep their velocity and emerge at nearly zero degree [1]; b) from Pb-Pb collisions at ALICE: energy deposited by spectators (ZDC amplitude) vs. forward particle multiplicity (VZERO amplitude) [32].

Another way to determine the centrality is via the forward energy deposited by *spectator* nucleons (fig. 29 a)). Unbound neutrons surviving the collision will deviate on a straight line from the supposed beam path; their abundance will be smaller for more central collisions. Most peripheral collisions however will again yield a low number of unbound neutrons, as neutrons remain bound in deuterons or larger fragments (fig. 29 b)).

2.4 PROBING THE QGP

The most abundant source of information in ultrarelativistic heavy-ion collisions are the hadrons that emerge as a result of the bulk energy deposition. In the sense that these hadrons are the static thermal radiation of the QGP, they only provide information about the hadronic freeze-out, but not about the earlier stages. Fortunately, one can imagine a variety of other probes that offer insights into the QGP evolution between the initial stage and the freeze-out:

Electromagnetic Probes

The QGP medium also radiates electromagnetically. Photons can be emitted and escape the QGP without notable interference because of their low interaction probability. The electromagnetic radiation therefore captures the moment of their production. With photons produced at any stage of the expansion (fig. 30), the task is to disentangle the convolution of all electromagnetic sources.

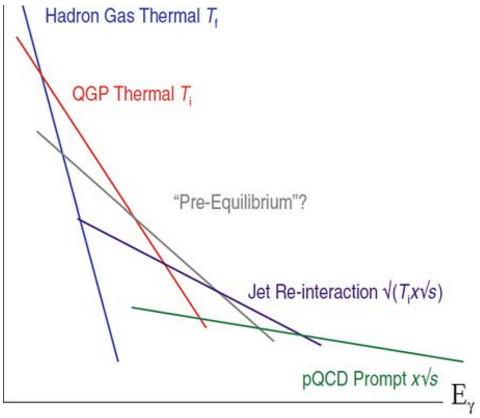

Figure 30: Various sources of *direct* photons [20].

Hydrodynamic Flow

Since there are no boundaries containing the hot and dense medium, the QGP will undergo an expansion that can be described by relativistic hydrodynamics. Besides an isotropic momentum boost (*radial flow*) one can imagine flow variations depending on the initial stage of the collision (fig. 31).

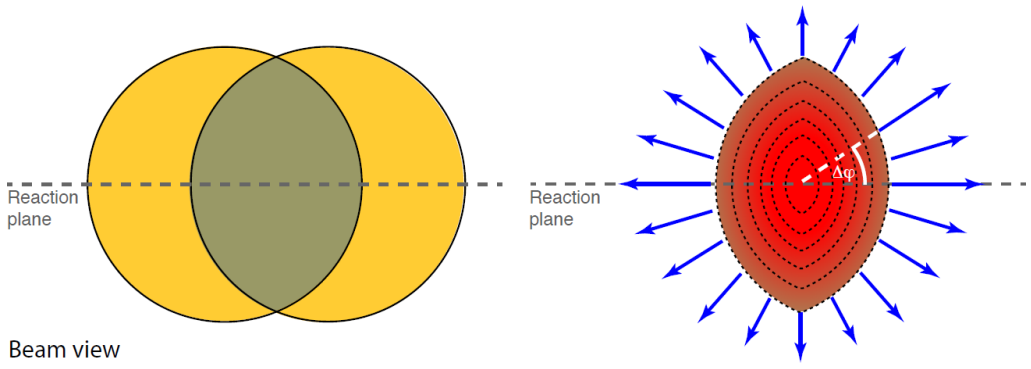

Figure 31: Anisotropic flow: a non-central collision gives a non-circular overlap, leading to an anisotropic pressure gradient (dashed lines indicate isobars) [13].

Quarkonia Suppression

In contrast to the light hadrons, heavy quarkonia ($c\bar{c}$ or $b\bar{b}$) are expected to survive the QGP phase transition up to a higher temperature. Embedded in a medium of free color charges the confinement part of the quark-antiquark potential (i.e. the long range term in eq. 2) vanishes and the remaining Coulomb potential receives a weakening from *color debye screening*. The characteristic screening radius depends on the temperature so that the various quarkonia species will successively *melt* at certain temperatures. Quarkonia spectroscopy can therefore serve as a thermometer of the QGP (fig. 32).

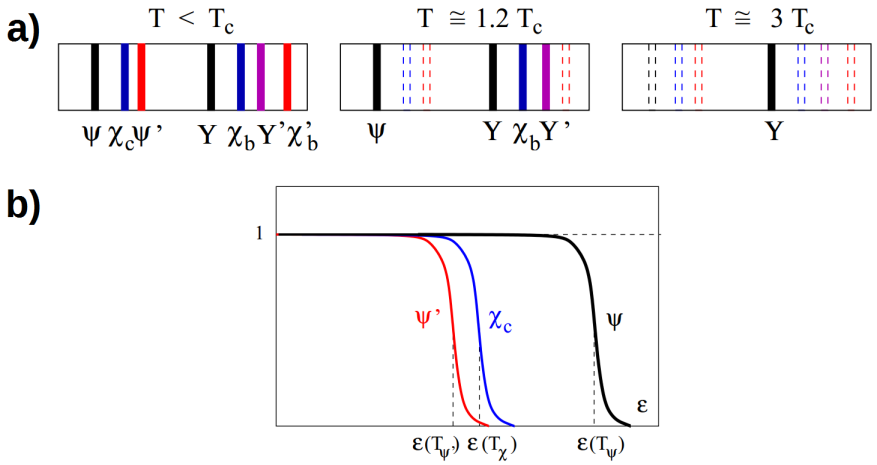

Figure 32: a) quarkonia spectral lines as a thermometer; b) charmonium survival probabilities vs. energy density [33].

This is just a selection of possible QGP probes. A more complete overview can be found in [1][20].

2.4.1 *Hard Scattering in a Medium*

Yet another QGP probe, that is used for the analysis in this thesis, are hard scattered partons that emerge in the early stage of the collision [34][20]. Traversing the dense color-charged medium these gluons or quarks undergo medium-induced modifications, an increased energy loss most prominently. The partons will appear in the detector as *jets* of particles into which they eventually hadronize. Comparing jets from central heavy-ion collisions (A-A) to jets from proton-proton collisions (p-p) or peripheral A-A collisions, one can quantify the influence of the medium.
Due to the large momentum transfer involved, hard scatterings occur on a short time scale of $\tau < 0.1\,\mathrm{fm/c}$. This allows a perturbative approach (pQCD) of the hard scattering process regardless of interference with the initial state given by the *parton distribution function* (PDF) and the evolution of the final state defined by the *fragmentation function* (FF). These contributions to the hard inelastic cross section are all sums of amplitudes – they *factorise*:

$$E\frac{d^3\sigma}{dp^3} = \int \mathbf{PDF} \otimes \mathbf{pQCD} \otimes \mathbf{FF} \tag{24}$$

While the partonic cross section can be evaluated up to any order of α_s from first principles, the parton distribution function and the fragmentation function need to be determined on an empirical basis. Their energy scale dependence however can be evaluated with the *Dokshitzer-Gribov-Lipatov-Altarelli-Parisi* (DGLAP) equation [35][36][37]. After the hard scattering – predominantly $2 \rightarrow 2$ and $2 \rightarrow 2 + X$ – the outgoing partons lose their energy mainly by medium-induced gluon emissions (fig. 33). In the aforementioned scheme the effect of this enhanced emission can be included in a medium-modified fragmentation function. At high energies, the collisional energy loss for gluons and light quarks is small; energy loss via Čerenkov and transition radiation is considered insignificant.

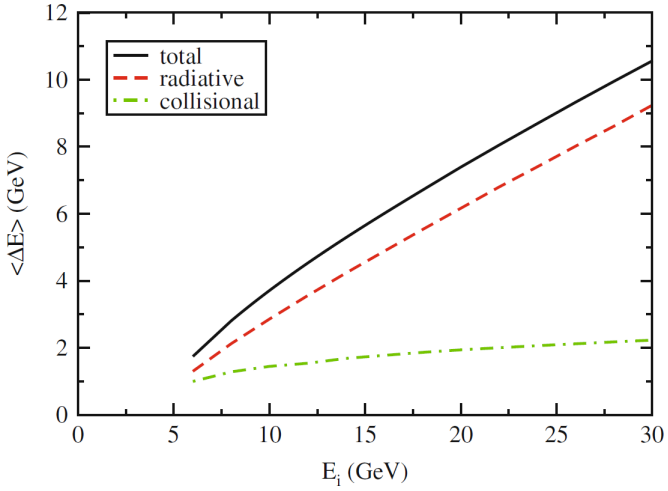

Figure 33: Comparison of collisional and radiative energy loss of light quarks with an initial energy E_i in the QGP environment for Au-Au collisions at RHIC [20].

For radiative energy losses one finds a hierarchical ordering of particle species:

$$\Delta E_{rad}(g) > \Delta E_{rad}(q) > \Delta E_{rad}(c) > \Delta E_{rad}(b) \tag{25}$$

Due to the larger color *Casimir factor*, gluon jets will lose more energy and are broader than jets of light quarks (u, d, s). Light quarks again radiate more energy than heavy quarks (c, b) due to the *dead cone effect* [38]. As a result, collisional energy loss is considered substantial for bottom and charm quarks. Top quarks are not considered subject to energy loss as they decay shortly after production ($\tau < 0.1\,\mathrm{fm/c}$).
Measurements of the parton energy loss are used to constrain theoretical predictions. The search for the right energy loss model however is difficult: Not only give the several properties of the plasma (e.g. medium thickness or temperature) room for interpretation, but also their evolution in time, which requires the correct understanding of the medium expansion.

2.4.2 *Jets*

An outgoing parton is not a physical observable. A somewhat easy approach is to take the leading hadron in an event as a proxy for the original parton. Ideally however, one deduces the parton properties from the properties of the whole jet, i.e. from all the fragments.
It is simple to summarise the four momenta of these particles and reconstruct the parton's four momentum, but how to say which particles stem from the original parton? How to tell them apart from the numerous particles of the soft background? And if one manages to do so: was the scheme guided by physics in a way that the results can be calculated and understood from basic principles?
There are various *jet clustering algorithms* and each one comes with an own scheme, often for a specific application (e.g. identifying b-quark jets). It thus becomes clear that a jet is a designed observable and can only with the proper consideration be related to a physical entity such as the energy of an outgoing parton.
One distinguishes two classes of jet clustering algorithms: Given a certain measure of distance, *sequential recombination algorithms* successively combine particles close to each other, delivering a hierarchical clustering of particles up to a defined limit. *Cone algorithms* follow a partitional clustering, looking for coarse regions of energy flow and checking afterwards, if the cone's axis coincides with the sum of the four momenta of the particles therein.
The significant algorithms for the thesis at hand are the k_t [39] and the anti-k_t algorithm [40]. They iteratively cluster particles according to their closeness in momentum and their spatial closeness ΔR_{ij} (eq. 10). The procedure for the k_t algorithm goes as follows:

1. Calculate the distance d_{ij} between all particles with the definition

$$d_{ij} = \min(p_{ti}^2, p_{tj}^2)\frac{\Delta R_{ij}^2}{R^2} . \tag{26}$$

2. Calculate the distance

$$d_{iB} = p_{ti}^2 . \tag{27}$$

3. Merge particles i and j with the smallest distance to a new *protojet*.
4. If d_{iB} is the smallest, call i a jet and remove it from the list.
5. Recalculate the distances of particles and protojets.

(For an inclusive approach repeat until there are no more particles and protojets.)

Following this scheme, the k_t algorithm summarises particles up to a certain threshold given by the *jet resolution parameter* R in eq. 26, starting with the softest particles. Changing the definitions to

$$d_{ij} = \min\left(\frac{1}{p_{ti}^2}, \frac{1}{p_{tj}^2}\right)\frac{\Delta R_{ij}^2}{R^2} , \tag{28}$$

$$d_{iB} = \frac{1}{p_{ti}^2} \tag{29}$$

one obtains the anti-k_t algorithm that begins clustering with a hard particle. In absence of a neighbouring hard particle within 2R, the anti-k_t will accumulate all particles within the radius R. It provides mostly conical jets with a jet area $A = \pi R^2$ (fig. 34).

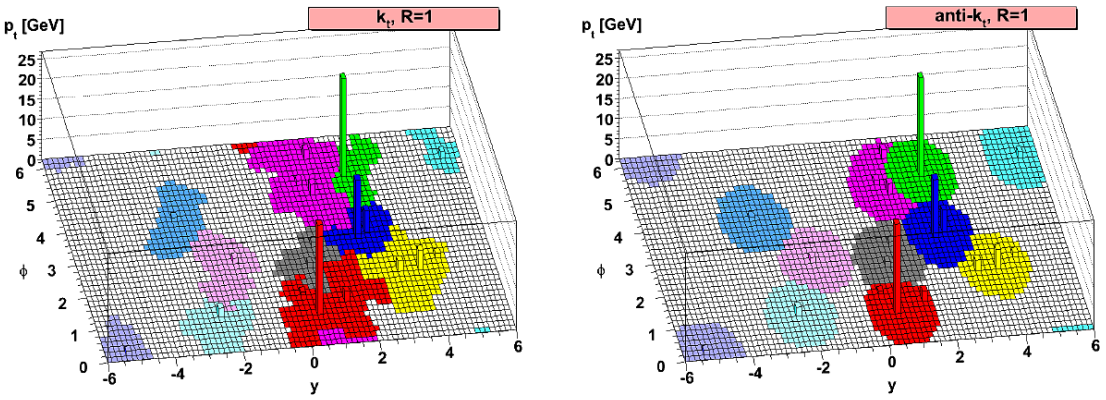

Figure 34: Jet shapes of k_t and anti-k_t algorithm in the φ-y-plane [40].

While the k_t algorithm is used to estimate an underlying event in a heavy-ion collision, the anti-k_t algorithm serves as a *signal* jet finder. The advantages of the latter are the regular jet boundaries and its resilience to *backreaction* (fig. 35).

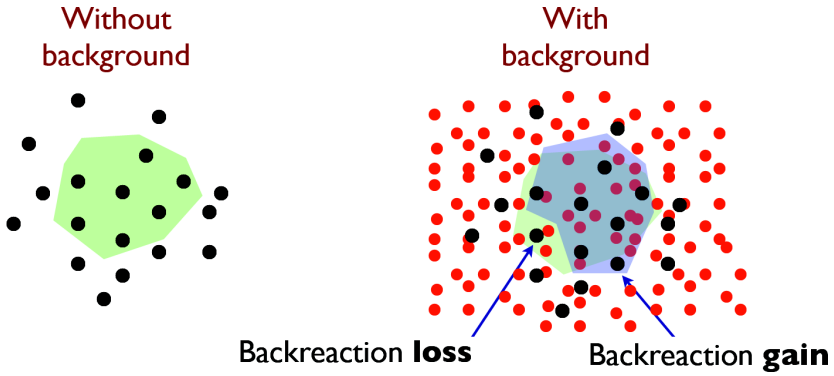

Figure 35: Backreaction: the underlying event can change the jet shape [41].

In order to calculate the jet rate with pQCD, the jet algorithm has to be insensitive against soft emissions and collinear splitting. The algorithm is called IRC safe (*Infrared Collinear* safe), when these effects do not change the jet or respectively, an associated observable O:

$$O(X; p_1, ..., p_n, p_{n+1} \to 0) = O(X; p_1, ..., p_n) \quad (30)$$

$$O(X; p_1, ..., p_n \| p_{n+1}) = O(X; p_1, ..., p_n + p_{n+1}) \quad (31)$$

In addition to its significance for calculations, IRC safety may also be seen beneficial for the jet finding itself. As heavy-ion collisions add lots of soft particles and detectors may split or merge collinear particles, an IRC safe algorithm can compensate for an incomplete consideration of these effects. IRC safety is guaranteed by the k_t/anti-k_t algorithm, as by any hierarchical clustering algorithm.

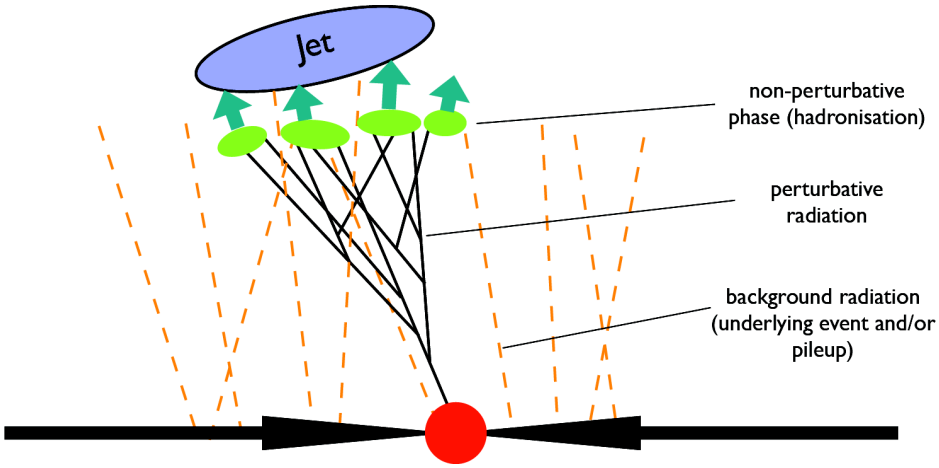

Figure 36: R-dependent momentum contributions to a jet [41].

After establishing the anti-k_t algorithm as the jet finder of choice, let us now consider the choice of the free parameter R. Broadening through hadronization and perturbative radiation motivates a large R, which however makes the jet susceptible to radiation of the underlying event (fig. 36).
Analytical estimates of the contributions are given by [42]; their R-dependence (in the small R limit) goes as follows:

$$\text{hadronization: } \Delta p_T \propto -\frac{(C_F, C_A)}{R} \tag{32}$$

$$\text{perturbative radiation: } \Delta p_T \propto \frac{\alpha_s(C_F, C_A)}{\pi} p_T \ln R \tag{33}$$

$$\text{underlying event: } \Delta p_T \propto R^2 \tag{34}$$

Here, the color factors $C_F = 4/3$ and $C_A = 3$ give the relative probabilities of the processes $q \to gq$ and $g \to gg$.
The large disturbance from the underlying event in heavy-ion collisions typically imposes a limit on the jet resolution parameter viable for jet analysis.

2.4.3 *Recent Results on Jet Quenching and Jet Structure*

The medium-induced energy loss of hard partons or *jet quenching* can be quantified by the *nuclear modification factor* R_{AA}, comparing jet or leading hadron spectra of heavy-ion collisions and p-p collisions:

$$R_{AA} = \frac{1}{N_{coll}} \frac{dN_{AA}/dp_T}{dN_{pp}/dp_T} \tag{35}$$

The heavy-ion yield is rescaled by N_{coll} from Glauber calculations, since the number of hard processes scales with the number of collisions. The ratio R_{AA} therefore is unity in absence of medium or initial state effects. Fig. 37 shows the nuclear modification factor for Pb-Pb collisions at $\sqrt{s_{NN}} = 2.76\,\text{TeV}$. These results confirm the phenomenon of jet quenching and, consistent with energy loss models, a rise of the nuclear modification factor with increasing parton energy E, i.e. a decreasing fractional energy loss $\Delta E/E$.

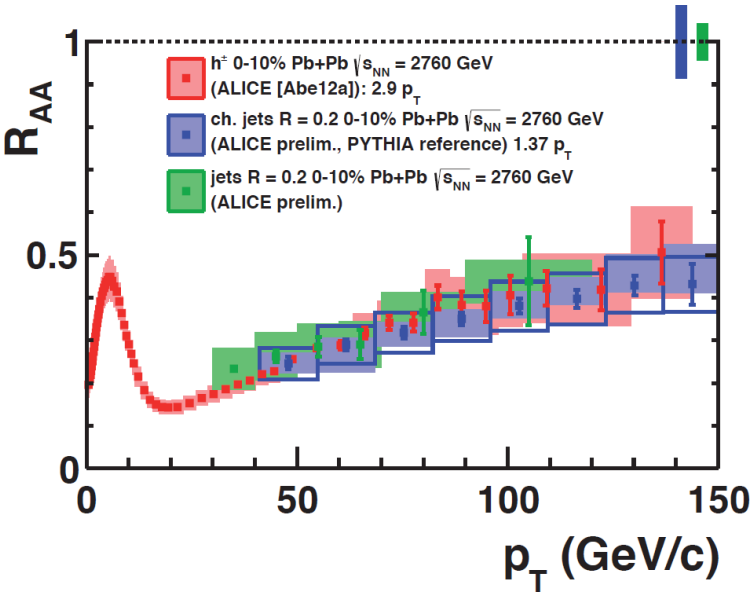

Figure 37: R_{AA} from central Pb-Pb collisions at $\sqrt{s_{NN}} = 2.76\,\text{TeV}$: charged hadrons, charged jets and full jets; the p_T for charged hadrons and charged jets is rescaled to full jets from a factor determined in p-p collisions [13]. PYTHIA (see section 3.4) simulations have been used as a p-p reference.

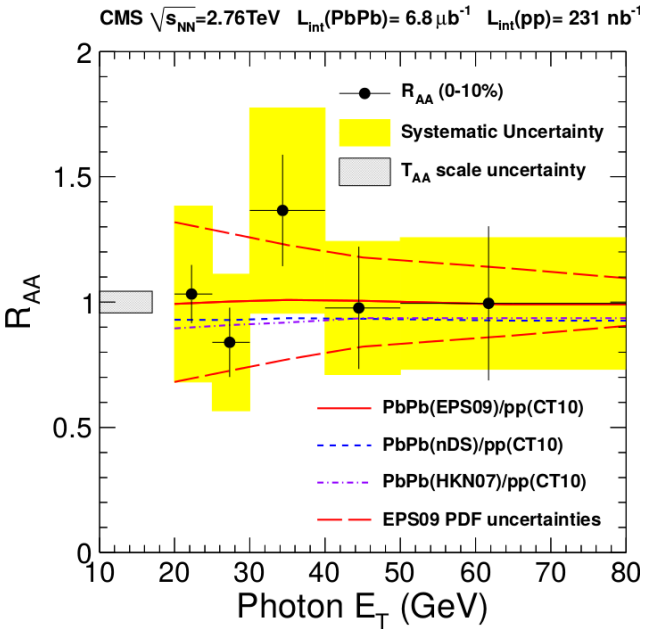

Figure 38: R_{AA} of photons; theoretical predictions for various nuclear PDFs (curves) [43].

Prompt photons with $R_{AA} \approx 1$ show that the N_{coll} scaling holds (fig. 38). For further validation of the parton energy loss suggested by the R_{AA}, one investigates p-Pb collisions to assess the influence of initial state effects. From what can be seen from the corresponding R_{pA}, there are no strong nuclear effects visible for charged jets in the momentum range between 20 and 100 GeV/c [44]. However, evidence for hydrodynamic flow [45] and an enhanced R_{pA} for tracks with $p_T > 30\,\text{GeV}/c$ [46] motivate further investigations for this supposed *cold nuclear matter* reference.

A second quantity to expose medium-induced modifications is the ratio R_{CP} comparing the yield of central and peripheral heavy-ion collisions:

$$R_{CP} = \frac{N_{\text{coll-peripheral}}}{N_{\text{coll-central}}} \frac{dN_{\text{central}}/dp_T}{dN_{\text{peripheral}}/dp_T} \tag{36}$$

Fig. 39 shows the suppression of jets comparing central and peripheral collisions. This observation indicates that the full jet energy is not recovered within the jet radius due to medium-enhanced out-of-cone radiation of gluons. One should be aware that for the low end of the momentum range it is debatable to what degree jet suppression can be attributed to an enhanced energy loss or the incomplete reconstruction of jets.

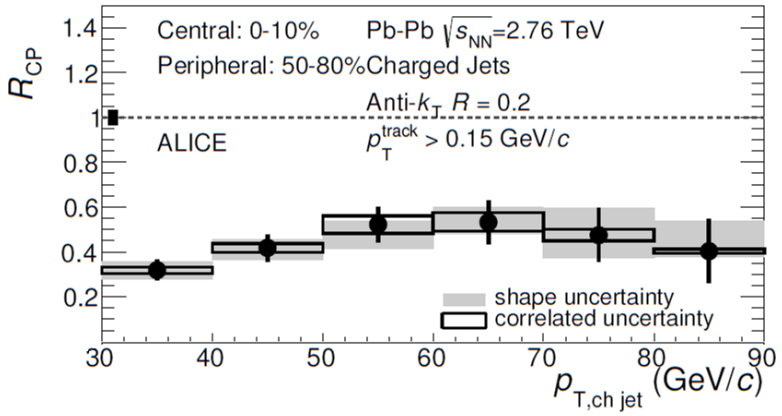

Figure 39: R_{CP} for jets from Pb-Pb collisions at $\sqrt{s_{NN}} = 2.76$ TeV [47].

While jet quenching as seen from the nuclear modification factors is a well established fact, it is not clear to what extent the jet fragmentation pattern – the jet substructure – is affected by the modified parton energy loss in a medium. Comparing the jet yield for different jet resolution parameters $R = 0.2$ and $R = 0.3$, there is no visible difference between a medium fragmentation and vacuum fragmentation (fig. 40).

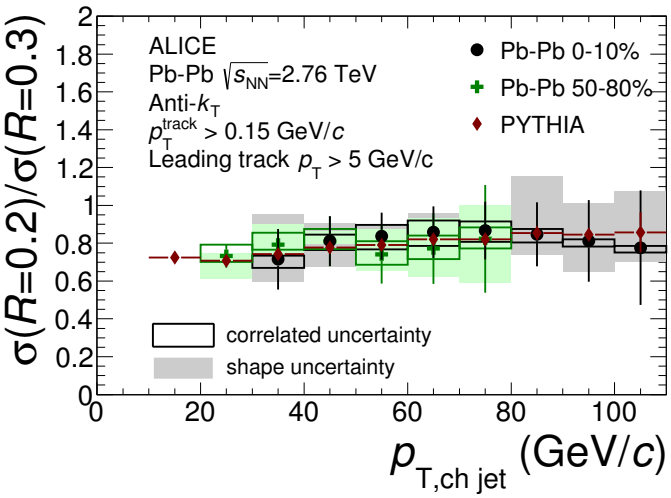

Figure 40: Ratio of charged jet spectra with radius parameter R = 0.2 and 0.3 with leading charged particle requirement of $p_T > 5$ GeV/c: PYTHIA simulations and peripheral Pb-Pb events yield a vacuum-like fragmentation pattern, central Pb-Pb events represent the medium modified case. [48].

Evidence for a modified jet structure has been found in [49] concerning highly energetic jets with $p_T > 100\,\mathrm{GeV}/c$. The employed observable is the differential jet shape $\rho(r)$ that describes the radial distribution of the transverse momentum within the jet cone in terms of rings (annuli) around the jet axis:

$$\rho(r) = \frac{1}{\delta r}\frac{1}{N_{jet}}\sum_{jets}\frac{1}{p_T^{jet}}\sum_{tracks\,\in\,[r_a,\,r_b[} p_T^{track} \tag{37}$$

Each annulus is defined with an inner radius $r_a = r - \delta r/2$ and an outer radius $r_b = r + \delta r/2$. The measured differential jet shape for Pb-Pb collisions at $\sqrt{s_{NN}} = 2.76\,\mathrm{TeV}$ is depicted in fig. 40 for different collision centralities using $\delta r = 0.05$ annuli and $R = 0.3$ jets. The comparison with a p-p reference points out the radial jet structure modification in a medium.
Peripheral collisions provide a jet shape similar to the p-p reference, confirming the vacuum-like fragmentation pattern expected from peripheral events. Going to higher centralities the region of $0.1 < r < 0.2$ becomes depleted, while the momentum density increases for $r > 0.2$. This shows that nuclear modifications can be found within the jet cone.

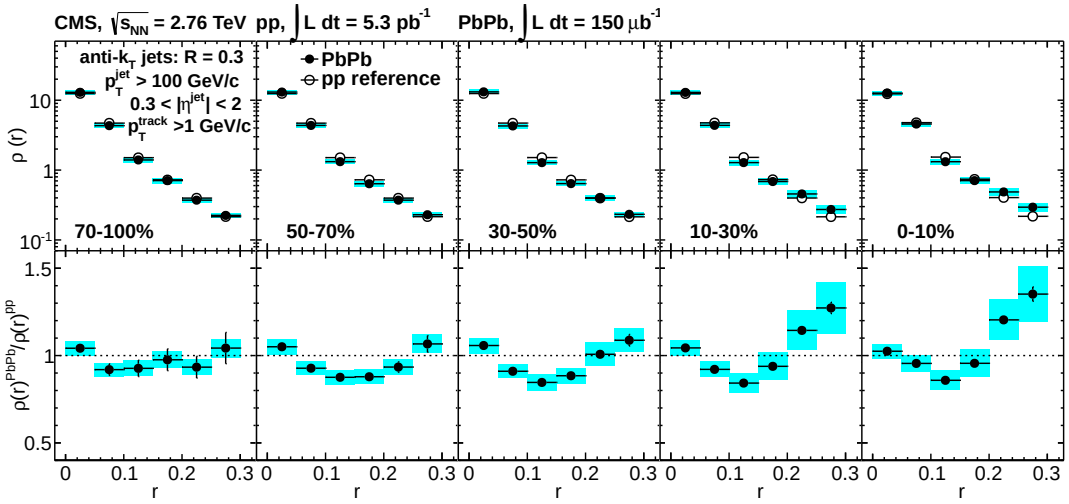

Figure 41: Top row: differential jet shapes of Pb-Pb (filled circles) and p-p (open circles). Bottom row: jet shape nuclear modification factor ρ_{PbPb}/ρ_{pp}. Each spectrum is normalised to an integral of unity. [49]

3

EXPERIMENTAL BASICS

Ideas about the QGP have been discussed since the emergence of QCD, yet the observation of it has become possible not before particle accelerators were able to deliver the required energy. Heavy-ion collisions have been introduced in the 1970s with projectile energies of about 1 GeV per nucleon [50]. The studies on condensed nuclear matter advanced with experiments at the AGS at Brookhaven National Laboratory (BNL) ($\sqrt{s_{NN}} \approx 5\,\text{GeV}$) and the SPS at CERN ($\sqrt{s_{NN}} \approx 20\,\text{GeV}$). With the Relativistic Heavy Ion Collider (RHIC) the collision energy could be increased to $\sqrt{s_{NN}} = 200\,\text{GeV}$ providing pronounced evidence of a QGP [51] [52] [23] [53].
The successor of the RHIC is the Large Hadron Collider (LHC) with the first heavy-ion collisions in 2010 at $\sqrt{s_{NN}} = 2.76\,\text{TeV}$. The ALICE detector experiment focuses on the observation of heavy-ion collisions and the QGP. Accelerator and detector are introduced briefly in the next sections. Closer attention will be payed to the particle tracking due to its relevance for jet analysis. The last section covers some computational methods of the analysis.

3.1 THE LARGE HADRON COLLIDER

The LHC is a particle accelerator at CERN (European Organization for Nuclear Research) near Geneva, Switzerland. With a circumference of 27 km this synchrotron is designed for a nucleon-nucleon centre-of-mass energy of 14 TeV for colliding protons (p-p) and 5.5 TeV for lead ions (Pb-Pb). So far the achieved energies were 8 TeV (p-p), 2.76 TeV (Pb-Pb) and 5.02 TeV for collisions between protons and lead ions (p-Pb).

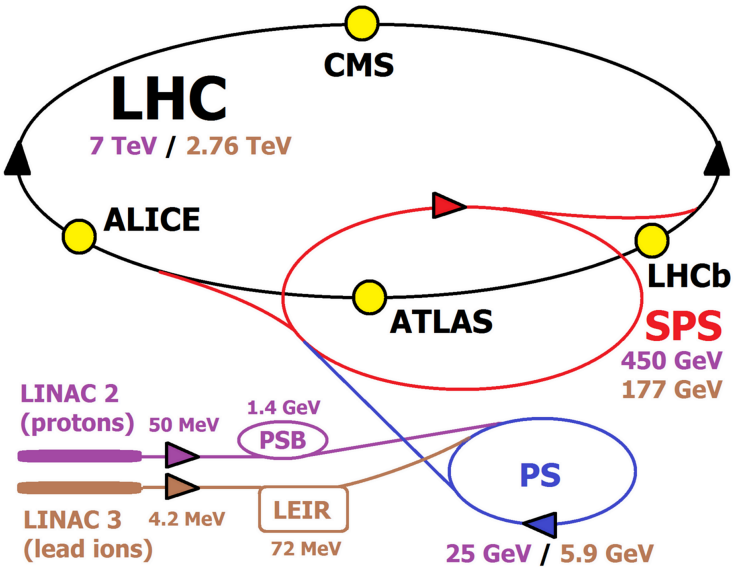

Figure 42: Schematic sketch of the LHC and preaccelerators with corresponding particle energies per nucleon.

Integrated in existing CERN structures, the LHC has been built in the tunnel of the Large Electron Positron Collider (LEP, 1989-2000) and makes use of the accelerator infrastructure of older experiments like the Super Proton Synchrotron (SPS) that emerged from the Sp$\bar{p}$S accelerator renowned for the production of W- and Z-Bosons from proton-antiproton collisions which have been observed by the experiments UA1 and UA2 in 1983.
Forced on their orbits by superconducting magnets, protons or lead ions in the LHC are revolving against each other in two separate beam pipes. A collision can be induced at four interaction points where the following detector experiments are located:

- ATLAS (A Toroidal LHC ApparatuS)

  ATLAS is a general purpose detector testing the Standard Model, respectively looking for physics beyond the Standard Model like Supersymmetric extensions [22]. One major goal has already been achieved in 2012 with the discovery of the Standard Model Higgs Boson [54].

- CMS (Compact Muon Solenoid)

  CMS is yet another general purpose detector [55]. Constructed in a different way from ATLAS, but inspecting similar topics, CMS is considered to verify ATLAS's findings and vice versa. That way, CMS was not less involved in the finding of the Higgs Boson [56].

- ALICE (A Large Ion Collider Experiment)

  In contrast to CMS and ATLAS, the abilities of the ALICE detector are aimed at heavy ion collisions involving a high particle multiplicity [57]. The focus lies mainly on the study of the quark-gluon plasma.

- LHCb (Large Hadron Collider beauty)

  Challenging the Standard Model, LHCb is designed for the precise measurements of the CP violation and rare decay modes of b-hadrons [58].

- TOTEM (Total Elastic and Diffractive Cross Section Measurement)

  This experiment studies the total proton-proton cross section and diffractive processes. In addition, TOTEM monitors the luminosity of the LHC [59].

- LHCf (Large Hadron Collider forward)

  The smallest experiment LHCf observes collisions from a zero degree angle for data that can be linked to the study of cosmic rays interacting with the atmosphere [60].

Further information on the LHC can be found in the LHC Guide [61] or more comprehensively, in the Technical Design Report [62].

3.2 THE ALICE EXPERIMENT

The ALICE detector allows the observation of heavy-ion collisions yielding more than a thousand charged particles per event and per unit of pseudorapidity [32] – in contrast to the yield of comparable proton-proton collisions that is more than two orders of magnitude smaller [63].

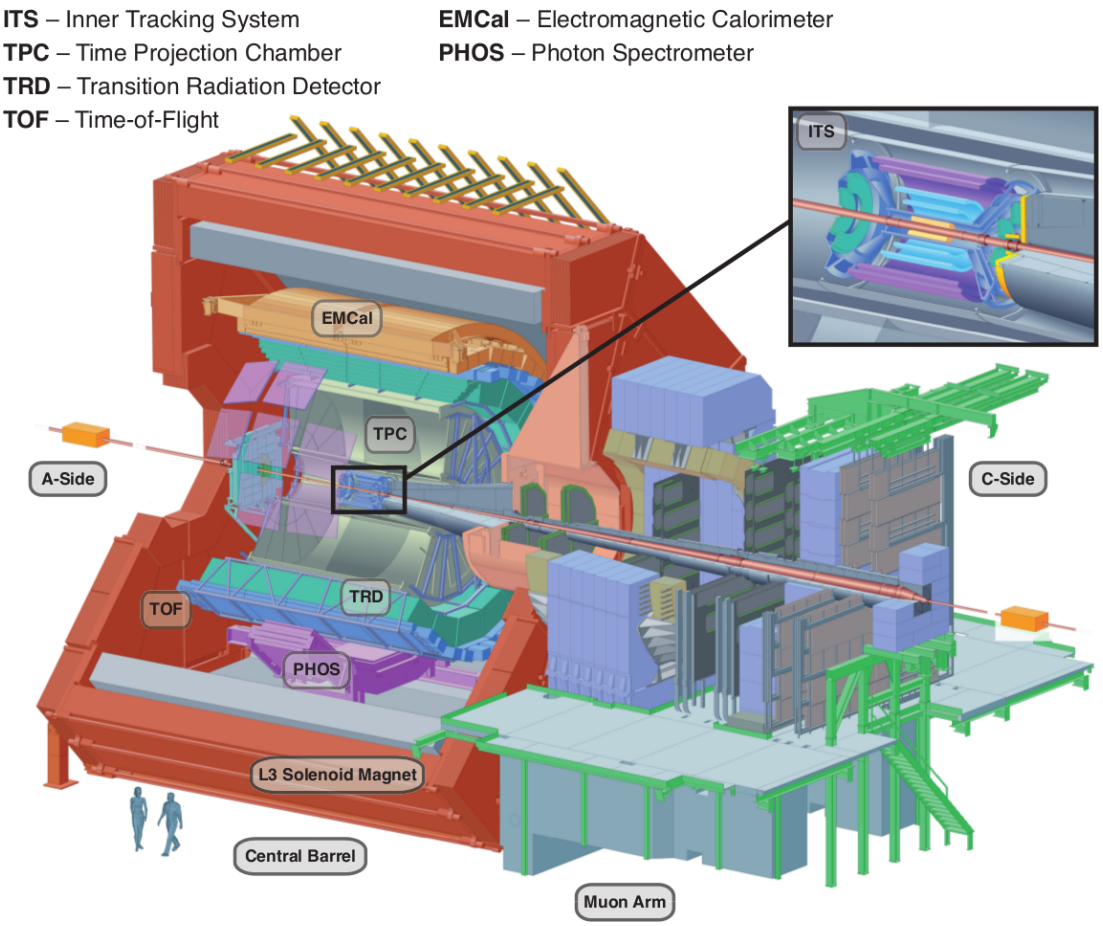

Figure 43: Cross-sectional view of the ALICE Detector [13].

The experiment consists of a set of detectors which are arranged around the interaction point (fig. 43). Along with a forward branch for measuring muons, there is the central part surrounded by a large magnet (delivering a homogeneous field of 0.5 T) that has already been used in the L3 experiment of the LEP. The 18 detectors serve different purposes including triggering, tracking, particle identification (PID) and estimation of the collision centrality. Below, some features of the ALICE detector will be presented in a brief fashion. For an exhaustive overview see [57].

Centrality Measurement

Measuring forward energy deposition with the VZERO detector [64] and the Zero Degree Calorimeter (ZDC) [65] provides an estimation of the collision centrality (cf. section 2.3).

Detection of Neutral Particles

Neutral particles like π^0 or η can be observed in the Photon Spectrometer (PHOS) and the Electromagnetic Calorimeter (EMCal) through their decay photons. While the PHOS focusses on the examination of direct photons, the EMCal covers a wider acceptance that allows neutral components to be included in the analysis of *full* jets (as opposed to *charged* jets).

Muon Spectrometer

The muon spectrometer placed in the forward arm of ALICE covers a pseudorapidity of $-4.0 < \eta < -2.5$. It provides the observation of the $\mu^+\mu^-$ spectrum and thus the measurement of vector-meson type quarkonia, from the ϕ meson up to Υ type resonances. Further studies cover the production of open charm and open beauty via semi-leptonic decay channels.

Particle Identification (PID)

Charged particles that traverse the Inner Tracking System (ITS) or the Time Projection Chamber (TPC) will undergo a specific energy loss per unit of length as a function of their charge, their rest mass and their momentum (Bethe-Bloch formula). In order to reveal a particle's identity, its momentum is measured via the bending in the magnet field and the energy deposit in the detector via the signal amplitude. This PID via Bethe-Bloch parametrization (fig. 44) is complemented by the Time-Of-Flight detector (TOF) which extends the momentum range and resolves ambiguities of the dE/dx PID, i.e. in regions where Bethe-Bloch curves of different particle species cross. Further PID is carried out by the HMPID for high momentum particle separation and the Transition Radiation Detector (TRD) providing electron identification.
A compact overview of PID at ALICE is given in [66].

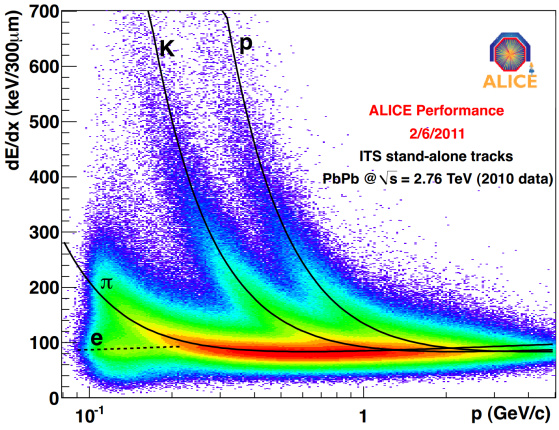

Figure 44: Example of a Bethe-Bloch parametrization using the ITS [67].

Triggering

ALICE has to cope with a rapid succession of collisions. A differentiated trigger setup has been invented in order to filter events of interest, to suit physics requirements, to account for the different busy times of the detectors and to follow Data Acquisition (DAQ) restrictions [68][69]. There are two fast trigger levels L0 and L1 whose signals reach the detectors in 1.2 μs and 7.7 μs, respectively. L0 considers basic properties like the particle multiplicity, while L1 includes more complex conditions like the appearance of jets. Limited by the TPC drift time of 94 μs the *slow* trigger L2 determines if an event is to be taken. After a complete read-out the event can still be discarded, based on the online analysis of the *High Level Trigger* (HLT).

3.3 CHARGED PARTICLE TRACKING

The particle tracking translates the space-points of detector hits into a track with the information about the primary vertex, the emission angle and the curvature (which gives the particle's momentum and the sign of its electric charge). The significant detectors for this task are the ITS and the TPC.

Inner Tracking System (ITS)

The ITS [70] consists of six cylindrical layers of silicon detectors (see upper right of fig. 43). The two innermost layers are Silicon Pixel Detectors (SPD) used to determine primary and secondary vertices. A further set of 2+2 layers of Silicon Drift Detectors (SDD) and Silicon Strip Detectors (SSD) can be used for PID via specific energy loss. Delivering space points of particle hits, all six layers contribute to particle tracking.

Time Projection Chamber (TPC)

The TPC [71] is the drift chamber surrounding the ITS. It is by far the largest detector of ALICE. Traversing particles leave charges behind that are pulled towards the readout end-plates by an electrostatic field. In this way, the charges draw a two-dimensional projection of particle tracks which is complemented by the drift time providing the third dimension. Together with the ITS the TPC covers the full azimuthal angle over a pseudorapidity of $|\eta| < 0.9$ (approx. $-44°$ to $44°$).

Track Reconstruction

Starting with the primary vertex and two clusters from the outer region of the TPC, where detector occupation is lower, a track fit is performed that successively moves inward, updated with every cluster that is picked up within a proximity cut. As the same TPC cluster can stem from more than one track, clusters shared between reconstructed tracks are allowed within certain limits. A track can be reconstructed with a maximum of 159 TPC clusters. Tracks with less than 20 clusters or less than 50 % of the expected clusters are rejected. After the track fit reaches the inner layer of the ITS, the procedure is repeated starting with the ITS. With the found clusters the final fit going inwards again is performed. Several refinements take place during the course of track reconstruction, e.g. the matching with hits in the TRD or the consideration of dead zones. For a detailed description of the tracking procedure, see [72].
The momentum resolution decreases for higher track momentum, as the curvature becomes less pronounced. There is a momentum resolution $\sigma(p_T)/p_T$ of about 1 % for 1 GeV/c, rising constantly to approx. 20 % at 100 GeV/c. At the expense of momentum resolution, tracks of worse quality can be included in order to compose a track distribution uniform in φ (*hybrid tracks*).
The share of reconstructed tracks against all physical tracks – the *tracking efficiency* – is about 85 % for p-p collisions. There is usually a minimum p_T requirement of 150 MeV/c – low energetic tracks are usually not reconstructed due to their limited trajectories. Pb-Pb collisions come with a tracking efficiency that is approx. 4 percentage points worse due to more restrictive tracking requirements used for higher multiplicities.

3.4 COMPUTATIONAL TOOLS

ROOT & AliRoot

The data analysis framework is given by the software ROOT [73]. Written in C++, it incorporates an object oriented approach providing modules for data acquisition, simulations, analysis, data visualization etc. As an extension to ROOT, AliRoot includes additional functionalities for the analysis of events from the ALICE experiment [74].

Monte Carlo Generators

To a large extent, particle collisions can be simulated with Monte Carlo (MC) simulations. This allows to study particle collisions with well defined properties and to compare expectations with experimental data.
For this work the Pythia6 event generator has been used [75] to simulate the hard QCD processes that give rise to jets. The generator covers all key points of a typical high-energy event, including the initial scattering based on an initial parton distribution function, the evolution of a final-state shower and a model for the hadronization that accounts for the QCD confinement mechanism. The set of parameters for Pythia in the context of this thesis is given by the Perugia-2011 tune [76] that is constrained by experimental data including early LHC results.
In order to simulate the influence of a medium on an outgoing parton, QPythia [77] has been employed. It modifies the vacuum-like final-state radiation of Pythia by adding a term to the parton splitting function that accounts for medium-induced gluon radiation.
After events have been generated on a *particle level*, the interaction of the particles with the ALICE detector can be modeled with GEANT3 [78]. This includes their propagation in the magnetic field, the interaction with the material, possible decays and electronic responses. Accordingly, the objects generated in this fashion are called *detector level tracks*. The appliance of a jet reconstruction algorithm may follow, yielding detector level jets.

4

UNFOLDING OF HEAVY-ION JET SPECTRA

Following a power law shape (eq. 15), the amount of jets produced in a collision depends heavily on their respective momentum. A presumably small uncertainty of the jet energy scale can lead to a large distortion of the original yield, compromising quantities like the nuclear modification factor (cf. 2.4.3) and therefore compromising the constraints on theoretical models.
Accounting for detector effects and the heavy-ion background, this study deals with the correction of jet spectra following the procedure of *unfolding*. The inspected events are Pb-Pb collisions that have been carried out in 2011 with $\sqrt{s_{NN}} = 2.76\,\text{TeV}$. The used data set is given in the appendix A via the respective run numbers.

4.1 BACKGROUND FLUCTUATIONS

Taking jets as an observable instead of single hadrons, one can again include energy that has been spread by fragmentation of the original parton. As a drawback one has to deal with the considerable influence of the underlying event.
For correction the first step is an event-wise determination of the mean background momentum density ρ. Clustering all tracks of an event with the k_t jet algorithm, one receives a set of jets i with transverse momentum $p_{T,i}$ and jet area A_i. The value of ρ can then be estimated with the median of $p_{T,i}/A_i$. Excluding the two leading tracks and using the median value, the influence of occasional hard tracks is reduced. For central Pb-Pb collisions at $\sqrt{s_{NN}} = 2.76\,\text{TeV}$ the mean background density ρ is about $140\,\text{GeV}/c$, which translates into the significant background contribution of $70\,\text{GeV}/c$ to an anti-k_t jet with resolution parameter $R = 0.4$.

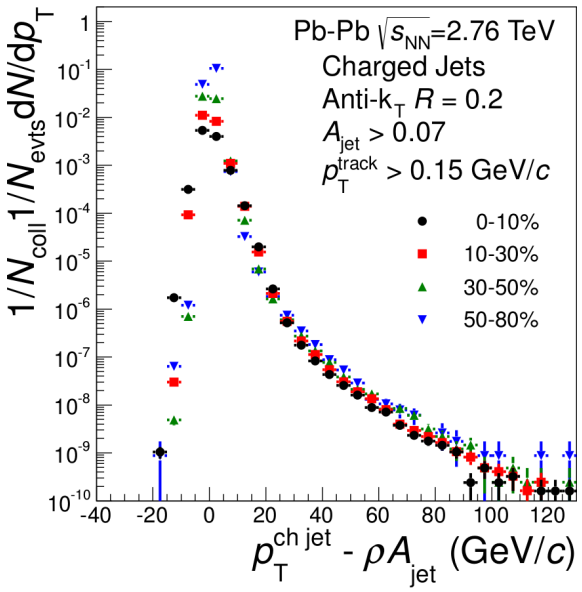

Figure 45: Charged jet spectrum for different centralities with the correction for mean background density [47].

Subtracting a mean background momentum ρA still leaves momentum fluctuations δp_T (fig. 45). Especially upward fluctuations cause a severe shift to the yield due to the steeply falling p_T spectrum. The sources of background fluctuations have been studied in [79].
The number of tracks N and their p_T in a jet fluctuate statistically. Therefore the resulting fluctuations δp_T of jets are of Poissonian nature and are correctly described by a Γ function [80]. The width of δp_T is given by

$$\sigma(\delta p_T) = \sqrt{N \cdot \langle p_T \rangle^2 + N \cdot \sigma^2(p_T)}\,, \tag{38}$$

where $\langle p_T \rangle$ is the mean and $\sigma(p_T)$ the variance of the single particle p_T spectrum. Subsuming tracks in cones randomly placed in (φ, η) one can expose the contributions of (non-)statistical contributions. Fig. 46 shows the δp_T found in these random cones (RC) for different scenarios.

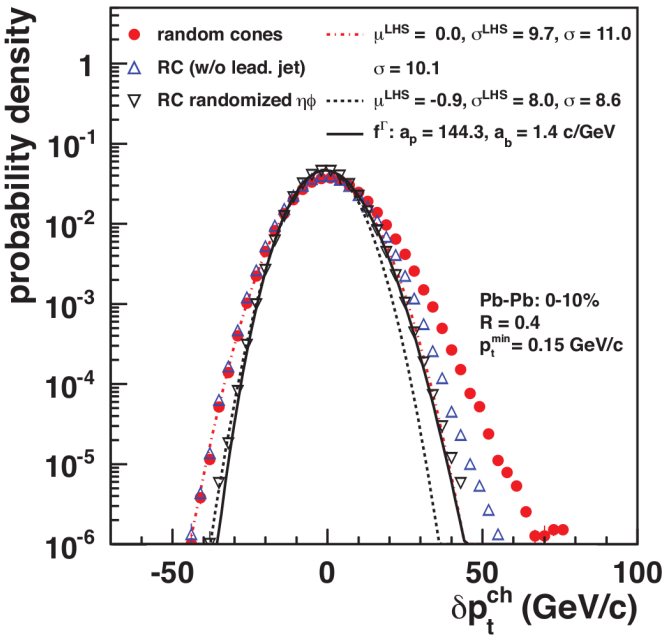

Figure 46: The δp_T found in random cones for three different approaches; dotted lines depict Gaussian fits to the left hand side [79].

Destroying all correlations, the randomization of tracks in (φ, η) gives a δp_T spectrum that is close to the Poissonian limit and can be described with the Γ function. Simultaneously, the visible right hand side deviation of a Gaussian Fit shows the asymmetric shape of the purely Poissonian form alone.
For cones that avoid overlap with the leading jet the region of positive δp_T is understandably less pronounced than for cones and tracks that have not been tampered with. However, non-Poissonian contributions remain, which are mainly attributed to the collective flow of the medium. Including a contribution σ_{CF} of the collective flow, the width $\sigma(\delta p_T)$ from eq. 38 can be modified accordingly:

$$\sigma(\delta p_T) = \sqrt{(N + \sigma^2_{CF}(N)) \cdot \langle p_T \rangle^2 + N \cdot \sigma^2(p_T)} \text{ with} \tag{39}$$

$$\sigma^2_{CF}(N) = 2N^2(v_2^2 + v_3^2) \tag{40}$$

The Fourier coefficient v_2 (v_3) accounts for the elliptic flow (triangular flow) caused by the initial asymmetric overlap of the nuclei (initial state fluctuations). Fig. 47 shows that collective flow can explain a large share of non-Poissonian fluctuations that do not stem from jets.

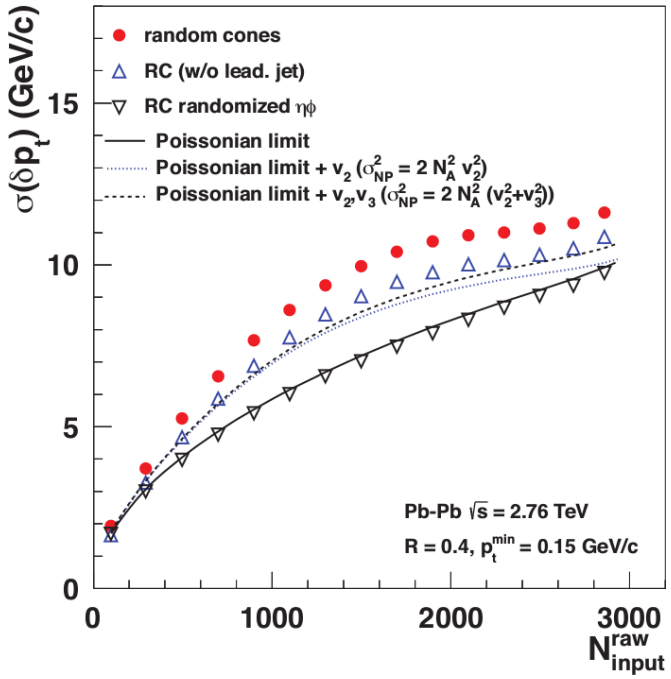

Figure 47: Background fluctuations found with track/jet embedding [79].

Fluctuations of an entirely different nature can arise from the interplay between the underlying event and the jet finder. One can embed different probes into the event for the jet algorithm to cluster, subtracting mean background and the probe afterwards:

$$\delta p_T = p_{T,Jet} - \rho A - p_{T,Probe} \tag{41}$$

In order to study two contrary cases of fragmentation pattern, the embedding of single high p_T tracks and the embedding of jets from p-p collisions have been examined (fig. 48).

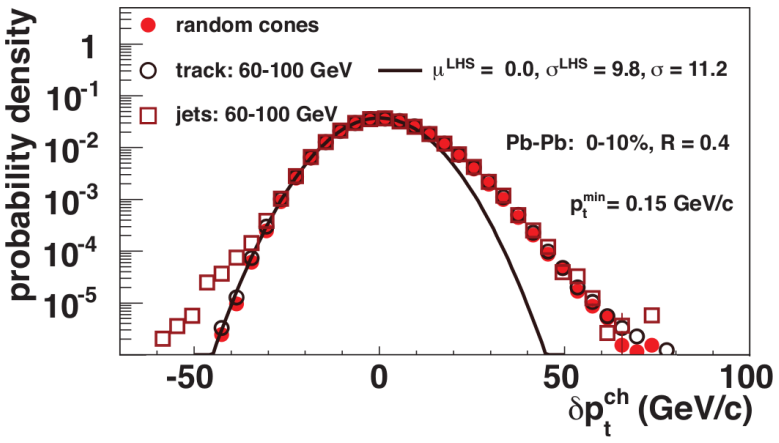

Figure 48: Background fluctuations for different probes (random cones, track embedding, jet embedding) [79].

The embedding of high p_T tracks gives fluctuations that resemble the result from random cones (fig. 48). The robust behaviour of the used anti-k_t jet finder is therefore confirmed for this case, except for a slight increase of $\sigma(\delta p_T)$ that can be attributed to the jet area resolution.
The embedding of p-p jets however reveals an undesirable behaviour within the heavy-ion environment. An embedded jet with a large area in combination with a neighbouring hard track of the event can lead the anti-k_t algorithm to have two split jets instead. The reduced area in which the transverse momentum is collected leads therefore to a reduced δp_T, which gives the left hand side enhancement in fig. 48.

4.2 DETECTOR RESPONSE

Fluctuations of the jet p_T can be caused by shortcomings of the detector. The finite momentum resolution leads to a smearing of the track p_T and consequently a smearing of the jet p_T. A second issue is the imperfect tracking efficiency. Particles that could not have been reconstructed as tracks do not appear in the jet, subsequently lowering the jet energy.

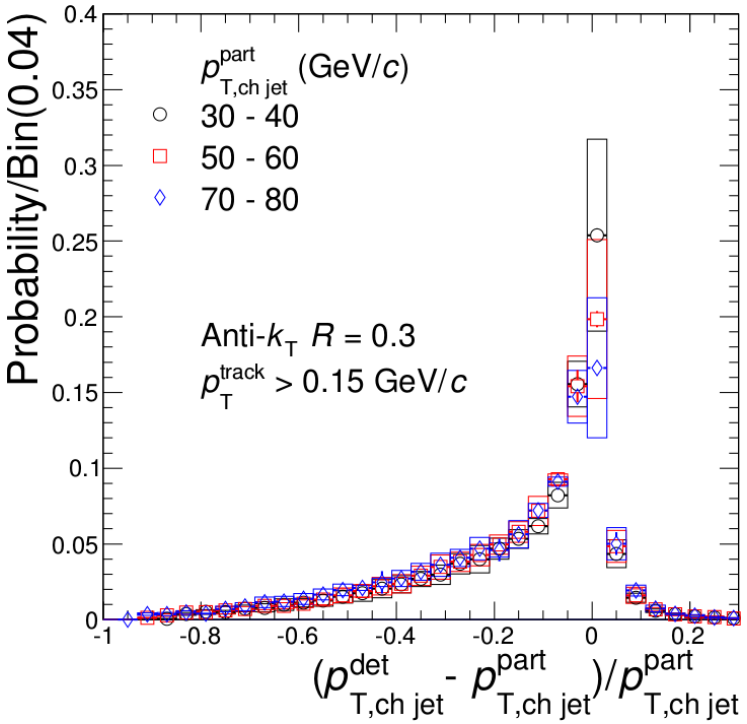

Figure 49: Simulated detector response for $R = 0.3$ anti-k_t jets for different p_T bins [48].

As provided by PYTHIA6 + GEANT3 simulations fig. 49 depicts the influence of momentum resolution and tracking efficiency, comparing the p_T of particle level jets and detector level jets. While a certain share of the jets is reconstructed correctly (within the given binning), a considerable amount is reconstructed at lower energy and only a minor part receives an upward shift.

4.3 UNFOLDING METHOD

While the detector effects and background fluctuations can be encoded in response matrices D and B, the binned yield of the measured and the corrected spectrum is represented by vectors m_i and u_k so that (using Einstein notation)

$$m_i = R_{ik} u_k = D_{ij} B_{jk} u_k \ . \tag{42}$$

Simply inverting the response matrix $R_{ik} = D_{ij} B_{jk}$ in order to obtain the corrected spectrum u_i leads to a highly fluctuating solution. However, it is possible to express the problem in terms of a χ^2-minimization. The χ^2 function compares the measured spectrum m_i (with uncertainty σ_i) and a *refolded* spectrum r_i:

$$\chi^2 = \sum_i \left(\frac{m_i - r_i}{\sigma_i} \right)^2 \text{ with} \tag{43}$$

$$r_i = R_{ik} u_k \tag{44}$$

Then, a term of regularization can simply be added:

$$\chi^2 = \sum_i \left(\frac{m_i - r_i}{\sigma_i} \right)^2 + \beta \sum_k \left(\frac{d^2 \ln u_k}{d \ln p_T^2} \right)^2 \tag{45}$$

The second term imposes the shape of a local power law onto the solution; the regularization parameter β allows to vary the strength of the regularization. It has to be ensured that the regularization does not dominate the procedure. Fig. 50 illustrates an unfolding where no regularization has been applied.
For the minimization process it is required that the bin number of the unfolded spectrum u_i – the number of free parameters – equals or is larger than the number of data points, i.e. the bins of the measured spectrum m_i.

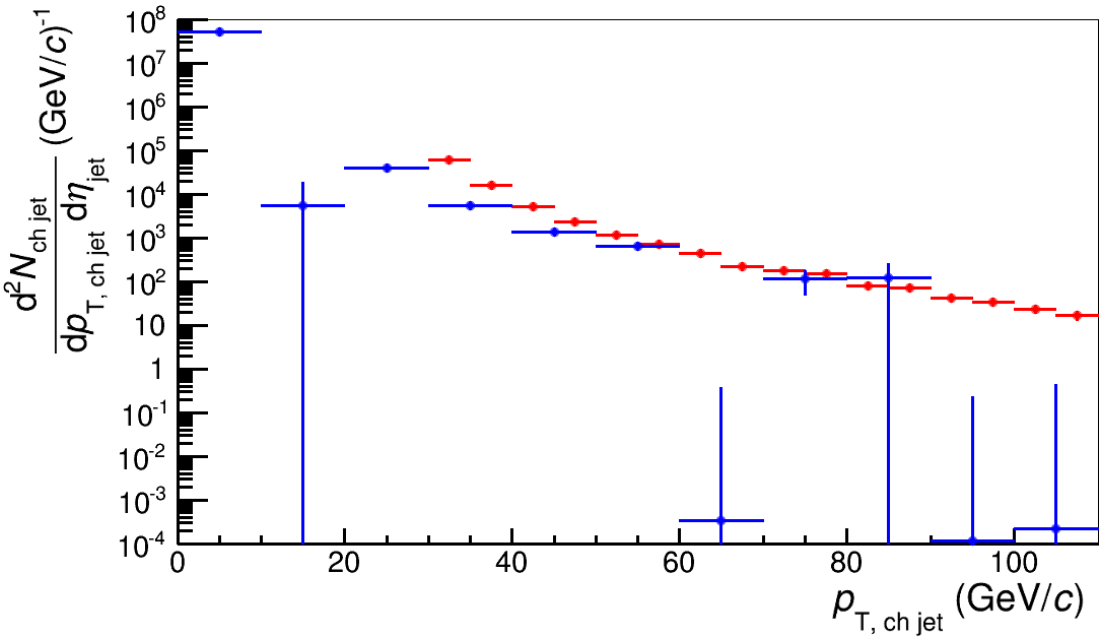

Figure 50: Measured (red) and unfolded jet spectrum (blue) without regularization.

Binning

The bin width of the measured and the refolded spectrum is 5 GeV/c. The bin width of the unfolded spectrum is twice as large with 10 GeV/c.

p_T Ranges

The chosen p_T-range for the measured spectrum is $30 - 110$ GeV/c. The maximum p_T was chosen according to the available statistics (there are approx. ten jets in the last bin for central events). Jets that arise mainly from background fluctuations are suppressed by the minimum p_T cut (one has $3\sigma(\delta p_T) \approx 30$ GeV/c for central events with $R = 0.4$). Combinatorial jets receive further rejection from a minimal jet area requirement.
The unfolded spectrum is given a range from $0 - 250$ GeV/c, which especially allows feed-in from the well populated region of low p_T. Although the feed-down from $p_T > 110$ GeV/c is expected to be almost negligible, the extra bins of the unfolded spectrum are necessary to meet the aforementioned minimum requirement of free parameters.

Response Matrices

The entries of the response matrices generated from PYTHIA and GEANT3 simulations have been merged to match the new binning (fig. 52). For the merging a *Tsallis* function has been used for the a proper reweighting. Provided by PYTHIA simulations it ensures a proper rebinning, as it accounts for the shape of the steeply falling jet spectrum. Without the reweighting the yield of a merged bin would incorrectly be dominated by the low p_T end of fine bins that are merged.
A closer look at the combined response matrix reveals that the content of bins can be shifted outside the reconstructed p_T range. This kinematic efficiency (fig. 51) is corrected for.

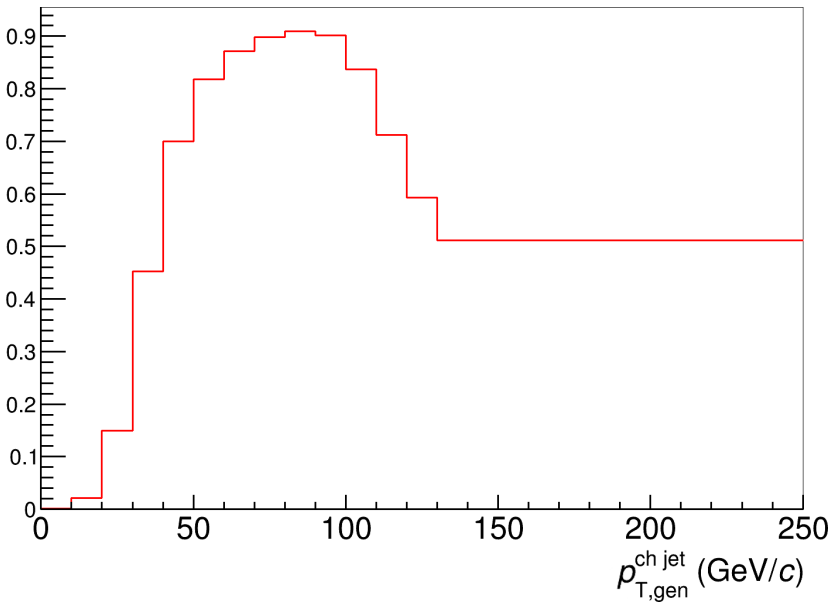

Figure 51: Kinematic efficiency of the combined response matrix for $R = 0.3$.

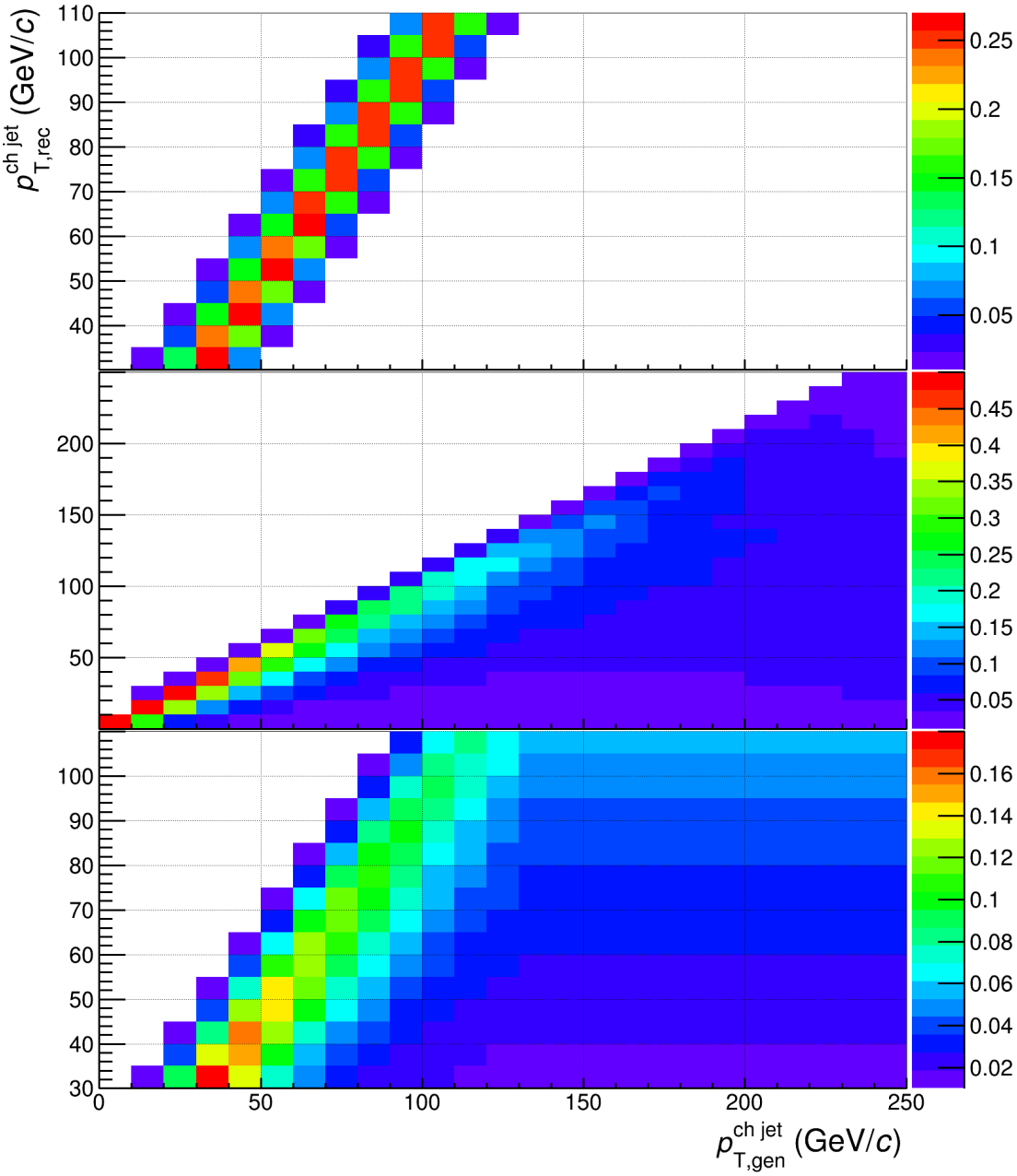

Figure 52: Response matrices for R = 0.3 for background fluctuations (top), detector effects (middle), both effects (bottom).

4.4 UNCERTAINTIES OF THE UNFOLDING PROCEDURE

In the following, parameters of the unfolding procedure are discussed and uncertainties evaluated.

4.4.1 *Regularization Strength*

The choice of the correct regularization strength β has been examined.
A first criterion is given by the Pearson coefficient matrix $P(i,j)$, which stems from the covariance matrix from the unfolding:

$$P(i,j) = \frac{\mathrm{cov}(i,j)}{\sigma_i \sigma_j} \tag{46}$$

These coefficients show correlations between bins i, j for values -1 (totally anti-correlated) over 0 (not correlated) to 1 (totally correlated).

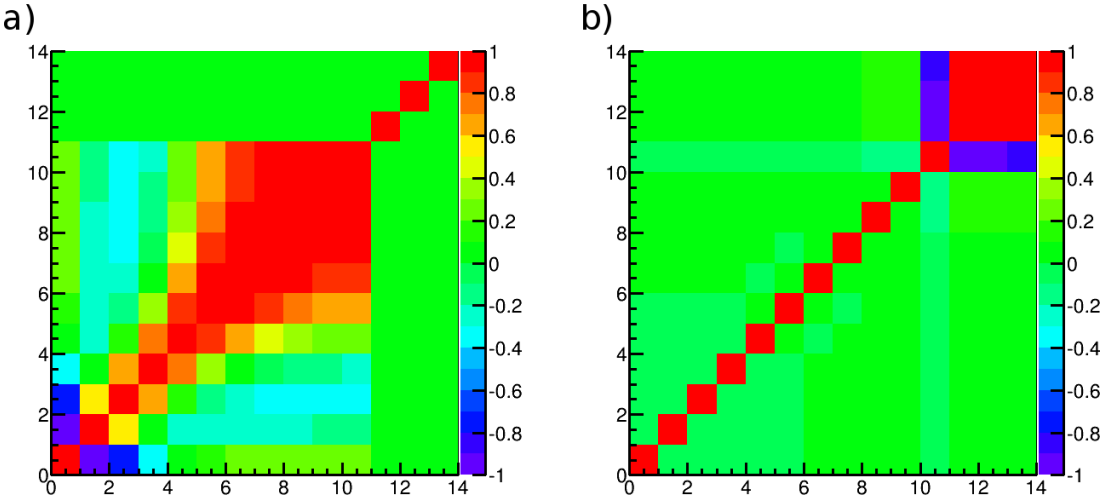

Figure 53: Pearson coefficient matrices for a) $\beta = 2.0$ and b) $\beta = 0.01$.

Choosing the regularization strength β too large, the Pearson matrix shows clear correlations between bins as shown in fig. 53 a). For a regularization too weak, the Pearson matrix can deliver larger off-diagonal elements, but above all, the yield of the unfolded spectrum starts to have obvious fluctuations. Matrices with visible correlations like fig. 53 b) will still be accepted, when correlated bins are limited to the regions of $p_T > 110\,\mathrm{GeV/c}$ and $p_T < 30\,\mathrm{GeV/c}$.
One can further refine the correct choice of β considering the quality of the fit. The χ^2 can be subdivided into its elements

$$\chi^2 = \chi^2(\mathrm{Fit}) + \chi^2(\beta) \tag{47}$$

Within the preliminary boundaries found above, $\chi^2(\beta)$ shows relative fluctuations of about 50 %. The value of $\chi^2(\mathrm{Fit})$ is always at least 20 times higher, which hints at a right choice of β. However, $\chi^2(\beta)$ stays fairly small even for clearly over-regularized cases. Anyway, a narrow interval of β can be found by improving $\chi^2(\mathrm{Fit})$ to the point, where the improvements of $\chi^2(\mathrm{Fit})$ and the fluctuations of $\chi^2(\beta)$ become comparable.
The systematic uncertainty of the unfolding procedure that arises from the remaining

freedom of β has been studied in the following for central events $(0-10\,\%)$ with $R = 0.3$.

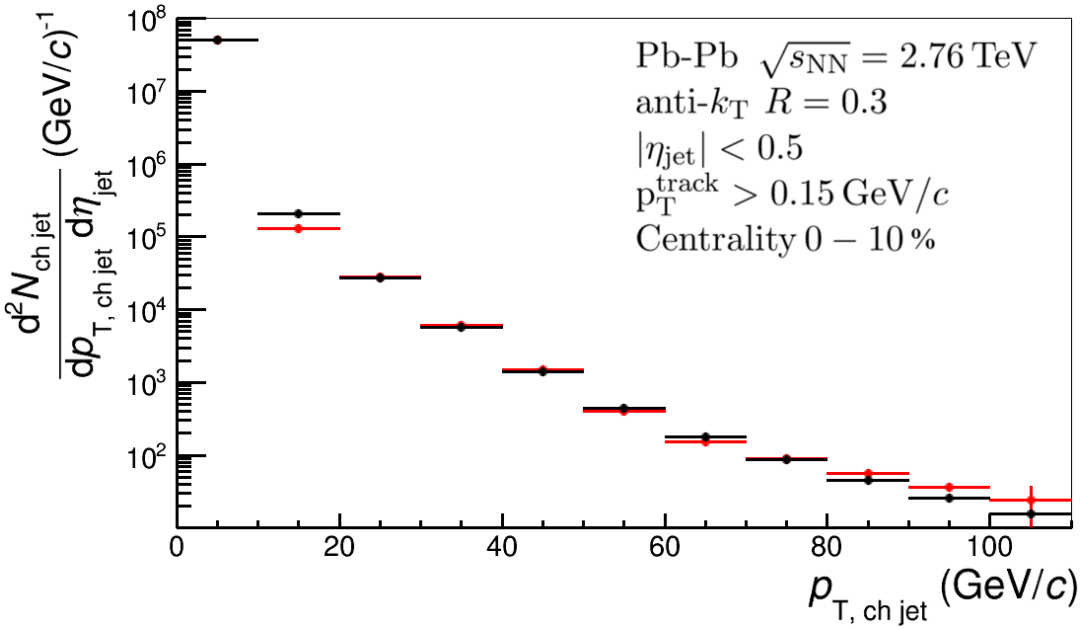

Figure 54: Unfolded spectra for $\beta = 0.0006$ (red) and $\beta = 0.01$ (black). Unfolding for intermediate β consistently yields values between the depicted spectra.

The aforementioned method gives an optimal $\beta \in [0.0006, 0.01]$. The unfolded spectrum for both limits is depicted in fig. 54. The unfolding is repeated for $n = 1000$ times with β linearly varied in the given range:

$$\beta(i) = 0.0006 + \left(\frac{0.01 - 0.0006}{1000}\right) i \tag{48}$$

The uncertainty of each bin u_j is then given by

$$\sigma_j = \sqrt{\frac{1}{n-1}\sum_{i=1}^{n}\left(\mu_j - u_j(i)\right)^2} \tag{49}$$

with the mean value μ_j of the bin j and $u_j(i)$ the value of bin j for the i-th pass. The relative uncertainties are given in table 1. The uncertainty on the right choice of β leads to relative uncertainties up to 12.5 %, most pronounced in the second bin and the last bins. Turning off the regularization for $p_T < 30\,\text{GeV}/c$ yields twice the uncertainty in the first and second bin; the uncertainty of the rest of the bins and the χ^2 of the fit change marginally.
Unfolding with the same method has been done for Pb-Pb data of 2010 [47], where severe fluctuations on the unfolded spectrum have been reported for $p_T < 40\,\text{Gev}/c$. These fluctuations have been observed in this work only in a few cases and for large β intervals that have not been optimized in the aforementioned way. This indicates that the extensive optimization of β can offer a more stable unfolding for a wider p_T range.

p_T (GeV/c)	σ_j/μ_j in %
$0-10$	0.5
$10-20$	12.4
$20-30$	0.5
$30-40$	2.9
$40-50$	0.7
$50-60$	3.2
$60-70$	3.4
$70-80$	0.9
$80-90$	5.4
$90-100$	9.1
$100-110$	12.5

Table 1: Regularization uncertainty.

4.4.2 *Prior*

For the presented unfolding the measured spectrum has been taken as the prior, i.e. the spectrum the χ^2 minimization starts with. Generally, the choice of the prior can affect the outcome of this process. The influence of the prior has been examined for an unfolding with $R = 0.3$ and a centrality $0-10\,\%$. It has been observed that an artificially smaller or larger prior (or even a constant prior) leads to a slightly different unfolded spectrum. The minimization process however appears to be robust for the various tested priors, since the resulting deviations are all within two certain limits u_i^{min} and u_i^{max}. The unlimited number of possible priors cannot be examined, so a uniform distribution between the two values is assumed, which yields the uncertainty

$$\sigma_i = \frac{\Delta_i}{\sqrt{12}}\,, \text{ where} \tag{50}$$

$$\Delta_i = u_i^{max} - u_i^{min}\,. \tag{51}$$

The relative systematic uncertainty that comes from the prior is given in table 2.

p_T (GeV/c)	σ_i/μ_i in %
$0-10$	0.1
$10-20$	0.2
$20-30$	0.2
$30-40$	0.2
$40-50$	0.7
$50-60$	0.8
$60-70$	0.9
$70-80$	3.7
$80-90$	7.4
$90-100$	11.7
$100-110$	15.8

Table 2: Prior uncertainty.

The choice of the prior has a clear p_T dependence. Up to $70\,\text{GeV/c}$ the relative uncertainty remains below $1\,\%$, still growing gradually. For $70-110\,\text{GeV/c}$ the value grows quickly up to $15.8\,\%$ for the last bin of the unfolded spectrum.

Although the choice of the prior already shows small influence for most of the p_T bins, it is debatable whether the estimate of the uncertainty prior is too conservative. Assuming that a prior already close to the solution always gives a better solution, it would be sufficient to vary the prior within limits. Then however, reasons for these limits and the mentioned assumption have to be given. Then again, one may even go a step further and have a simulated jet spectrum with a background/detector model in order to start even closer to the unfolded solution.

4.4.3 p_T *Range Measured Spectrum*

The systematic uncertainty from the p_T range of the measured spectrum has been studied by varying the minimum p_T from 25 Gev/c to 35 GeV/c, i.e. having one additional bin or removing one bin. Fig. 55 shows the relative change of the unfolded solution. As for the variation of the regularization parameter β the second bin is the most unstable. The other regions of p_T show stability within 2% for most bins when extending the measured spectrum to $25 - 110$ GeV/c. Shortening the measured range to $35 - 110$ GeV/c the unfolded solution gives more pronounced deviations up to 11%.

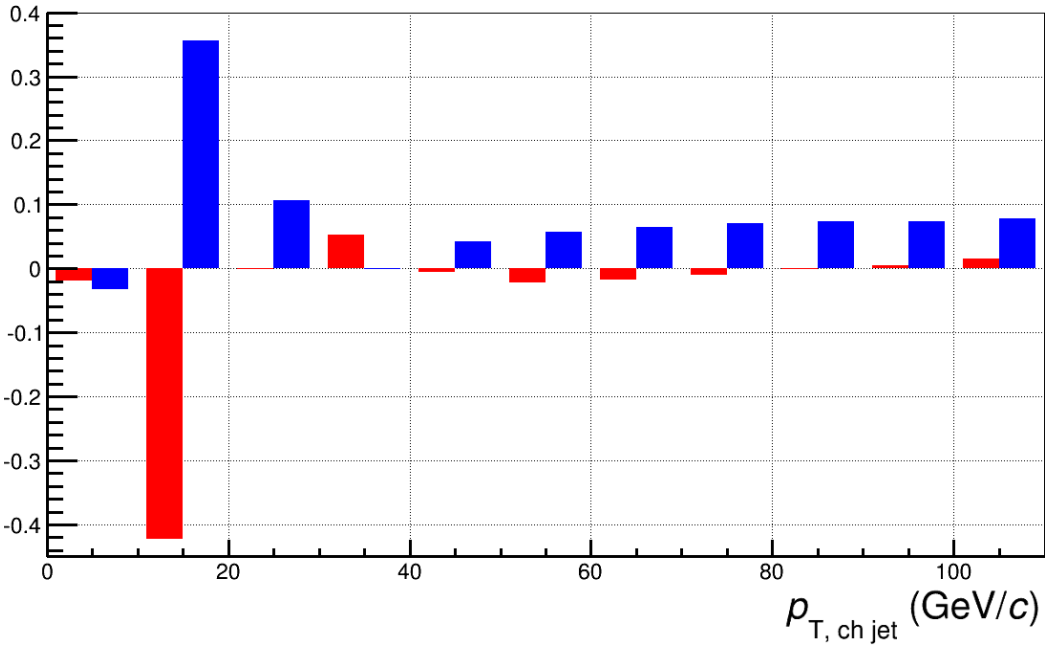

Figure 55: Uncertainty from variation of the measured spectrum: red (blue) bars give the relative change in unfolded yield for adding (omitting) one bin of the measured spectrum at the lower edge of the p_T range.

4.4.4 *Total Systematic Uncertainty of the Unfolding Procedure*

The used method of χ^2 unfolding cannot be applied in a strictly defined fashion. Parameters have to be tuned in a way that the minimization process does not break down and yields non-oscillating spectra. The remaining freedom for the choice of the parameters then gives rise to uncertainties of the unfolding procedure that have been studied for an anti-k_t jet spectrum of central events with $R = 0.3$.

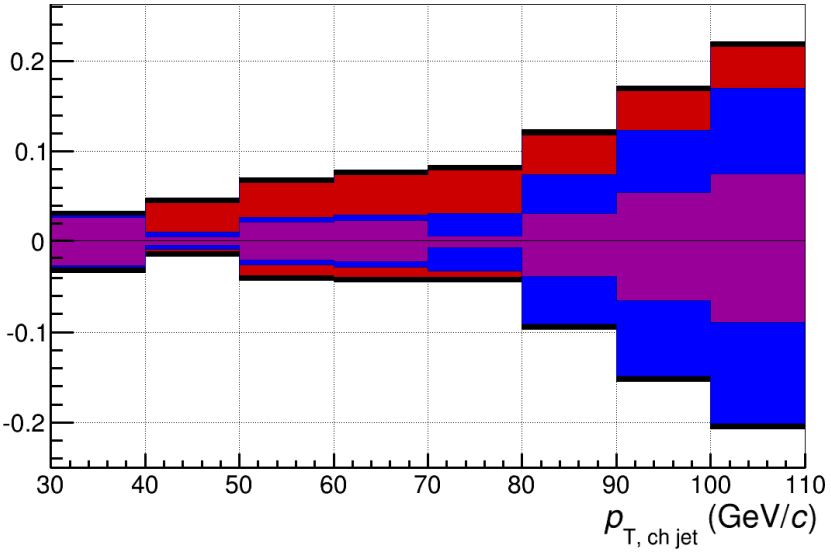

Figure 56: Total relative uncertainty from the unfolding procedure (black line). The colored boxes show not the actual values, but the linear proportions of the uncertainties relative to each other: regularization strength (violet), prior (blue), measured p_T range (red).

The total relative uncertainty (fig. 56) remains below 10% for the p_T region of $30 - 80\,\mathrm{GeV}/c$ and rises then to approx. 20% in the last p_T bin, where the uncertainty from the prior (blue) quickly increases. The uncertainty from the regularization (violet) shows a weaker p_T dependence, but rises as well for the last bins. No significant p_T dependence is seen for the uncertainty from varying the p_T range of the measured spectrum; it gives an overall upward shift to the total uncertainty.

4.5 COMPARISON TO RESULTS FROM 2010

Fig. 57 compares the corrected charged jet spectrum of the 2011 Pb-Pb data (this work) with results from 2010 Pb-Pb data [48]. The spectra (upper panel) have been normalised to the number of events and the number of collisions. Both results include statistical uncertainties and uncertainties from the unfolding procedure. The results from 2010 additionally consider uncertainties from the extraction of the response matrices. These correlated uncertainties however should cancel to a large degree concerning a ratio between the two results.

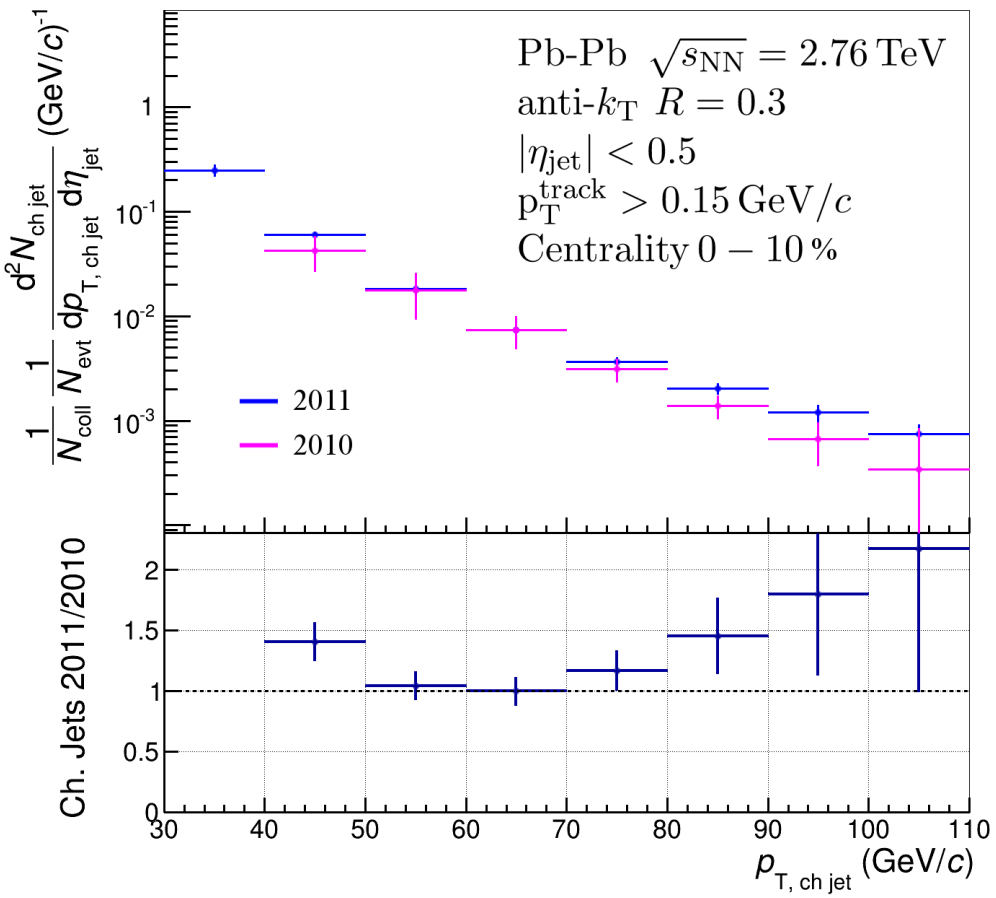

Figure 57: Corrected charged jet spectra (R = 0.3) from the 2010 (magenta) and 2011 (blue) run period of Pb-Pb collisions (upper panel); the ratio between the results visualises deviations (lower panel).

The ratio of the yields (lower panel) suggests a discrepancy. The points are not evenly distributed around unity, but form a convex shape that indicates a systematic difference between the two results from 2011 and 2010. To some degree this behaviour can be understood from the unfolding procedure: variation of unfolding parameters usually shows an anti-correlated relation between intermediate p_T bins and bins near the minimum/maximum p_T. Thus leads a larger regularization to a smoother shape of the ratio, yet a constant deviation from unity remains visible in every case.
In order to give a more quantitative account of the deviation, three simple functions have been fitted to the ratio; the results can be taken from table 3. Despite the visibly rising trend for higher p_T a constant factor 1.14 ± 0.07 gives a reasonable description of the deviation – which seems comprehensible considering the larger uncertainties at higher p_T.

fit function	χ^2/NDF	p − value
$f(x) = 1$	12.35/7	5 − 10 %
$f(x) = 1.14(7)$	7.78/6	25 − 30 %
$f(x) = 0.0003(50)p_T + 1.12(36)$	7.77/5	15 − 20 %

Table 3: Functions describing the ratio from the lower panel of fig. 57.

4.6 R_{AA} OF CHARGED AND FULL JETS

After the correction of the jet yield it is now justified to construct the nuclear modification factor R_{AA} (eq. 35). There is no experimental reference of p-p collisions for charged jets at $\sqrt{s_{NN}} = 2.76\,\text{TeV}$, so a PYTHIA reference has been used [81].

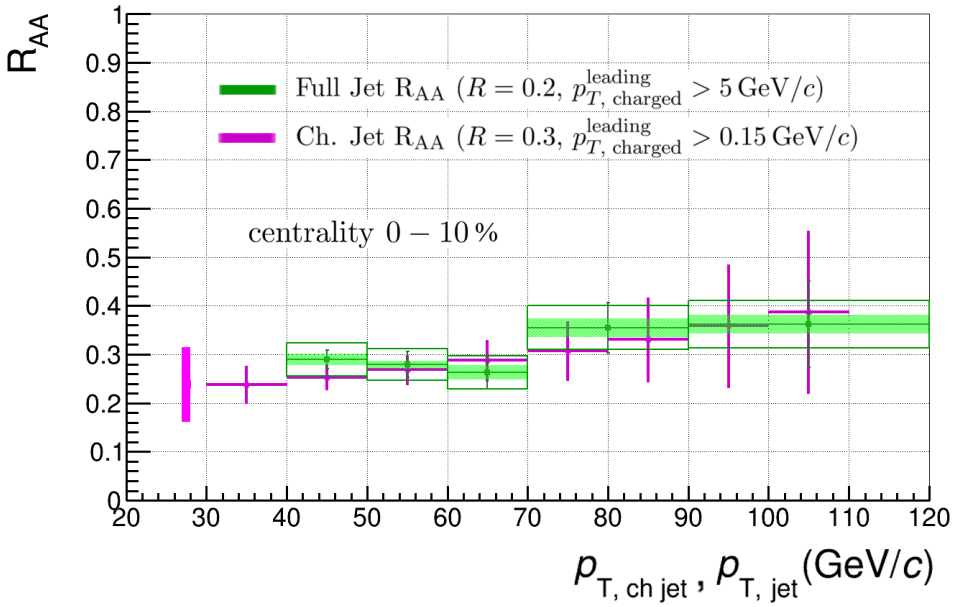

Figure 58: Nuclear modification factor in central Pb-Pb collisions at $\sqrt{s_{NN}} = 2.76\,\text{TeV}$. Magenta: charged jet R_{AA} (this work), error bars include the statistical uncertainty and the total systematic uncertainty from the unfolding, the bar on the left shows for the first bin the additional uncertainty from the PYTHIA reference (30 %) and the N_{coll} scaling (11 %); Green: full jet R_{AA} [82], error bars show statistical, hollow boxes show correlated, filled boxes show shape uncertainties.

The R_{AA} is shown in fig. 58 together with current results from full jet measurements [82] that employ a similar data set from 2011 Pb-Pb collisions. It is important to note that both results can only be compared with three caveats:

- The full jet measurement alone uses a leading track requirement of 5 GeV/c, which can lower the yield for lower jet energies ($p_T \lesssim 50\,\text{GeV/c}$). This however affects Pb-Pb and p-p jet yields almost equally, so that the impact on the R_{AA} should be insignificant.
- The full jet measurement reports an R_{AA} with a jet resolution parameter $R = 0.2$ instead of $R = 0.3$. A larger jet recovers more energy for the same energy of the original parton.
- The R_{AA} from charged jets lacks the inclusion of neutral particles, so that the jet energy is lower for the same energy of the original parton.

Considering the two latter caveats, the power law-like shape of the jet yield allows to adjust the p_T scale of the charged $R = 0.3$ jet R_{AA} with a simple factor given by PYTHIA simulations. It can be determined through the transformation of the p_T scale

that matches a R = 0.3 charged jet yield to a R = 0.2 full jet yield.[1] The rescaled R_{AA} is shown in fig. 59.

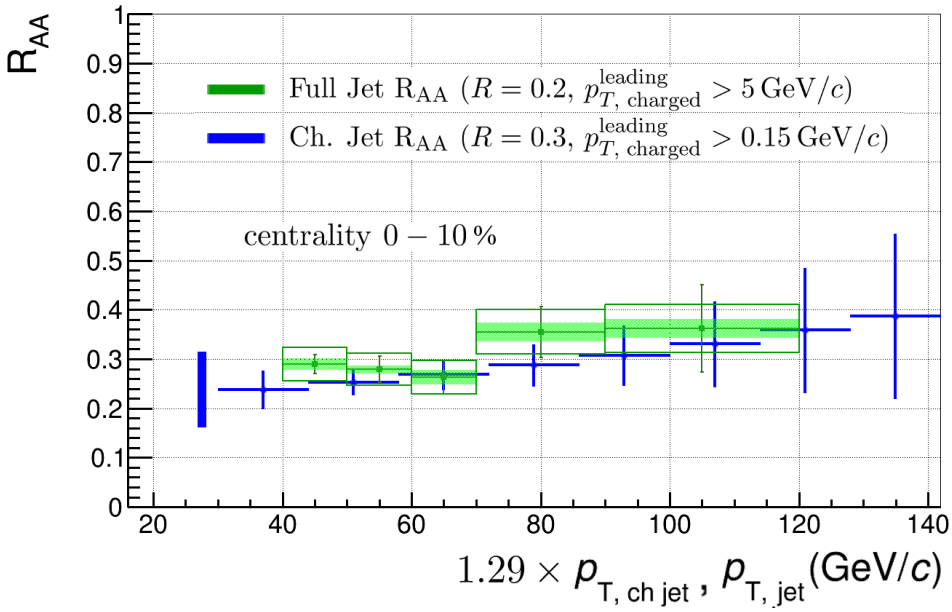

Figure 59: Nuclear modification factor in central Pb-Pb collisions at $\sqrt{s_{NN}} = 2.76$ TeV. Blue: rescaled charged jet R_{AA} (this work); Green: full jet R_{AA} [82]; uncertainties as in fig. 58.

The nuclear modification factors found from different jet definitions are in visible concordance. Moreover, the charged jet R_{AA} consistently reproduces the rise of the R_{AA} for higher jet energies, which agrees with the assumption of a decreasing fractional energy loss of harder partons in the medium. For any model comparison however one should be aware of the large uncertainties for large jet energies, and especially of the general uncertainty from the charged p-p reference that is provided by PYTHIA simulations rather than by experimental observation. Going beyond the scope of the ALICE collaboration, it can be noted that both results agree with recent full jet measurements from the ATLAS collaboration [83].

1 The assumption that a simple p_T rescaling from PYTHIA simulations can account for the energy shift from charged to full jets is easily accepted for the vacuum and the medium case. However, two minor caveats concerning the jet resolution parameter have tacitly been overlooked: 1) A larger energy of the original parton implies a more collimated fragmentation, so the change from R = 0.2 to R = 0.3 is not precisely given by a simple p_T rescaling. 2) Medium fragmentation is most presumably different from vacuum fragmentation. Nevertheless, the consequence of going from R = 0.2 to R = 0.3 is roughly the same for the vacuum and the medium as shown in section 2.4.3, fig. 40.

4.7 SUMMARY AND OUTLOOK

In this chapter the correction of a heavy-ion charged jet spectrum for detector effects and background fluctuations has been presented. Systematic uncertainties that stem from the unfolding procedure have been evaluated. The correction for background fluctuations and detector effects results in a flatter spectrum, lowering the yield by almost an order of magnitude for a p_T of $30-40\,\mathrm{GeV}/c$. The difference vanishes steadily for growing p_T and at $90-110\,\mathrm{GeV}/c$ the yield of the unfolded and the measured spectrum are comparable.
The reported results are based on charged jet yields from the 2011 Pb-Pb run at ALICE. A comparison to similar results from the 2010 Pb-Pb run [48] suggests a visible deviation, that has been parametrised and is at least partially covered by the uncertainties. The rather systematic impression of the deviation can to a large degree be attributed to the shape uncertainty of the unfolding procedure.
The influence of the medium, namely the jet quenching, has been quantified in the form of the nuclear modification factor R_{AA}. The results agree with recent full jet measurements from the ALICE collaboration [82] and similar measurements from the ATLAS collaboration [83].

In the following an outlook shall be given for further studies on the unfolding of jet spectra. Some elements of the unfolding procedure itself can be studied in more detail:

- Uncertainties that do not arise from the unfolding method itself remain unexplored, for instance the uncertainty of the tracking efficiency/detector resolution or the background fluctuations, i.e. uncertainties of the response matrices.
- If permitted by statistics, the unfolding can be carried out with a finer (or a variable) binning of the measured spectrum.
- There are alternative methods that the χ^2 unfolding can be compared with (e.g. Bayesian unfolding [84], Single Value Decomposition [85]).
- The unfolding procedure can be validated with a toy model of a jet spectrum.

The unfolding has been carried out with a minimum bias jet sample (except for the focus on central events and the standard minimum p_T requirement of $150\,\mathrm{MeV}/c$ for tracks). However, there are certain cuts that would allow to cope with the significant heavy-ion background, which would especially allow to study the jet spectrum at a lower transverse momentum:

- A smaller jet resolution parameter ($R = 0.2$ or even $R = 0.1$) can be considered. As the affliction by the background is proportional to the jet area, this would significantly decrease its influence. A smaller jet radius however undermines the very feature of a jet, the recovery of fragmented parton energy.
- The requirement of a minimum p_T of the leading particle in a jet decreases the amount of combinatorial jets that mainly stem from soft particles. This however introduces a bias on the fragmentation, which has to be weighed against the benefit of a reduced background influence. The same applies for a possible minimum track p_T requirement.

- Cuts on leading *subjets* can be considered, since they introduce a smaller fragmentation bias than leading hadron cuts. Subjets constitute a fairly unexplored observable. They are going to be subject to the next chapter of this thesis.

5

SUBJETS IN CHARGED JETS

Since the first collisions in 2010, jets became a well established observable in the heavy-ion environment of Pb-Pb collisions at $\sqrt{s_{NN}} = 2.76\,\text{TeV}$. The influence of the underlying event has been assessed for charged particles [79] (see also 4.1). Baseline measurements of the p-p jet cross-section have been carried out for full jets at $\sqrt{s_{NN}} = 2.76\,\text{TeV}$ [86] and for charged jets at $\sqrt{s_{NN}} = 7\,\text{TeV}$ [87]. The suppression of charged jets at $\sqrt{s_{NN}} = 2.76\,\text{TeV}$ has been evaluated in this work, section 4.6, and in [48]; full jet suppression has been reported in [82]. Further ongoing efforts include jet studies about p-Pb collisions at $\sqrt{s_{NN}} = 5.02\,\text{TeV}$, hadron-jet correlations and about the jet production with identified particles.

Probing the QGP, the jet observable has taken over the role of the leading hadron. The jet includes the energy lost by the fragmentation of a hard parton and is therefore closer to the original parton energy. Little does it matter for a jet how the final state of the parton shower is arranged – it is almost insensitive to the soft and thus poorly controlled effects of soft splitting and hadronization. At the same time, a (IRC safe) jet is an observable that is well understood and can be reproduced in theoretical calculations.

The same argumentation shall now be applied considering an investigation of the jet substructure. Small jets, i.e. *subjets*, should be considered to resolve more differential properties of the large, regular jet[1]. So far only the tracks of regular jets have been used to probe the fragmentation pattern (e.g. in fig. 60 or in section 2.4.3: fig. 41).

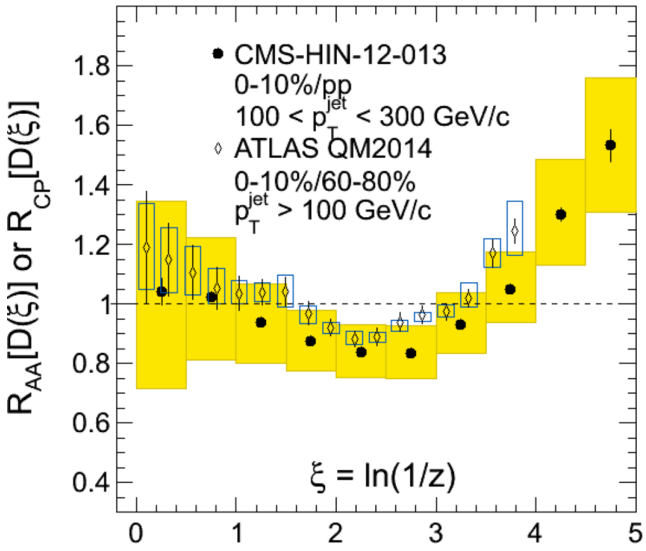

Figure 60: Fragmentation function $\xi = \ln(1/z)$ with $z = p_T^{track}/p_T^{jet}$. The R_{AA} from measurements of the CMS collaboration together with the R_{CP} from the ATLAS collaboration consistently report a depletion of jet constituents at intermediate p_T and an enhancement of low p_T constituents in Pb-Pb collisions at $\sqrt{s_{NN}} = 2.76\,\text{TeV}$. ATLAS in addition reports a slight enhancement of high p_T constituents [88].

1 In the following, *jets* will always refer to the large regular jets; subjets will always be denoted as such.

In this chapter properties of this so far unconventional observable shall be studied by way of simulation. Going from hard scatterings in p-p collisions over medium-modified jets to a toy model of the heavy-ion background and detector effects it will be shown how subjets behave in different scenarios. The underlying objective in this work is to test the general feasibility of subjet studies and to provide an analysis setup for further efforts.
There is little prior knowledge about subjets and their behaviour in a heavy-ion environment. Therefore the focus will lie on the most energetic subjet, the leading subjet, as the main observable of interest, since it is an observable that should be relatively robust against background affliction.

5.1 SUBJET PROPERTIES IN PYTHIA EVENTS

In the following subjets will be examined in charged jet populations from simulated hard scatterings. At this stage no medium effects are considered. The aim is to study basic properties of subjets with different subjet parameters in PYTHIA6 events, i.e. for the case of leading order hard scattering and vacuum fragmentation.
The anti-k_t jet algorithm is used throughout the analysis to reconstruct jets from the generated charged tracks with a jet resolution parameter $R = 0.4$. Considering the acceptance of the TPC and the ITS these tracks are generated within full azimuth and within a pseudorapidity of $|\eta| < 0.9$. Jet reconstruction is accordingly restricted to $|\eta| < 0.5$. The standard p_T track cut of 150 MeV/c is applied. According to the typical region of transverse momentum observed by ALICE, jets have been studied within a range of $30\,\mathrm{GeV/c} < p_T^{\mathrm{Jet}} < 70\,\mathrm{GeV/c}$.
Subjets are reconstructed with the k_t or the anti-k_t jet finder from tracks of a jet, so that they are always restricted to the boundaries of the jet. To test the sensitivity to the fragmentation pattern the subjet resolution parameter will be varied around $R = 0.1$. Motivated by the 1/R-dependence of momentum dispersion by hadronization (see eq. 34), small subjets should already tend to recover most of the energy distributed in the non-pertubative phase of the parton fragmentation.
A collision energy of $\sqrt{s_{NN}} = 2.76\,\mathrm{TeV}$ has been chosen. It has not been varied, since subjets will be examined within p_T bins of the jet: The fragmentation of a given parton is universal for a given medium or vacuum and does not depend on the collision energy. The collision energy determines the shape of the hard parton spectrum, which can hence marginally change the fragmentation function observed in jet p_T bins of finite size. The subordinate role of the collision energy in this context is demonstrated in fig. 80, 81 and 82 which can be found in the Appendix B.
The error bars in all figures give the statistical uncertainty. They are sometimes visible due to restricted computation time, but do not affect any of the conclusions.

Fragmentation Function for (Sub-)Leading Subjets

The fragmentation function $F(z)$ gives the probability to find a track (e.g. in fig. 60) or a subjet with a certain momentum fraction z of the jet's momentum with

$$z = \frac{\vec{p} \cdot \vec{p}^{Jet}}{|\vec{p}^{Jet}|^2} . \tag{52}$$

Here, the momentum vector $\vec{p}$ of a track/subjet is projected onto the axis of the jet, so that z is refered to as the longitudinal momentum fraction of a jet. The required vector components (p_x, p_y, p_z) in Cartesian coordinates are determined by the transverse momentum p_T and the coordinates φ, η:

$$p_x = p_T \cos(\varphi) \tag{53}$$
$$p_y = p_T \sin(\varphi) \tag{54}$$
$$p_z = p_T \sinh(\eta) \tag{55}$$

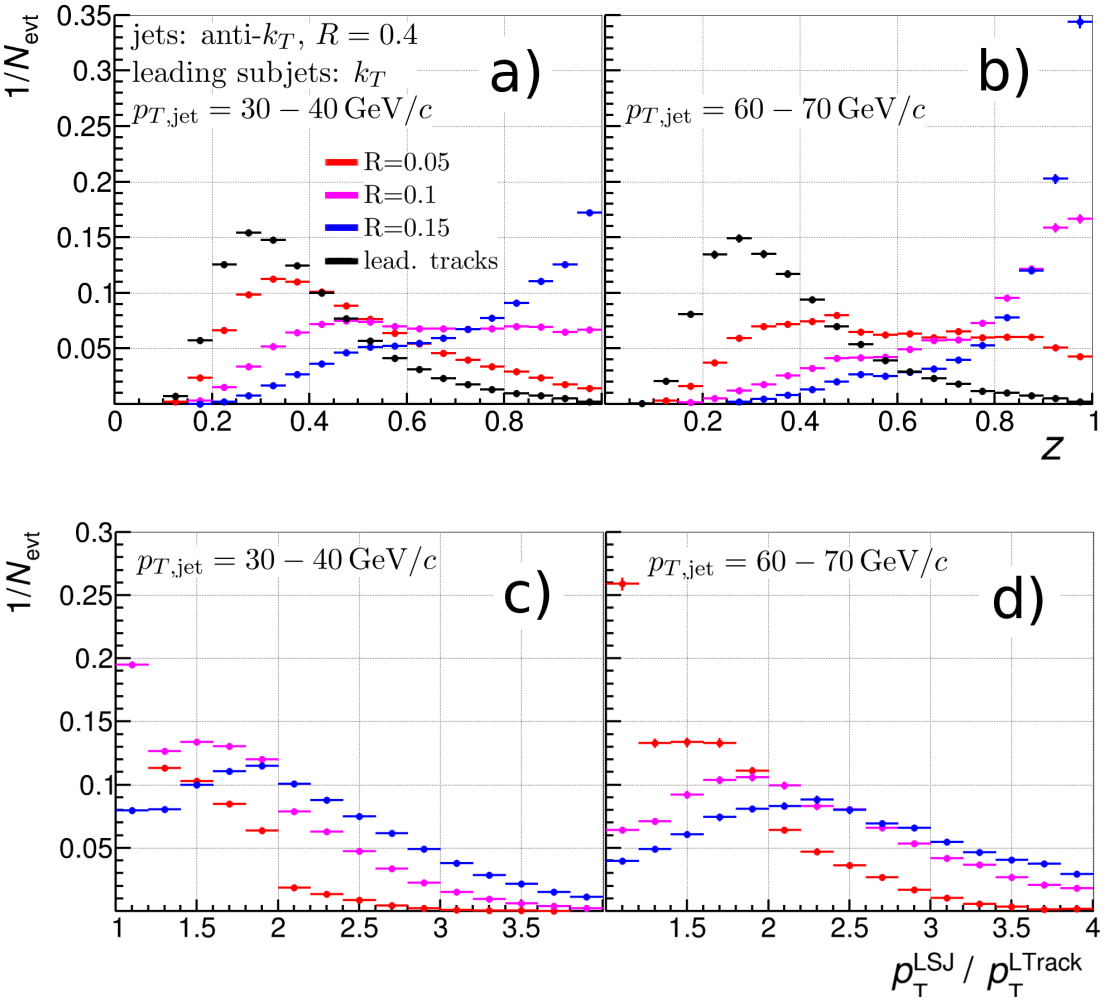

Figure 61: Upper panel: Fragmentation function $F(z)$ of the leading subjet for jet energies a) $30 - 40\,\mathrm{GeV}/c$, b) $60 - 70\,\mathrm{GeV}/c$; the fragmentation function of the leading tracks has been drawn in black for comparison. Lower panel: leading subjet p_T per leading track p_T for jet energies c) $30 - 40\,\mathrm{GeV}/c$, d) $60 - 70\,\mathrm{GeV}/c$. Different subjet resolution parameters have been used: $R = 0.05$ (red), $R = 0.1$ (magenta), $R = 0.15$ (blue). Note that in c) the red data point at the left end goes as high as 0.55 and can not be seen in the figure.

The upper panel of fig. 61 shows the fragmentation function of the leading subjets for different subjet resolution parameters and for two different p_T bins of the jet. From a comparison to the fragmentation function of the leading tracks (black points) and from the lower panel of fig. 61 it can be seen that smaller subjets often contain only the leading particle. This behaviour is not desired, since it is the aim of subjets to cover a broader profile of the jet, i.e. to be more resilient to variations from hadronization and soft splittings. A subjet resolution parameter $R < 0.1$ is therefore inappropriate. A large subjet however may not be as sensitive to the fragmentation pattern (though there is no request for high resolution in the context of this work). Balancing these caveats against each other, it has also to be considered that a jet is more collimated for higher energies of the original parton: As can be seen for the different jet energies, a leading subjet with $R = 0.15$ in $30 - 40\,\mathrm{GeV}/c$ jets yields a similar fragmentation function as a leading subjet with $R = 0.1$ in $60 - 70\,\mathrm{GeV}/c$ jets.

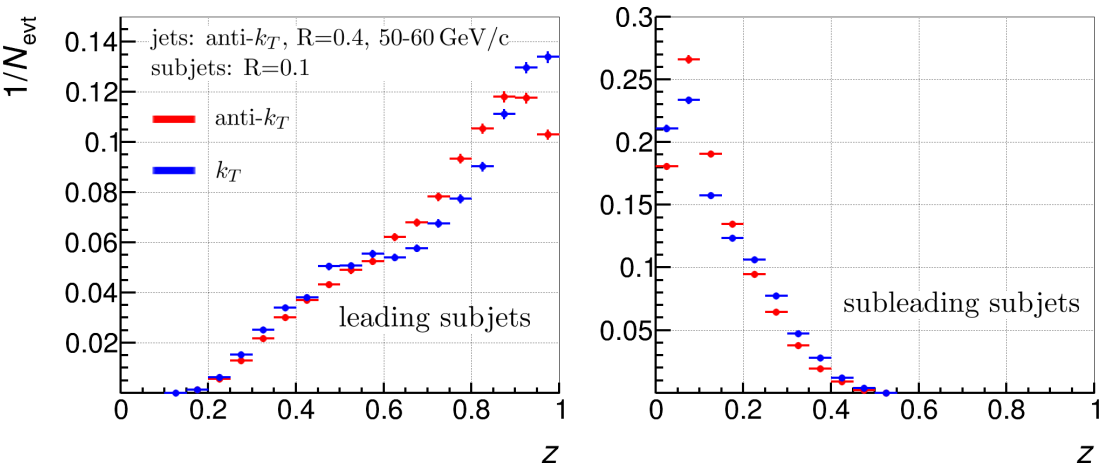

Figure 62: Comparison of subjet algorithms in PYTHIA: The fragmentation function of leading subjets (left) and subleading subjets (right) using the anti-k_t (red) and k_t (blue) jet finder.

It has been observed that the fragmentation functions for the subjets in PYTHIA events depend little on the choice of the subjet algorithm. This is illustrated in fig. 62, where fragmentation functions of leading and subleading anti-k_t (red) and k_t subjets (blue) are compared.

5.2 SUBJET SENSITIVITY AGAINST MEDIUM EFFECTS

The effect of medium effects on subjet observables has been studied with QPYTHIA (section 3.4). QPYTHIA modifies the PYTHIA fragmentation in order to provide a softer and broader parton shower. Fig. 63 illustrates this softening for the number of subjets and the fragmentation function of the tracks within a jet. The quenching power has been chosen so that QPYTHIA yields a $R_{AA} = 0.25$ at $p_T^{Jet} = 40\,GeV/c$. Regardless of the question whether QPYTHIA provides a satisfying reproduction of medium effects or not, it shall serve as a proxy to test the sensitivity of subjet observables against these effects.

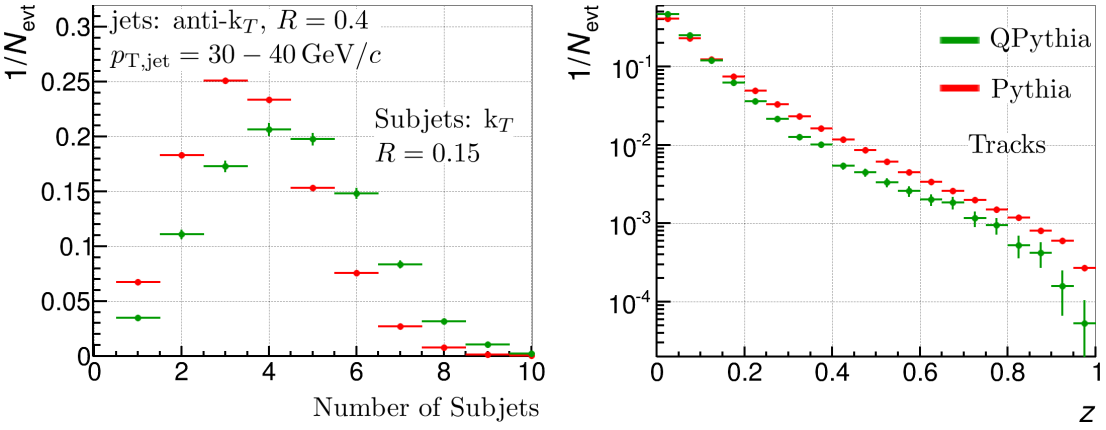

Figure 63: PYTHIA (red) in comparison with QPYTHIA (green): Number of subjets found in a jet (left), fragmentation function of all tracks in the jet (right).

Fig. 64 shows the spatial distance ΔR in the φ-η-plane between the jet axis and the leading subjet axis. It can be seen that QPYTHIA clearly enhances the small fraction of leading subjets that can be found farther away from the jet axis ($\Delta R \gtrsim 0.1$). Note that (Q)PYTHIA does not consider any medium evolution; these results are almost entirely symmetric in η and φ.

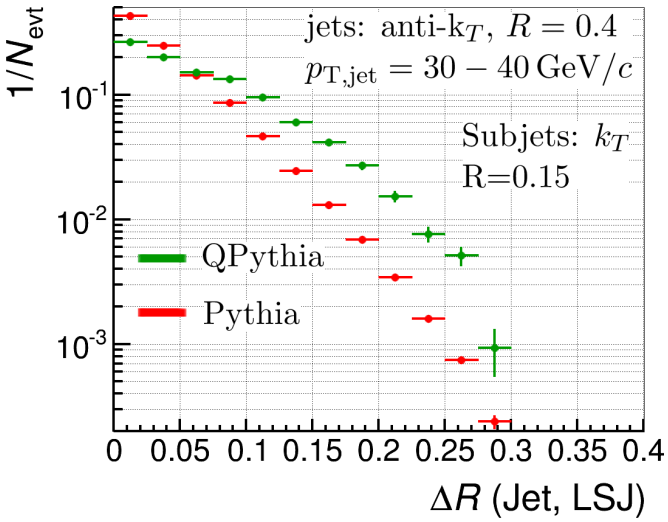

Figure 64: Spatial distance ΔR between the jet axis and the leading subjet axis in PYTHIA (red) and QPYTHIA (green) track populations.

The leading subjet not only reveals the spatial broadening of the jet profile, but also the softening of the constituents as seen in the fragmentation function $F(z)$ of the leading subjet (fig. 65). The fraction of leading subjets with a low z is visibly enhanced for QPythia quenched events. The power of separation between modified and unmodified events is worst for low p_T jets and a small subjet resolution parameter $R = 0.1$. This can again be explained by the fact that such a small leading subjets tends to recover only one track, i.e. the leading track.
Also for the next hardest subjet, the subleading subjet, the conclusion holds that $R = 0.1$ is too small for $p_T^{Jet} = 30 - 40\,GeV/c$ (fig. 66).

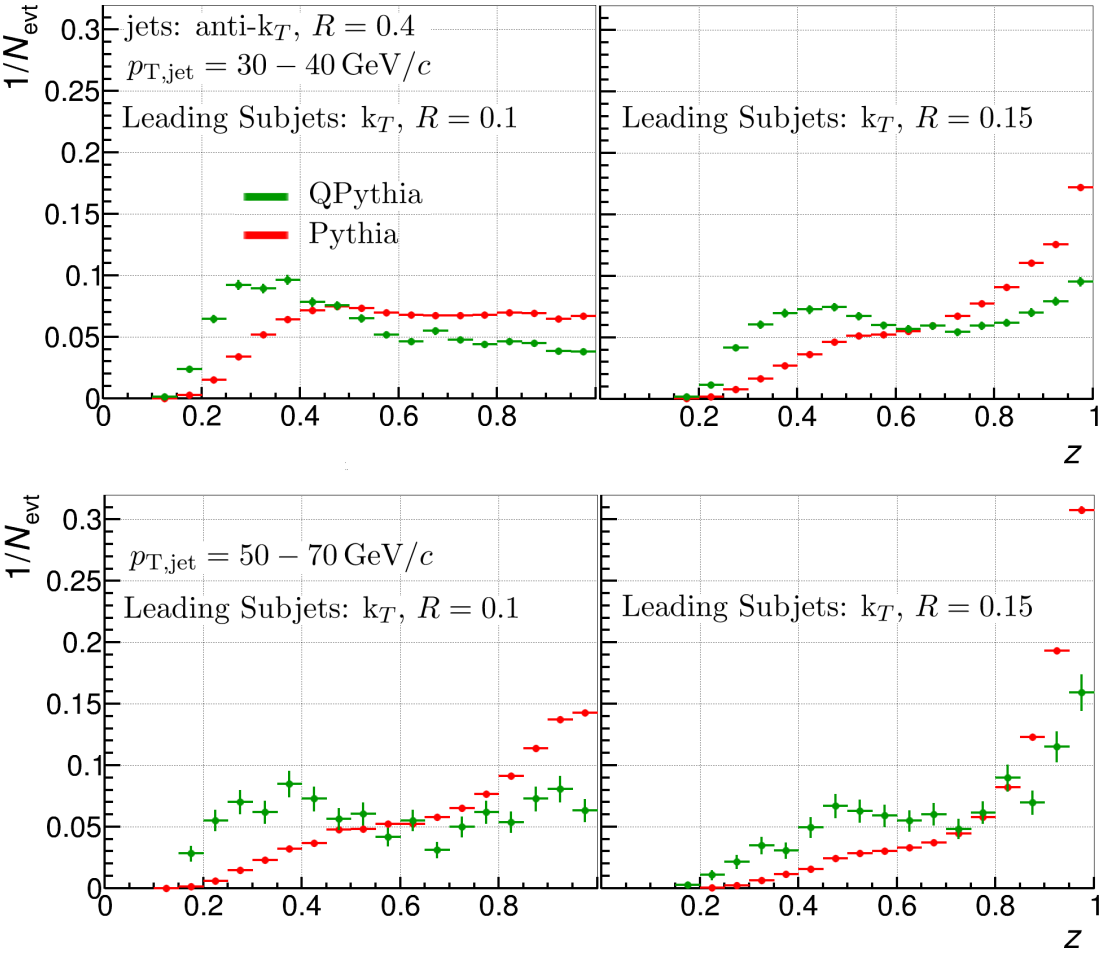

Figure 65: Pythia (red) vs. QPythia (green): Fragmentation function $F(z)$ of the leading subjet for jet tranverse momenta $30 - 40\,GeV/c$ (upper panel), $50 - 70\,GeV/c$ (lower panel), and subjet resolution parameters $R = 0.1$ (left), $R = 0.15$ (right).

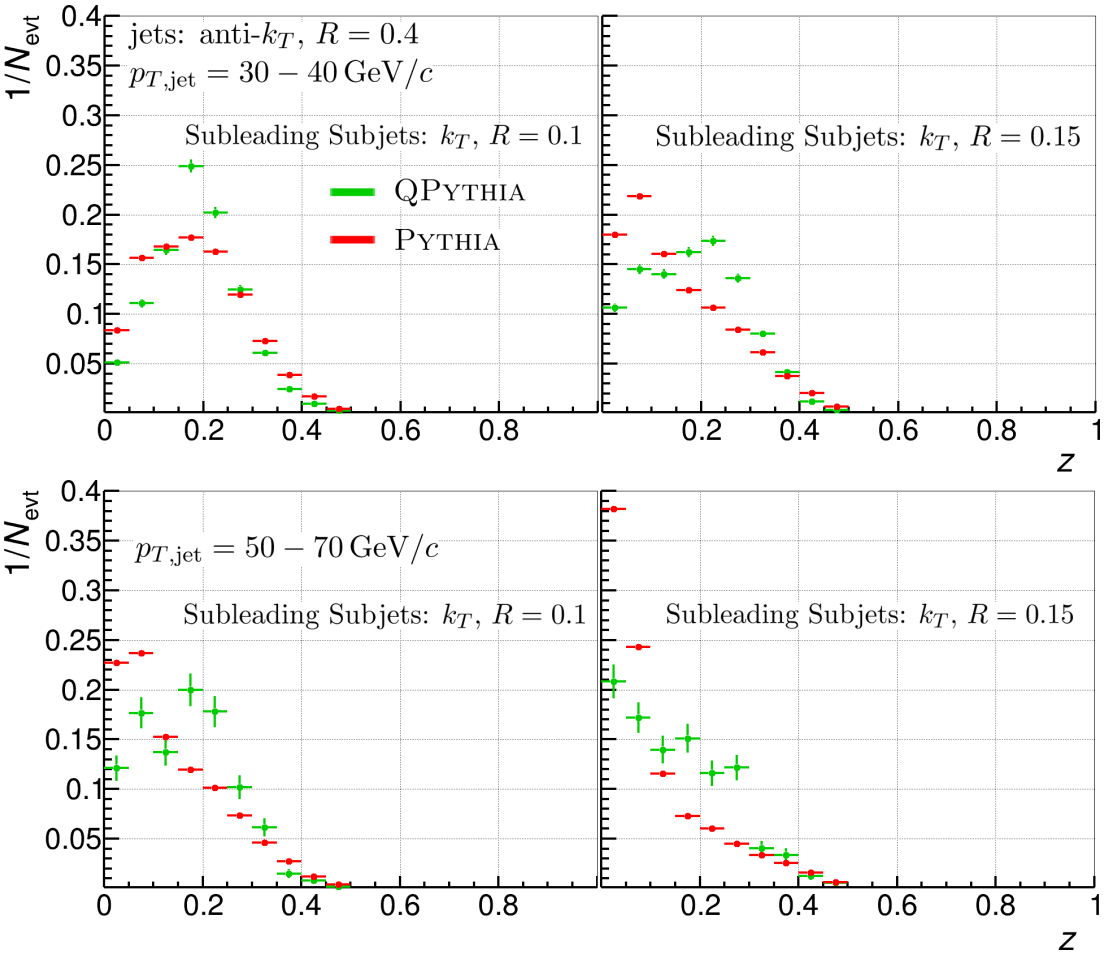

Figure 66: PYTHIA (red) vs. QPYTHIA (green): Fragmentation function $F(z)$ of the subleading subjet for jet tranverse momenta $30-40\,\mathrm{GeV}/c$ (upper panel), $50-70\,\mathrm{GeV}/c$ (lower panel), and subjet resolution parameters $R = 0.1$ (left), $R = 0.15$ (right).

While the fragmentation function of the leading subjet offers a broad range of z to differentiate between modified and unmodified events (with the exception of intermediate z), the subleading subjets allows a discrimination for only a few bins, i.e. $0.15 < z < 0.25$.
Although the subleading subjet shows less sensitivity to the QPythia softening, it may be useful to employ a combination of the leading (LSJ) and subleading (SLSJ) subjet fragmentation function with a modified longitudinal momentum fraction, denoted here as z':

$$z' = \frac{\vec{p}^{\,\mathrm{LSJ}} \cdot \vec{p}^{\,\mathrm{Jet}} - \vec{p}^{\,\mathrm{SLSJ}} \cdot \vec{p}^{\,\mathrm{Jet}}}{|\vec{p}^{\,\mathrm{Jet}}|^2} \tag{56}$$

Since the leading and the subleading subjet are located in a similar region, this observable should effectively cancel contributions from a background. Fig. 67 demonstrates that this $F(z')$ also achieves to separate between QPYTHIA and PYTHIA events.

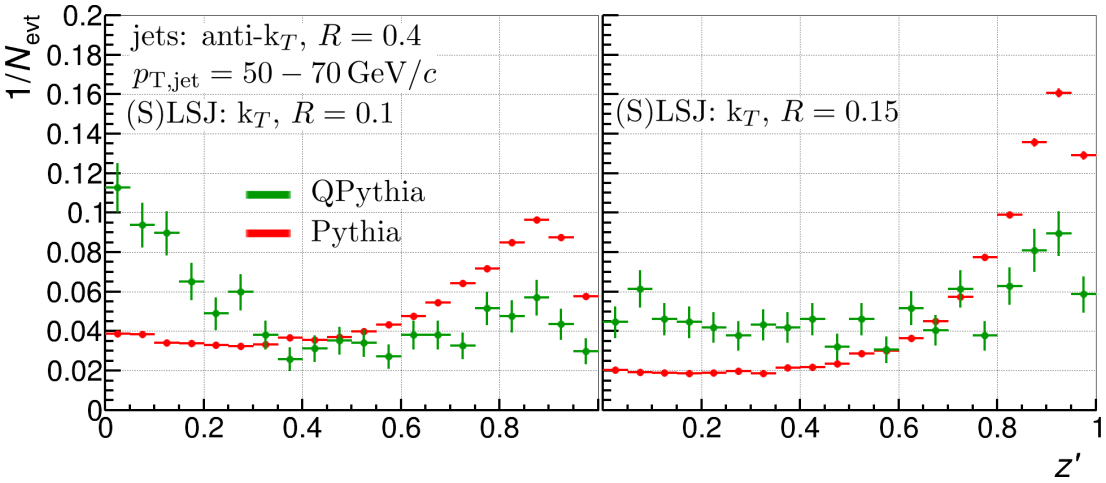

Figure 67: The combined fragmentation function $F(z')$ of leading and subleading subjet for (Q)Pythia events with $R = 0.1$ (left) and $R = 0.15$ (right).

In this section it has been shown that there are viable subjet observables that are sensitive to a modified jet fragmentation pattern. Namely the leading subjet allows a separation both in the η-φ-plane and with regard to the relative energy, i.e. its fragmentation function $F(z)$, respectively the combined fragmentation function $F(z')$ of leading and subleading subjet. The subleading subjet alone does not manage to give a similar power of discrimination.

5.3 TOY MODEL OF THE HEAVY-ION BACKGROUND AND DETECTOR EFFECTS

After the subjet observables have been studied in the undisturbed scenario of (Q)Pythia events, it is now to see how they change within a heavy-ion environment. As given in eq. 14 the bulk of particles arising from a heavy-ion collision can be described as the thermal radiation of the medium. Accordingly, background particles can be added to a Pythia event as provided by the Boltzmann distribution

$$\frac{dN}{dp_T} \simeq \frac{4}{\langle p_T \rangle^2} p_T \exp\left(-\frac{2p_T}{\langle p_T \rangle}\right). \tag{57}$$

The equation employs the high energy approximation $m_T \simeq p_T$ and a slope parameter $\langle p_T \rangle / 2 = 335\,MeV/c$ as determined from a fit of the single hadron spectrum in central Pb-Pb collisions at $\sqrt{s_{NN}} = 2.76\,TeV$. Modifications by anisotropic flow are ignored in here; the particles are distributed homogeneously in φ and η. The sampling of background particles is carried out for a multiplicity of 3100 tracks, a typical multiplicity in central heavy-ion collisions [32]. Only charged particles are considered in this study, so every third track is cut along with the track p_T cut of $150\,MeV/c$.
The background introduces fluctuations and a general increase of the reconstructed jet energy. As discussed in 4.1 a constant energy offset can be corrected for event-by-event, while background fluctuations remain. This approach has been implemented for both the regular jets and the subjets.
A comparison of the two major jet finders (fig. 68) shows that the anti-k_t jet finder provides a larger subjet multiplicity: Anti-k_t subjets are more prone to be unusually small, when most of the subjets are already clustered in circular jets leaving small

patches of remaining tracks.[2] The anti-k_t jet finder should therefore be avoided for observables that include the soft subjets of a jet, for instance an inclusive fragmentation function of all subjets. Both anti-k_t and k_t however provide comparable results for leading and subleading subjets. For the remaining analysis the k_t finder was chosen.

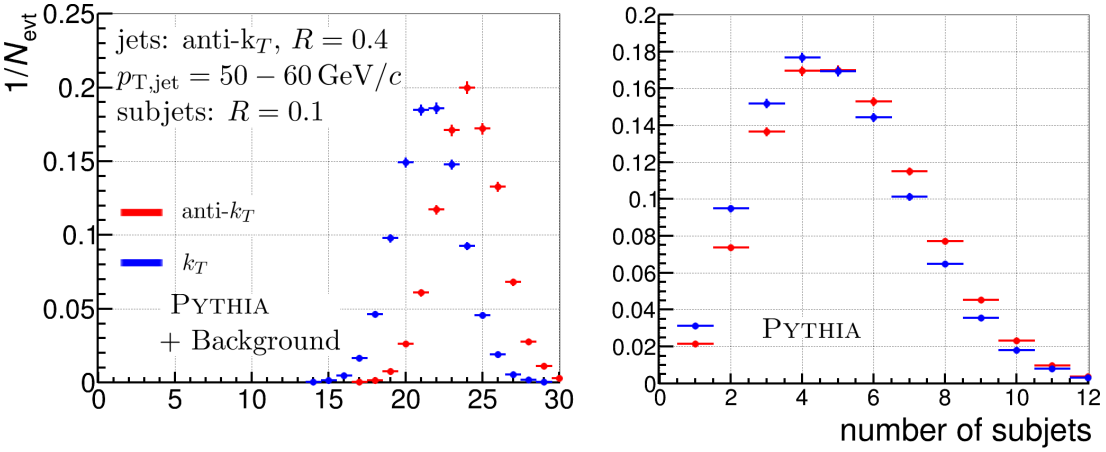

Figure 68: Comparison of subjet algorithms k_t (blue) and anti-k_t (red) in face of a simulated underlying event: Number of subjets in PYTHIA events embedded in a thermal background (left) as opposed to plain PYTHIA events (right).

In QPYTHIA simulations (fig. 63 left or fig. 69 right) the number of subjets in a jet showed a certain sensitivity for the softening of a jet. The discriminating power of this observable however vanishes entirely in face of the simulated thermal background (fig. 69), where the number of subjets saturate due to the high particle multiplicity. This observation disqualifies the number of subjets as an observable sensitive to a modified fragmentation pattern in a high multiplicity environment.

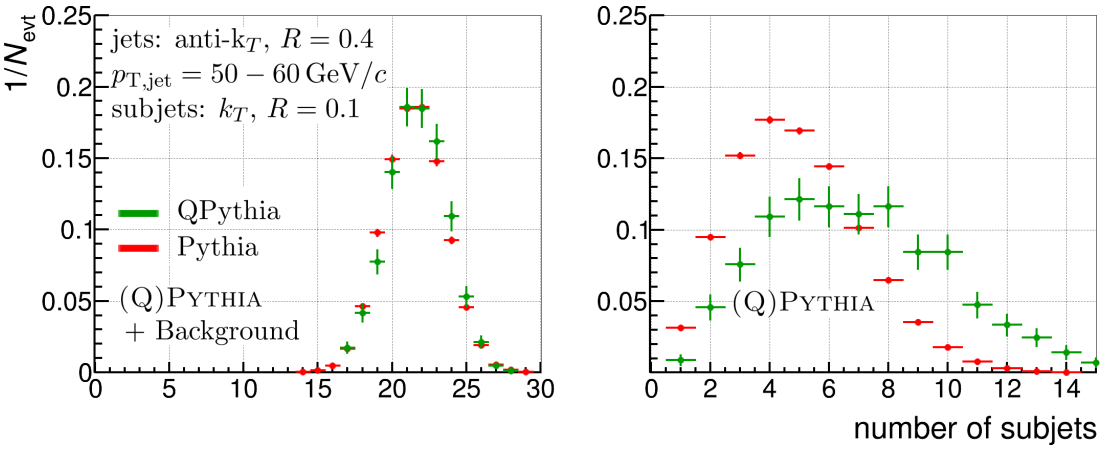

Figure 69: Number of subjets in (Q)PYTHIA events embedded in a thermal background (left) as opposed to plain (Q)PYTHIA events (right).

2 This undesirable behaviour in a crowded track population is the reason why k_t jets are preferred over anti-k_t jets for background density estimation.

Despite the high particle multiplicity it remains possible for the leading subjet to differentiate between a modified and an unmodified jet substructure. This applies both for a geometric discrimination, as seen in the spatial distance ΔR between jet and leading subjet axis (fig. 70), and for an energetic discrimination, as seen in the fragmentation function $F(z)$ of the leading subjet (fig. 71).[3]

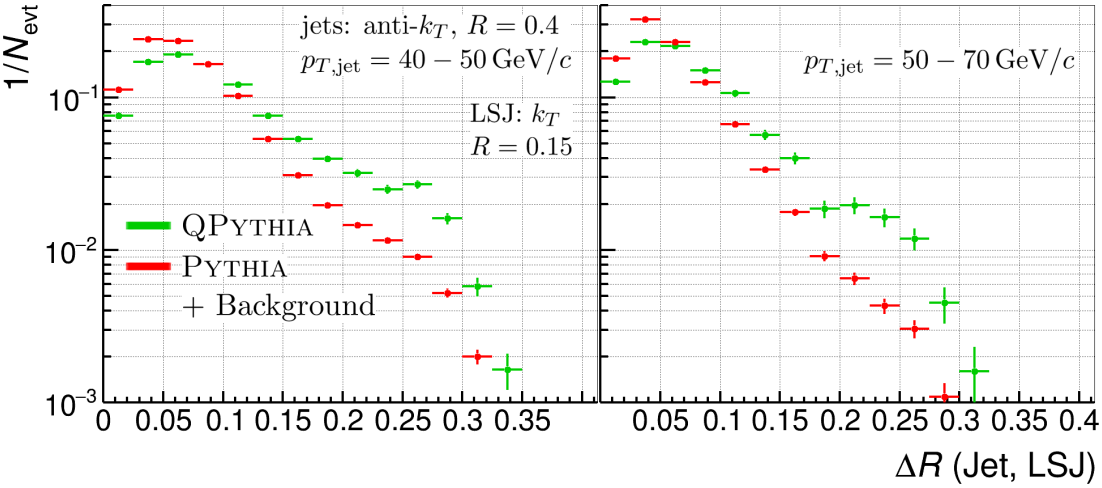

Figure 70: Spatial distance ΔR between the jet axis and the leading subjet axis in PYTHIA (red) and QPYTHIA (green) track populations embedded in the thermal background for $p_T^{Jet} = 40 - 50\,GeV/c$ (left), $p_T^{Jet} = 50 - 70\,GeV/c$ (right).

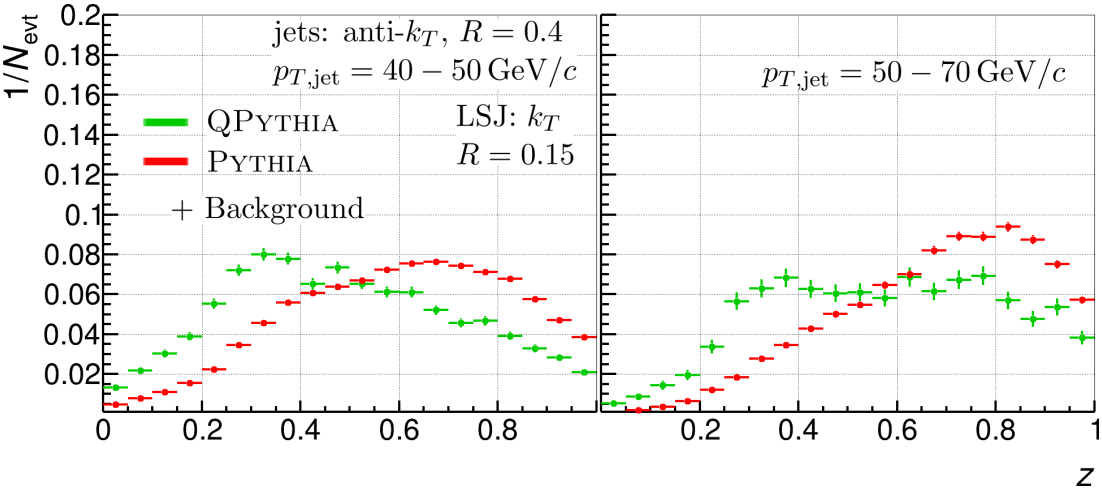

Figure 71: Background corrected fragmentation function of the leading subjet in (Q)PYTHIA events embedded in the thermal background for $p_T^{Jet} = 40 - 50\,GeV/c$ (left), $p_T^{Jet} = 50 - 70\,GeV/c$ (right).

The shape of the fragmentation function changes considerably, as the denominator p_T^{Jet} – despite the correction for a median background density – is now significantly shaped by fluctuating contributions from the background. With the entire jet area filled with energy, leading subjets with a high z are less abundant. Nevertheless,

3 In the last sections it has been shown, that the $R = 0.1$ is a subjet resolution parameter too small, so that here only $R = 0.15$ is considered. Moreover, the minimum jet p_T has been raised to $40\,GeV/c$ in order to be safe from fake jets that stem from upward fluctuations.

the fragmentation function of the leading subjet in a modified event remains visible against the unmodified case. This is understandable as the smearing of $F(z)$ from the fluctuations[4] is still considerably smaller than the energy of a leading subjet, even a quenched one.

While $F(z)$ of the leading subjet maintains the ability to point out a modified fragmentation pattern over a broad range of the longitudinal momentum fraction ($0 < z < 0.5$), the subleading subjet is less robust against the distortion from the background (fig. 72). The already limited discriminating power remains visible over a small z range, but is less pronounced than in the case without the underlying event.

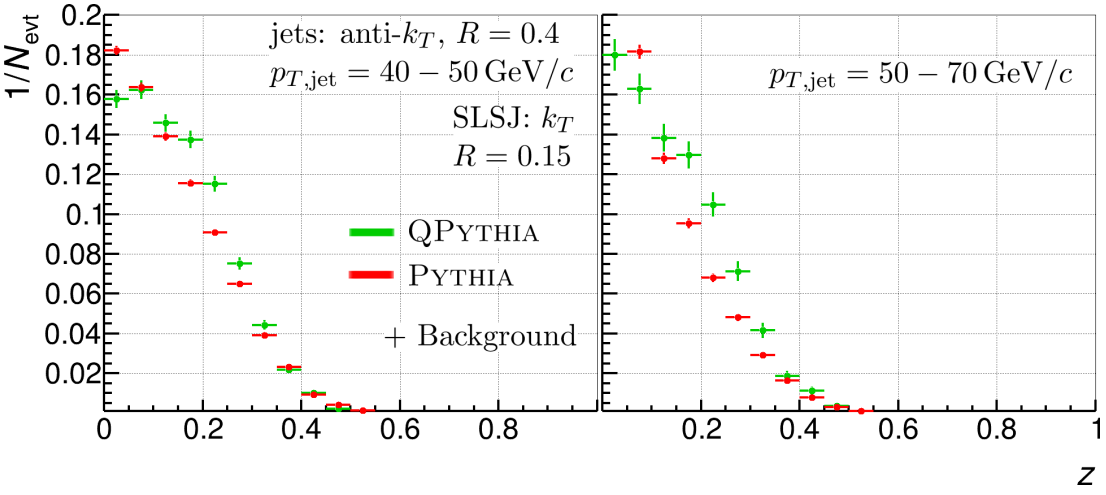

Figure 72: Background corrected fragmentation function of the subleading subjet in (Q)PYTHIA events embedded in the thermal background for $p_T^{Jet} = 40 - 50\,GeV/c$ (left), $p_T^{Jet} = 50 - 70\,GeV/c$ (right).

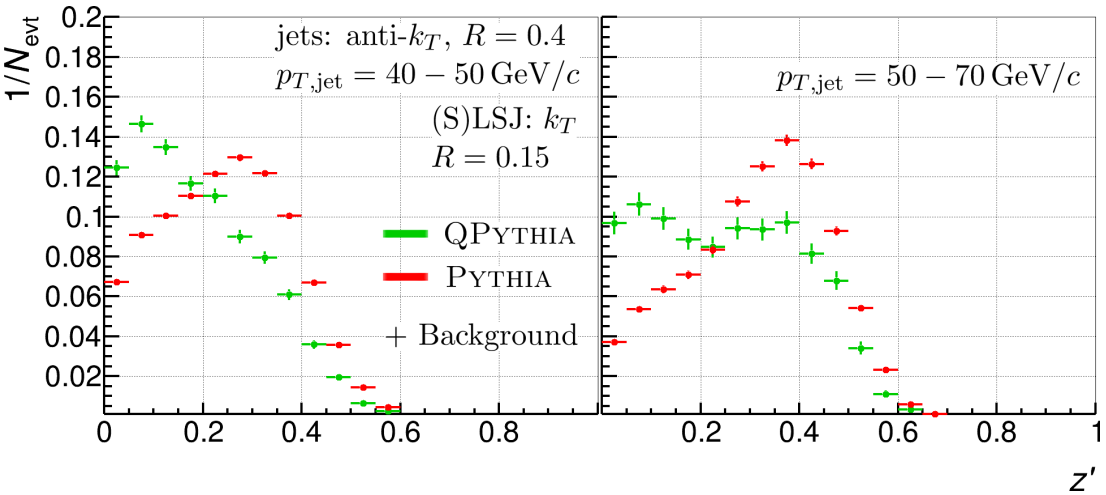

Figure 73: The combined fragmentation function $F(z')$ of leading and subleading subjet for (Q)PYTHIA events embedded in the thermal background for $p_T^{Jet} = 40 - 50\,GeV/c$ (left), $p_T^{Jet} = 50 - 70\,GeV/c$ (right).

4 Note that the background energy density goes with R^2, background fluctuations go with R, so a small jet area should be more prone to energy fluctuations *relative* to the constant energy shift that can be corrected for.

The combined fragmentation function $F(z')$ of the leading and subleading subjet also suffers a visible quality loss from the background (fig. 73). A separation of QPythia and Pythia events is here effectively limited to $z < 0.15$ and $0.2 < z < 0.4$. Confronting the given subjet observables with a simulated heavy-ion background narrowed the choice down to the fragmentation functions that involved the leading subjet. The subleading subjet already is too susceptible to the background fluctuations, losing the ability to effectively identify a modified fragmentation pattern. Subjets with even less energy should accordingly prove even less fruitful in a heavy-ion environment as long as there is no effective method to prevent the distortion from background fluctuations[5].

For a definite conclusion about the experimental feasibility of leading subjets in the experimental environment detector effects are considered in the following. As explained in sec. 4.2, a major distortion of the jet energy scale stems from the finite detector resolution and the imperfect tracking efficiency of the TPC and the ITS. Using a toy model of the detector it will be shown in the following how these experimental shortcomings affect the leading subjet observables.

According to the tracking efficiency (fig. 74 right) tracks are discarded randomly and the momentum of the remaining tracks receive a Gaussian smearing according to the momentum resolution (fig. 74 left).

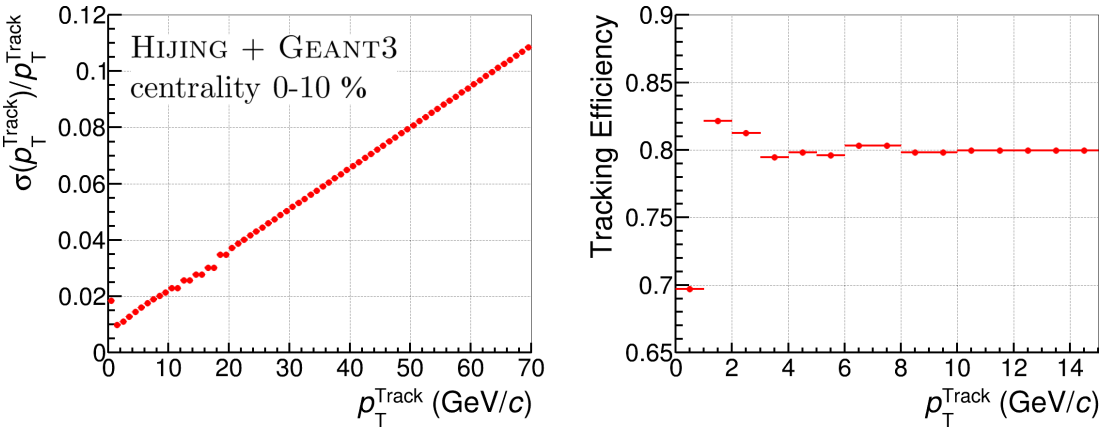

Figure 74: Simulation of detector properties for central Pb-Pb collisions: momentum resolution (left), tracking efficiency (right). The tracking efficiency for $p_T^{Track} > 15\,GeV/c$ (not shown) remains constant at 0.8. Event and detector simulations are provided by [89].

The smearing of the transverse momentum makes little difference to the fragmentation functions, the imperfect tracking efficiency however leads to a visible modification that is illustrated in fig. 75 and fig. 76. The tracking efficiency is poor for tracks of lowest transverse momenta ($150\,MeV/c < p_T < 1\,GeV/c$) and accordingly, the overall jet energy decreases more than the energy of its hard core; the fragmentation functions $F(z)$, $F(z')$ appear slightly harder.

5 A simple cut of the track momentum can provide a remedy for the problem of the background, but again introduces a fragmentation bias. Such p_T cuts have not been taken into consideration in this work.

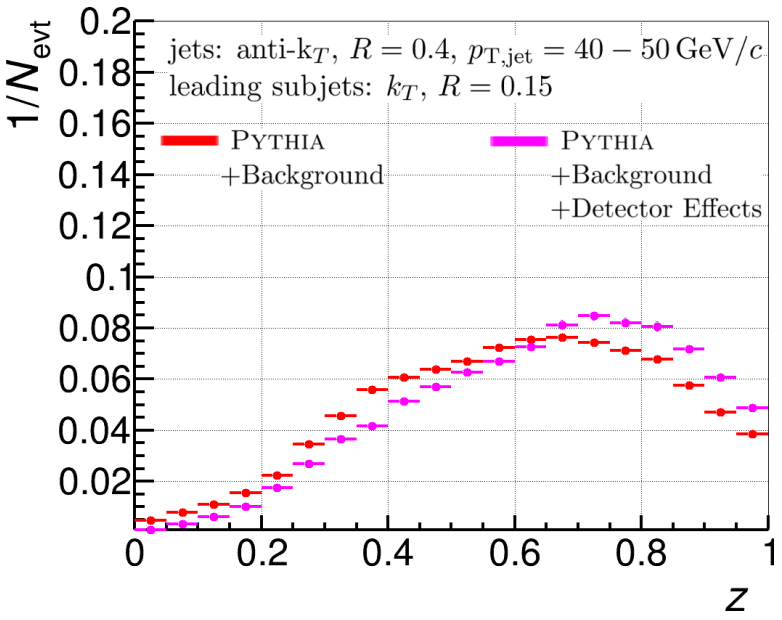

Figure 75: Background corrected fragmentation function of the leading subjet in PYTHIA events embedded in the thermal background with and without detector effects.

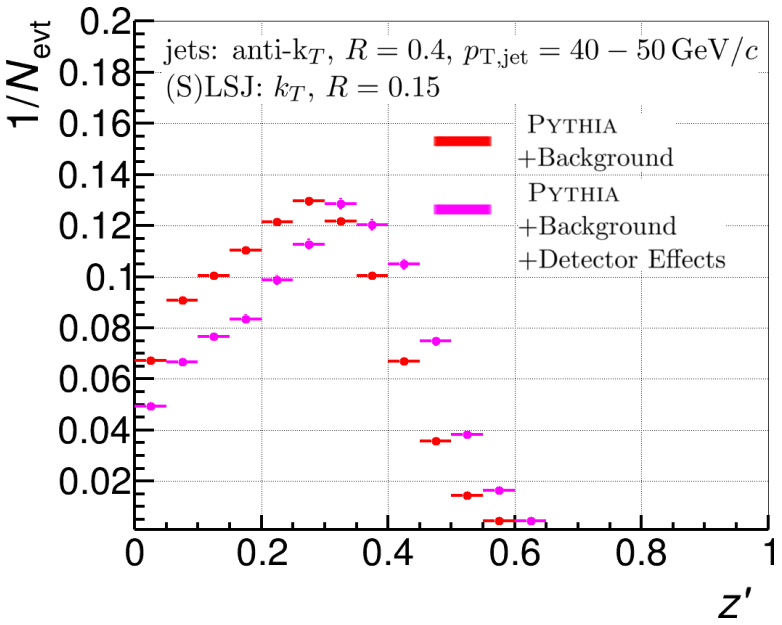

Figure 76: The combined fragmentation function $F(z')$ of leading and subleading subjet for PYTHIA events embedded in the thermal background with and without detector effects. (Sub-)Jets are corrected for the mean background density.

As QPYTHIA and PYTHIA events are almost equally affected by detector effects, the spatial localization of a modified leading subjet (fig. 77) as well as the fragmentation functions $F(z), F(z')$ are insignificantly modified (fig. 78, 79). They keep their viability as a probe that is sensitive to the fragmentation pattern and the same time robust in an experimental heavy-ion environment.

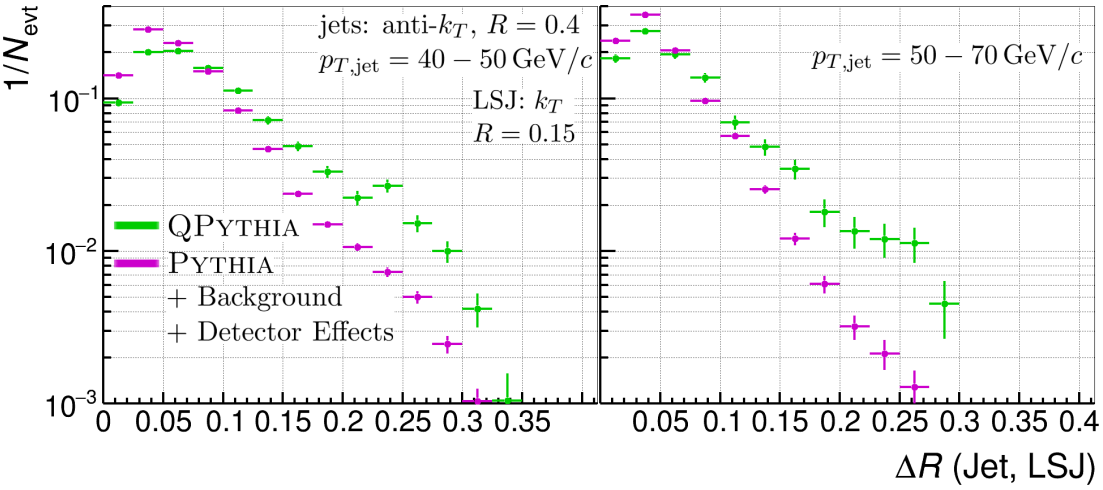

Figure 77: Spatial distance ΔR between the jet axis and the leading subjet axis in PYTHIA (red) and QPYTHIA (green) track populations embedded in the thermal background and applied detector effects for $p_T^{\mathrm{Jet}} = 40 - 50\,\mathrm{GeV}/c$ (left), $p_T^{\mathrm{Jet}} = 50 - 70\,\mathrm{GeV}/c$ (right).

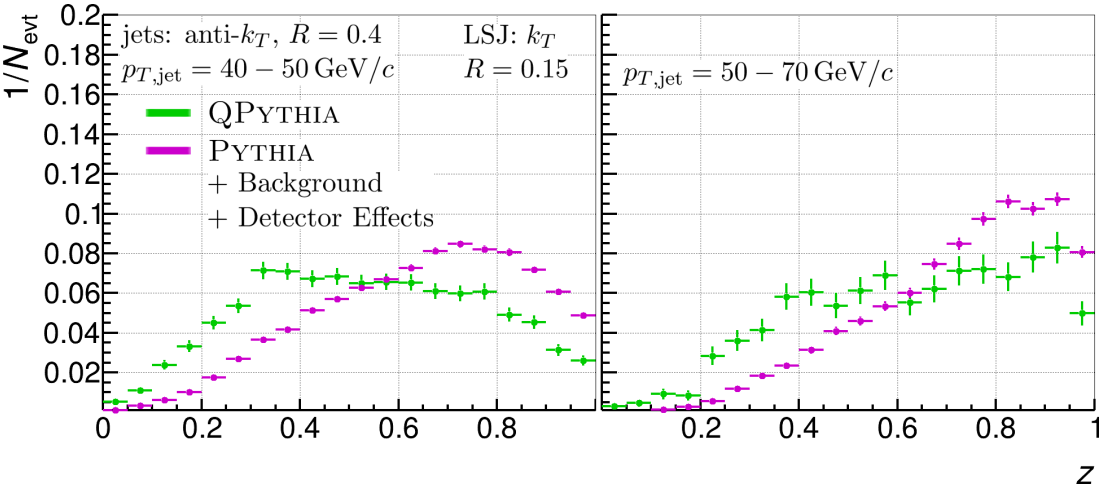

Figure 78: Background corrected fragmentation function of the leading subjet from QPYTHIA events embedded in the thermal background and applied detector effects for $p_T^{\mathrm{Jet}} = 40 - 50\,\mathrm{GeV}/c$ (left), $p_T^{\mathrm{Jet}} = 50 - 70\,\mathrm{GeV}/c$ (right).

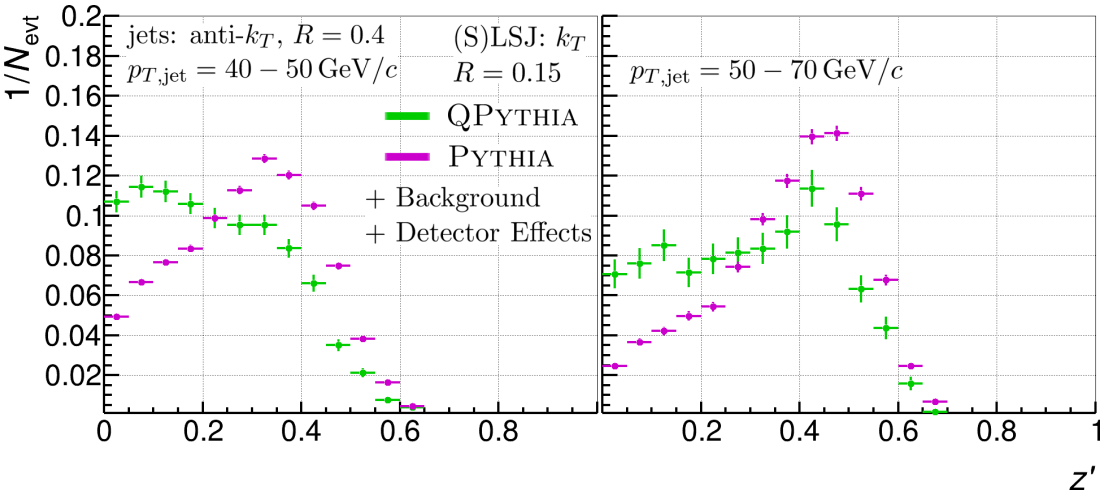

Figure 79: The combined fragmentation function $F(z')$ of leading and subleading subjet for (Q)PYTHIA events embedded in the thermal background and applied detector effects for two jet $p_T^{\text{Jet}} = 40 - 50\,\text{GeV/c}$ (left), $p_T^{\text{Jet}} = 50 - 70\,\text{GeV/c}$ (right).

5.4 SUMMARY & OUTLOOK

With the regard to the upcoming run period of the LHC and the prospect of enhanced statistics, a more differential examination of the jet profile with the help of subjets has been considered feasible. However, subjet observables in the scope of the ALICE experiment are yet poorly understood: It has not been verified which observables are both sensitive to modifications of the medium and robust against the affliction of the heavy-ion environment.
In this chapter, a general subjet analysis has been established that allows to find jets and subjets in a given track population. Subjets of a given jet are energy-ordered, which allows a selection of the leading, subleading subjet etc. Similar to the treatment of regular jets, the median-p_T background subtraction method has been implemented for the subjets.
Subsequently, first steps have been made to examine subjet behaviour in different scenarios. Since the influence of the background remains to be assessed in detail, the natural choice was to focus on the leading and subleading subjets as the most robust entities:

Subjets in PYTHIA events

In PYTHIA6 simulations, general parameters of subjets have been examined. It has been verified that a variation of the collision energy does not change the subjet observables in a given p_T bin of the regular jet. Furthermore, there is little difference between k_t and anti-k_t subjets. For the jet p_T range significant for ALICE it has been shown that a minimal subjet resolution parameter $R \approx 0.1 - 0.15$ is required to maintain the jet-like character, i.e. to recover substantially more than just single tracks. This requirement may vary for higher jet energies, where smaller subjet sizes may suffice for more collimated jets.

Subjets in QPYTHIA events

As a test for medium sensitivity, QPYTHIA has been used to simulate softened/broadened jets. Besides the number of subjets and the distance ΔR between the jet axis and the leading subjet axis, the fragmentation function of the leading subjet is most sensitive to the quenching provided by QPYTHIA. Especially a combination with the fragmentation function of the subleading subjet has found to be promising for the appliance in a heavy-ion environment.

The influence of a thermal background and detector effects

In order to assess the subjet observable for practical application in real Pb-Pb events (Q)PYTHIA events have been embedded in an isotropic heavy-ion background. Moreover, the tracking efficiency and the momentum resolution has been accounted for by a detector toy model. It has been found that for soft subjets the anti-k_t jet finder yields irregular jet shapes in face of the high particle multiplicity. The high particle multiplicity again leads to a saturation of number of subjets in a jet, disqualifying this observable in a heavy-ion environment. The fragmentation function $F(z)$, $F(z')$ involving the leading subjet maintain their sensitivity to the fragmentation pattern

and are able to discriminate between quenched and unquenched jets. A simulation of detector effects further confirmed an experimental feasibility.
The subleading subjet so far disqualifies as a probe that is robust against the heavy-ion background. Accordingly, this marks a limit of energy flow (i.e. $p_T^{SLSJ} \approx 10\,\mathrm{GeV/c}$ with $R = 0.15$), where different subtraction methods or p_T cuts have to be considered.

Outlook

- With the demonstrated sensitivity against a modified fragmentation pattern (sub-)leading subjets can already be used to test model predictions more differentially, rather than by coarse quantities like the nuclear modification factor.
- QPYTHIA events have been employed to approximate possible medium effects. Above all, it has been used because it is easily implemented. But although it provides a general softening and broadening of jets, QPYTHIA hardly gives a realistic description of jet quenching. A valuable extension of the analysis setup would therefore be the implementation of advanced jet quenching generators like JEWEL [90], which derives medium modifications from first principles.
- It is not ensured that the conventional median-p_T method suffices to correct the energy scale of the subjets. As the most energetic part of the jet, the leading subjet naturally shows little disturbance by the background, yet other subjet observables - that may access the soft, outer part of the jet - will be distorted more severely. One has to note that the large jet, whose energy scale is already distorted by background fluctuations, again contains background fluctuations within, which gives rise to another level of energy distortion concerning subjets. For that matter, a quantitative analysis of the subjet susceptibility to fluctuations remains to be done. After all, a new background subtraction method may be required.
- For a more comprehensive feasibility study of subjets, it is required to simulate a more realistic heavy-ion background that above all includes anisotropic flow. A simplified scenario of central Pb-Pb collisions has already been given in this work; a centrality-differential study remains to be carried out.
- Subjets have to be examined in p-p collisions, as they constitute the baseline for medium effects. p-Pb collisions may provide a fruitful scenario to examine subjets among a moderate background.
- The sensitivity to the fragmentation pattern makes subjet observables a promising tool for the study of quark and gluon jets.
- Jets show resilience against fluctuations in the non-pertubative stage of the fragmentation. One can therefore easily anticipate that the conventional leading track p_T cut reducing the background may be discarded in favor of a leading subjet cut.

SUMMARY

In this work the charged jet yield of heavy-ion collisions has been corrected for detector effects and background fluctuations. The underlying data was given by Pb-Pb collisions carried out at the ALICE experiment in 2011 at the LHC with a center-of-mass energy of $\sqrt{s_{NN}} = 2.76\,\text{TeV}$. The correction has been performed with a χ^2 unfolding, where the parameters involved have been examined and a systematic uncertainty for the procedure was given.
Considering given uncertainties and a systematic discrepancy that stems presumably from the unfolding procedure, the corrected spectrum agrees fairly with similar results based on 2010 Pb-Pb collisions.
The corrected charged jet yield has furthermore been used to construct the nuclear modification factor R_{AA} with a p-p reference from PYTHIA simulations. Given a jet suppression of around 0.25 at $p_T = 40\,\text{GeV/c}$ with a mild rise to 0.35 at $p_T = 110\,\text{GeV/c}$, the reported effect of the medium agrees well with recent full jet measurements from ALICE and ATLAS.
Prospects of further research on jet suppression are intimately related to the upcoming second run season of the LHC. In the Pb-Pb run scheduled for November 2015 the collision energy will be increased to $\sqrt{s_{NN}} = 5.1\,\text{TeV}$. The aim is to collect data of an integrated luminosity of around $1\,\text{nb}^{-1}$, which is roughly ten times more than in 2011 and a hundred times more than in 2010. The higher collisions energy means a new physics scenario with new questions (e.g. does a higher collision energy imply a higher suppression?); The richer statistics allow to extend the maximal jet p_T range of ALICE, which in return means that systematic uncertainties may become limiting factors such as the uncertainty related to the high-p_T tracking performance.

Apart from an improvement of well established quantities like the nuclear modification factor, the prospect of higher statistics motivate more differential jet measurements and new observables. Amongst a variety of proposals it has been suggested that the jet structure can be examined more closely with smaller *subjets* within a jet. This work constitutes one of the earliest assessments of this observable: An analysis setup has been developed that allows to study subjets in various scenarios. (Q)Pythia simulations along with a toy model of both the heavy-ion background and the detector have been used in this work. Robust against background fluctuations, the fragmentation function of the leading subjet has been proven to provide sensitivity against medium effects even in a heavy-ion environment. The analysis setup provides the opportunity for further studies on subjets, e.g. with a more realistic background model/detector simulation, the examination of jet quenching models or a differential study concerning quark and gluon jets.

A

UNFOLDING

Listing 1: Numbers of the LHC runs used for unfolding. Check on alimonitor.cern.ch or twiki.cern.ch/twiki/bin/viewauth/ALICE/JELHC11hTrackQA for information on run conditions.

```
167903 167915 167987 167988 168066 168068 168069 168076 168104 168107 168108
168115 168212 168310 168311 168322 168325 168341 168342 168361 168362 168458
168460 168461 168464 168467 168511 168512 168777 168826 168984 168988 168992
169035 169040 169044 169045 169091 169094 169099 169138 169143 169144 169145
169148 169156 169160 169167 169238 169411 169415 169417 169418 169419 169420
169475 169498 169504 169506 169512 169515 169550 169553 169554 169555 169557
169584 169586 169587 169588 169590 169591 169835 169837 169838 169846 169855
169858 169859 169923 169956 169975 169981 170027 170036 170038 170040 170081
170083 170084 170085 170088 170089 170091 170152 170155 170159 170163 170193
170195 170203 170204 170205 170228 170230 170264 170268 170269 170270 170306
170308 170309
```

B

SUBJETS

Three figures that exemplify subjet observables in PYTHIA events with different collision energies are given in the following. Anti-k_T jets ($R = 0.4$) with $p_{T,jet} = 50 - 60\,GeV/c$ have been used and k_T subjets ($R = 0.1$).

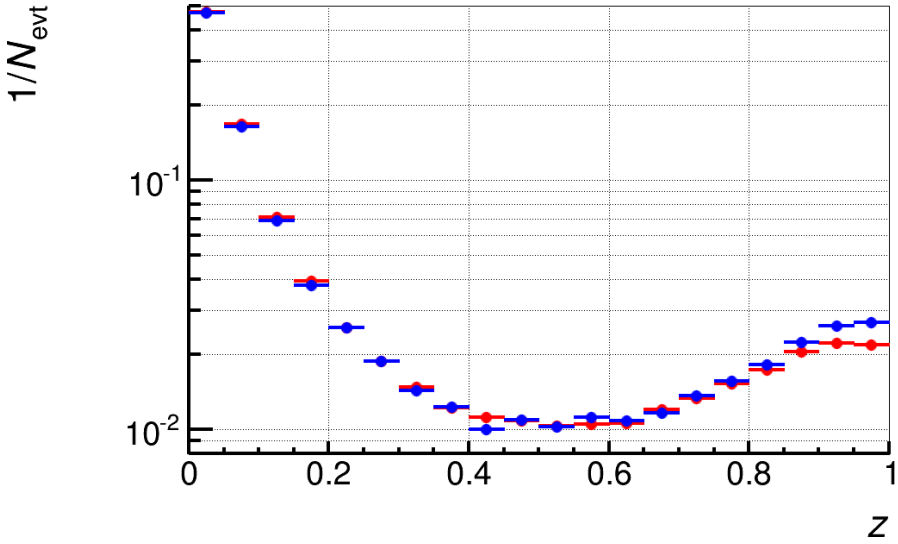

Figure 80: inclusive k_T subjet ($R = 0.1$) fragmentation function at different collision energies: 2.76 TeV (red), 5.1 TeV (blue).

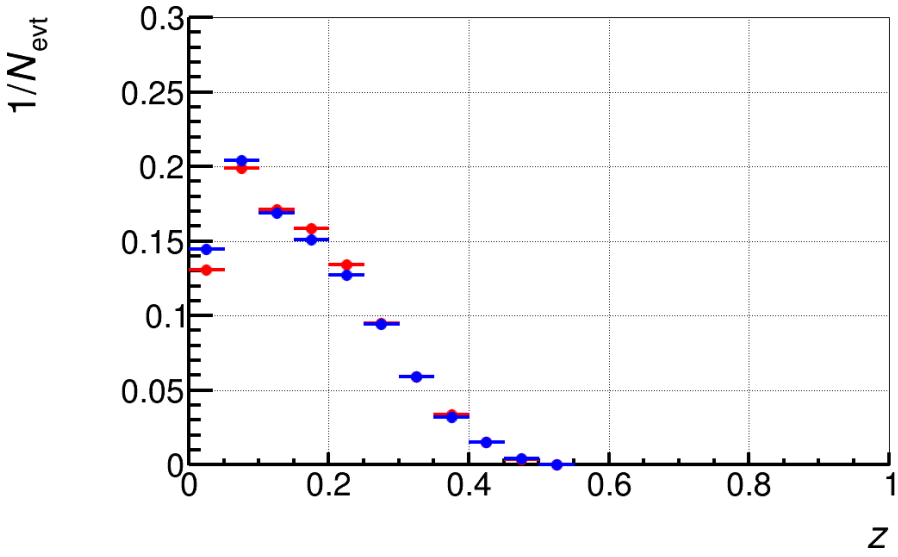

Figure 81: k_T subleading subjet ($R = 0.1$) fragmentation function at different collision energies: 2.76 TeV (red), 5.1 TeV (blue).

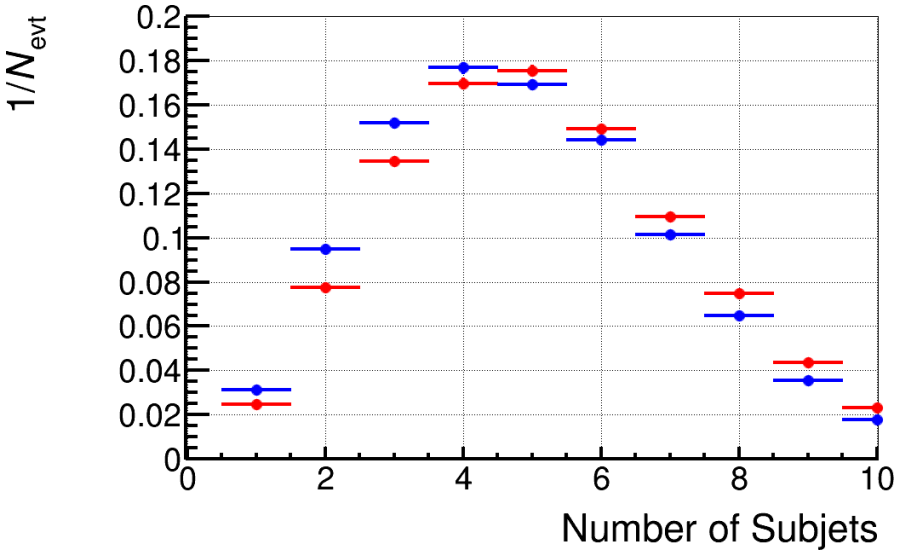

Figure 82: Number of k_T subjets ($R = 0.1$) per jet at different collision energies: 2.76 TeV (red), 5.1 TeV (blue).

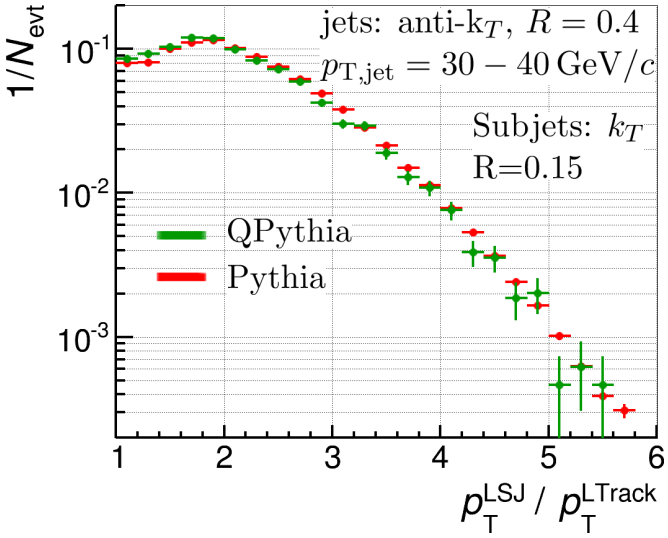

Figure 83: PYTHIA (red), QPYTHIA (green): Leading subjet p_T per leading track p_T. This graph illustrates that QPYTHIA softens the leading track and the softer fragments almost equally, so that this ratio is similar to the PYTHIA case.

BIBLIOGRAPHY

[1] T. Hatsuda *et al.*, "Quark-Gluon Plasma", Cambridge University Press, 2005. 1, 9, 10, 17, 18, 19, 20, 22

[2] J. Thomson, "On the Structure of the Atom: an Investigation of the Stability and Periods of Oscillation of a number of Corpuscles arranged at equal intervals around the Circumference of a Circle; with Application of the Results to the Theory of Atomic Structure", *Philosophical Magazine* **Series 6. 7, Nr. 39** (1904) 237–265. 2

[3] E. Rutherford, "The Scattering of alpha and beta Particles by Matter and the Structure of the Atom", *Philosophical Magazine* **Series 6, vol. 21** (1911) 669–688. 2

[4] C. Weizsäcker, "Zur Theorie der Kernmassen", *Zeitschrift für Physik* **96** (1935) 431 ff. 2

[5] M. G. Mayer, "On Closed Shells in Nuclei. II", *Phys. Rev.* **75** Jun (1949) 1969–1970. 2

[6] H. Yukawa, "On the Interaction of Elementary Particles. I", *Proceedings of the Physico-Mathematical Society of Japan. 3rd Series* **17** (1935) 48–57. 3

[7] C. M. G. e. a. Lattes, "Processes Involving Charged Mesons", *Nature* **159** (1947) 694–697. 3

[8] G. Zweig, "An SU(3) model for strong interaction symmetry and its breaking. Version 1", *CERN-TH-401*, 1964. 3

[9] M. Gell-Mann, "A Schematic Model of Baryons and Mesons", *Phys.Lett.* **8** (1964) 214–215. 3

[10] B. Muller, J. Schukraft, and B. Wyslouch, "First Results from Pb+Pb collisions at the LHC", arxiv:hep-ex/1202.3233. 3

[11] Povh *et al.*, "Teilchen und Kerne, 8. Auflage", Springer Verlag, 2009. 4, 5, 8

[12] W. Atwood, "Lectures on Lepton Nucleon Scattering and Quantum Chromodynamics", *Progress in Physics* **4** (1982). 4

[13] C. Klein-Boesing, "Study of the Quark-Gluon Plasma with Hard and Electromagnetic Probes", 2013. http://qgp.uni-muenster.de/thesisdb/habil-klei-13.pdf. 6, 7, 12, 17, 21, 27, 32

[14] C. Berger, "Elementarteilchenphysik", Springer Verlag, 2006. 6, 7

[15] T. Liu, Y. Mao, and B.-Q. Ma, "Present status on experimental search for pentaquarks", arxiv:hep-ex/1403.4455. 7

[16] D. H. Perkins, "Introduction to High Energy Physics", Cambridge University Press, 2000. 8

[17] E. S. Swanson, "The Flux tube model: Applications, tests, and extensions", arXiv:hep-ph/0311328. 9

[18] Z. Fodor and C. Hoelbling, "Light Hadron Masses from Lattice QCD", *Rev. Mod. Phys.* **84,** (2012) 449, 1203.4789. 9

[19] F. Karsch, E. Laermann, and A. Peikert, "The pressure in 2, 2 + 1 and 3 flavour QCD", *Physics Letters B* **478** Apr (2000) 447,455. 11

[20] B. S. Sourav Sarkar, Helmut Satz, "The Physics of the Quark-Gluon Plasma", *Springer Verlag*, 2010. 11, 21, 22, 23

[21] H. Poppenborg, "Characterisation of Heavy-Ion-Background in Jet-Reconstruction", Master's thesis, 2011. http://qgp.uni-muenster.de/thesisdb/batch-hpop-11.pdf. 14

[22] **ATLAS** Collaboration, G. Aad *et al.*, "The ATLAS Experiment at the CERN Large Hadron Collider", *JINST* **3** (2008) S08003. 14, 31

[23] B. Back *et al.*, "The PHOBOS Perspective on Discoveries at RHIC", arXiv:nucl-ex/0410022. 15, 30

[24] B. Back, "The significance of the fragmentation region in ultrarelativistic heavy ion collisions", *Phys.Rev.Lett.* **91:052303,2003** arXiv:nucl-ex/0210015. 15

[25] K. Filimonov, "Overview of results from the STAR experiment at RHIC", arXiv:hep-ex/0306056. 16

[26] E. Schnedermann, J. Sollfrank, and U. Heinz, "Thermal phenomenology of hadrons from 200 AGeV S+S collisions", *Phys.Rev.C* **48:2462-2475,1993** (Phys.Rev.C48:2462-2475,1993) arxiv:nucl-th/9307020. 16

[27] J. Bjorken, "Highly relativistic nucleus-nucleus collisions: The central rapidity region", *Phys. Rev. D*, 1983. 17

[28] L. K. Graczykowski and for the ALICE Collaboration, "Pion femtoscopy measurements in ALICE at the LHC", arxiv:hep-ex/1402.2138. 18

[29] C. Wong, "Introduction to High-Energy Heavy-Ion Collisions", World Scientific Pub Co, 1994. 18

[30] K. Reygers and for the ALICE collaboration, "A Quick Tour of Ultra-Relativistic Heavy-Ion Physics at the LHC", arxiv:nucl-ex/1208.1626. 18

[31] M. L. Miller *et al.*, "Glauber Modeling in High-Energy Nuclear Collisions", *Annual Review of Nuclear and Particle Science* **57** Nov (2007) 205–243. 18, 20

[32] K. Aamodt *et al.*, "Charged-particle multiplicity density at mid-rapidity in central Pb-Pb collisions at sqrt(sNN) = 2.76 TeV", *Phys.Rev.Lett.* **105:252301,2010** (2010) arxiv:nucl-ex/1011.3916. 20, 32, 60

[33] H. Satz, "Quarkonium Binding and Dissociation: The Spectral Analysis of the QGP", *Nucl.Phys.A* **783:249-260,2007** (Nucl.Phys.A783:249-260,2007) arxiv:hep-ph/0609197. 22

[34] A. Majumder and M. V. Leeuwen, "The theory and phenomenology of perturbative qcd based jet quenching", *Prog.Part.Nucl.Phys* **66** (2010) 41–92, arxiv:hep-ph/1002.2206. 22

[35] Y. Dokshitzer *Sov. Phys. JETP* **46** (1977) 641. 23

[36] V. Gribov and L. Lipatov *Sov. J. Nucl. Phys.* **15** (1972) 438. 23

[37] G. Altarelli and G. Parisi *Nucl. Phys.* **B126** (1977) 298. 23

[38] Y. L. Dokshitzer and D. E. Kharzeev, "Heavy quark colorimetry of QCD matter", *Phys.Lett.B* **519:199-206,2001** (Phys.Lett.B519:199-206,2001) arxiv:hep-ph/0106202. 23

[39] S. D. Ellis and D. E. Soper, "Successive Combination Jet Algorithm For Hadron Collisions", *Phys.Rev.D* **48:3160-3166,1993** (Phys.Rev.D48:3160-3166,1993) arxiv:hep-ph/9305266. 24

[40] M. Cacciari, G. P. Salam, and G. Soyez, "The anti-kt jet clustering algorithm", *JHEP* **0804:063,2008** (2008) arxiv:0802.1189. 24, 25

[41] M. Cacciari, "Talk at 25th Indian-Summer School of Physics", 2013. http://rafael.ujf.cas.cz/school13/presentations/Cacciari2.pdf. 25, 26

[42] M. Dasgupta, L. Magnea, and G. P. Salam, "Non-perturbative QCD effects in jets at hadron colliders", *JHEP* **0802:055,2008** (2007) arxiv:0712.3014. 26

[43] C. Collaboration, "Measurement of isolated photon production in pp and PbPb collisions at sqrt(sNN) = 2.76 TeV", *Phys. Lett. B* **710** (2012) 256, arxiv:1201.3093. 27

[44] R. Haake and for the ALICE collaboration, "Charged Jets in Minimum Bias p-Pb Collisions at sqrt(s) = 5.02 TeV with ALICE", arxiv:1310.3612. 27

[45] K. Werner *et al.*, "Flow in pPb collisions at 5 TeV?", arxiv:1405.0664. 27

[46] **CMS** Collaboration, "Charged particle nuclear modification factor and pseudorapidity asymmetry in pPb collisions at sqrt(sNN)=5.02 TeV with CMS", Tech. Rep. CMS-PAS-HIN-12-017, CERN, Geneva, 2013. 27

[47] M. Verweij, "Modelling and measurement of jet quenching in relativistic heavy-ion collisions at the LHC", PhD thesis, Utrecht, 2013. http://www.nikhef.nl/pub/services/biblio/theses_pdf/thesis_M_Verweij.pdf. 28, 36, 44

[48] A. Collaboration, "Measurement of charged jet suppression n Pb-Pb collisions at sqrt(sNN)=2.76TeV", arxiv:1311.0633. 28, 39, 47, 51, 53

[49] C. Collaboration, "Modification of jet shapes in PbPb collisions at sqrt(s[NN]) = 2.76 TeV", *Phys. Lett. B* **730** (2013) 243, arxiv:1310.0878. 29

[50] K. Reygers, "Die Suche nach dem Quark-Gluon-Plasma mit dem PHENIX - Experiment am RHIC", 2004. http://qgp.uni-muenster.de/thesisdb/reygers_habil.pdf. 30

[51] I. Arsene *et al.*, "Quark–gluon plasma and color glass condensate at RHIC? The perspective from the BRAHMS experiment", *Nuclear Physics A* **757** Aug (2005) 1–27. 30

[52] K. Adcox *et al.*, "Formation of dense partonic matter in relativistic nucleus–nucleus collisions at RHIC: Experimental evaluation by the PHENIX Collaboration", *Nuclear Physics A* **757** Aug (2005) 184–283. 30

[53] J. Adams *et al.*, "Experimental and theoretical challenges in the search for the quark–gluon plasma: The STAR Collaboration's critical assessment of the evidence from RHIC collisions", *Nuclear Physics A* **757** Aug (2005) 102–183. 30

[54] A. Collaboration, "Observation of a new particle in the search for the Standard Model Higgs boson with the ATLAS detector at the LHC", *Phys.Lett. B* **716** (2012) 1–29, arxiv:1207.7214. 31

[55] **CMS** Collaboration, S. Chatrchyan *et al.*, "The CMS experiment at the CERN LHC. The Compact Muon Solenoid experiment", *J. Instrum.* **3** (2008) S08004. 361 p, Also published by CERN Geneva in 2010. 31

[56] C. Collaboration, "Observation of a new boson at a mass of 125 GeV with the CMS experiment at the LHC", *Phys. Lett. B* **716** (2012) 30, arxiv:1207.7235. 31

[57] K. Aamodt *et al.*, "The ALICE experiment at the CERN LHC", *Journal of Instrumentation* **3** Aug (2008). 31, 32

[58] **LHCb** Collaboration, A. A. e. a. Alves, "The LHCb Detector at the LHC", *J. Instrum.* **3** (2008), no. LHCb-DP-2008-001. CERN-LHCb-DP-2008-001, S08005, Also published by CERN Geneva in 2010. 31

[59] J. Kaspar, "TOTEM Experiment: Elastic and Total Cross Sections", arxiv:1204.5689. 31

[60] "The LHCf detector at the CERN Large Hadron Collider", 2013. http://home.web.cern.ch/about/experiments/lhcf. 31

[61] C. Lefevre, "LHC: the guide (English version). Guide du LHC (version anglaise)", https://cds.cern.ch/record/1165534/files/CERN-Brochure-2009-003-Eng.pdf, Feb 2009, unpublished. 31

[62] O. Brüning *et al.*, "LHC Design Report", CERN, 2004. https://cds.cern.ch/record/782076/files/CERN-2004-003-V1.pdf. 31

[63] A. Collaboration, "Charged-particle multiplicities in pp interactions measured with the ATLAS detector at the LHC", *New J.Phys.* **13:053033,2011** (2010) arxiv:1012.5104. 32

[64] **ALICE** Collaboration, P. Cortese *et al.*, "ALICE technical design report on forward detectors: FMD, To and Vo", 2004, https://cds.cern.ch/record/781854/files/lhcc-2004-025.pdf. 32

[65] **ALICE** Collaboration, M. Gallio *et al.*, "ALICE Zero-Degree Calorimeter (ZDC): Technical Design Report", CERN, 1999. https://cds.cern.ch/record/381433/files/Alice-TDR.pdf. 32

[66] C. Z. for the ALICE Collaboartion, "Particle Identification with the ALICE detector at the LHC", arxiv:1209.5637. 33

[67] A. Kalweit, "Particle Identification in the ALICE Experiment", arxiv:1107.1514. 33

[68] B. Bathen, "Jet Measurements and Reconstruction Biases in Proton–Proton and Pb–Pb Collisions with ALICE at the LHC", PhD thesis, 2012. http://qgp.uni-muenster.de/thesisdb/diss-bathen-12.pdf. 33

[69] **ALICE** Collaboration, C. W. Fabjan *et al.*, "ALICE trigger data-acquisition high-level trigger and control system: Technical Design Report", CERN, 2004. https://cds.cern.ch/record/684651. 33

[70] **ALICE** Collaboration, "ALICE Inner Tracking System (ITS): Technical Design Report", CERN, 1999. http://aliceinfo.cern.ch/ITS/sites/aliceinfo.cern.ch.ITS/files/documents/ITS_TDR.pdf. 34

[71] **ALICE** Collaboration, G. Dellacasa *et al.*, "ALICE time projection chamber: Technical Design Report", CERN, 2000. https://cds.cern.ch/record/451098/files/open-2000-183.pdf. 34

[72] A. Collaboration, "Performance of the ALICE Experiment at the CERN LHC", arxiv:1402.4476. 34

[73] R. Brun and F. Rademakers, "ROOT: An object oriented data analysis framework", *Nucl.Instrum.Meth.* **A389** (1997) 81–86. 35

[74] "AliRoot Documentation". http://aliweb.cern.ch/Offline/AliRoot/Manual.html. 35

[75] T. Sjostrand, S. Mrenna, and P. Skands, "PYTHIA 6.4 Physics and Manual", *JHEP* **0605:026,2006** (JHEP 0605:026,2006) hep-ph/0603175. 35

[76] P. Z. Skands, "Tuning Monte Carlo Generators: The Perugia Tunes", *Phys.Rev.D* **82:074018,2010** (2010) arxiv:1005.3457. 35

[77] N. Armesto, L. Cunqueiro, and C. A. Salgado, "Q-PYTHIA: a medium-modified implementation of final state radiation", *Eur.Phys.J.C* **63:679-690,2009** (2009) arxiv:0907.1014. 35

[78] R. Brun, F. Carminati, and S. Giani, "GEANT Detector Description and Simulation Tool", 1994, http://inspirehep.net/record/863473/files/geantall_CERN-W5013.pdf. 35

[79] A. Collaboration, "Measurement of Event Background Fluctuations for Charged Particle Jet Reconstruction in Pb-Pb collisions at $\sqrt{s_{NN}} = 2.76$ TeV", *JHEP* **1203** (2012) 053, arxiv:1201.2423. 37, 38, 53

[80] M. Tannenbaum, "The distribution function of the event-by-event average pt for statistically independent emission", *Phys.Lett* **B** (2001), no. 498, 29–34. 37

[81] P. Kähler. private communication, 2014. 49

[82] A. Collaboration, "Measurement of jet suppression in central Pb-Pb collisions at $\sqrt{s_{NN}} = 2.76$ TeV", arxiv:1502.01689. 49, 50, 51, 53

[83] A. Collaboration, "Measurements of the Nuclear Modification Factor for Jets in Pb+Pb Collisions at $\sqrt{s_{NN}} = 2.76$ TeV with the ATLAS Detector", arxiv:1411.2357. 50, 51

[84] G. D'Agostini, "Bayesian Inference in Processing Experimental Data: Principles and Basic Applications", *Rept.Prog.Phys.* **66** (2003) 1383–1420, arxiv:physics/0304102. 51

[85] A. Hoecker and V. Kartvelishvili, "SVD Approach to Data Unfolding", *Nucl.Instrum.Meth.A* **372:469-481,1996** (Nucl.Instrum.Meth.A372:469-481,1996) hep-ph/9509307. 51

[86] A. Collaboration, "Measurement of the inclusive differential jet cross section in pp collisions at $\sqrt{s} = 2.76$ TeV", *Phys. Lett. B* **722** (2013) 262–272, arxiv:1301.3475. 53

[87] A. Collaboration, "Charged jet cross sections and properties in proton-proton collisions at $\sqrt{s} = 7$ TeV", arxiv:1411.4969. 53

[88] Y.-J. Lee, "QM 2014 – Experimental results on jets in ultra-relativistic nuclear collisions (SLIDES)", 2014. http://indico.cern.ch/event/219436/session/3/contribution/728/material/slides/1.pdf. 53

[89] M. Verweij. private communication, 2014. 64

[90] K. Zapp, J. Stachel, and U. A. Wiedemann, "JEWEL - a Monte Carlo Model for Jet Quenching", arxiv:0904.4885. 69

Acknowledgements

Ich bedanke mich bei Prof. Dr. Wessels und PD Dr. Christian Klein-Bösing dafür, dass sie mir die Masterarbeit ermöglicht haben und damit eine vertiefte Auseinandersetzung mit der Forschung zum Quark-Gluon Plasma als einem der aktuellsten Themen der Hochenergiephysik. Insbesondere möchte ich mich dafür bedanken, dass mir Fortbildungsmöglichkeiten im Ausland ermöglicht worden sind.
Ich danke den Mitgliedern der AG Wessels für das angenehme Arbeitsklima und für die ständige Bereitschaft, einander zu unterstützen. Ich schaue gerne zurück auf die Arbeit an den TRD Supermodulen, die eine weitere Perspektive auf die Arbeit in der Teilchenphysik eröffnete.
Concerning my research stay at CERN, I would like to thank Xiaoming Zhang, Markus Fasel and especially Marta Verweij for the great support. *Hvala* to Goran, Dhevan and Alexej for the great time beyond the physics business. (Žao nam je, da sam donio gripu u Hrvatsku!)
Ich möchte speziell noch danken: Philipp, meinem feinsinnigen battle buddy seit der Bachelorarbeit; Rüdiger als einen hilfreichen Ansprechpartner für technische Details; Christian als meinen Betreuer, der maßgeblich dazu beigetragen hat, dass ich meine Fähigkeiten und ein besonderes Interesse an der Forschung entwickeln konnte.
Zuletzt danke ich meinen Eltern für meine Freiheit im Studium.

Hiermit bestätige ich, dass ich diese Arbeit selbstständig verfasst und keine anderen als die angegebenen Quellen und Hilfsmittel verwendet habe.

Münster, 12.04.2015

Hendrik Poppenborg